A Hard Look at Accretion Around Neutron Stars

by

Renee Ludlam

A dissertation submitted in partial fulfillment
of the requirements for the degree of
Doctor of Philosophy
(Astronomy and Astrophysics)
in the University of Michigan
2019

Doctoral Committee:

Professor Jon M. Miller, Chair
Professor August Evrard
Professor Kayhan Gültekin
Professor Fiona A. Harrison, California Institute of Technology
Professor Keren Sharon

Renee M. Ludlam

rmludlam@umich.edu

ORCID iD: 0000-0002-8961-939X

ACKNOWLEDGMENTS

I would like to thank my PhD advisor, Jon M. Miller, for believing in me and providing me with every opportunity. You pushed me to achieve higher than I thought was possible and I am a better scientist for it. Words can not fully express how grateful I am.

A special thanks to my committee for the support and the valuable feedback throughout my studies.

I would also like to thank my undergraduate research advisor, Ed Cackett, for continuing to mentor me throughout my graduate career. I look forward to continued collaboration as colleagues.

Thank you to my parents whose sacrifices allowed me to pursue a higher education. As well as, for the fierce work ethic that my father instilled in me and for my mother who taught me to "Do right, because it's right, and do it right." A big thank you to my sister for always being there for me and keeping me grounded. You have made graduate school more manageable.

Finally, thank you to the wonderful women in the department who encouraged me through the ups and downs.

TABLE OF CONTENTS

LIST OF TABLES

Table

LIST OF FIGURES

Figure

ABSTRACT

Neutron stars (NSs) are the most compact objects with a surface in the Universe. The only way to understand how matter behaves under the conditions found in NSs is to determine the equation of state (EoS) of ultradense, cold matter. The EoS sets the radius for a NS of a given mass, therefore, measurements of masses and radii can be used to rule out or confirm theoretical EoSs. One method to determine radii of NSs utilizes atomic lines that arise from the inner region of the accretion disk. These lines are broadened due to Doppler and relativistic effects from the motion of the disk and extreme gravity near the NS. The resolution and sensitivity of *NuSTAR* in the $3 - 79$ keV bandpass have provided an unprecedented look at the innermost accretion flow onto NSs. Numerous observations have revealed clear disk reflection spectra, unbiased by detector effects or modeling degeneracies. In this dissertation I demonstrate the importance of these features in determining properties of the accretion disk and NS in low-mass X-ray binaries (LMXBs).

The discovery of multiple emission lines that originate from different ionization states – and presumably radii – within the disk are presented in Chapter 2. Modeling of these lines does not return distinct radii, but this is promising nonetheless for future endeavors that can capture these features with higher signal-to-noise. In Chapter 3, a sample of persistently accreting NSs reveals tight constraints on the position on the inner disk close to the NS. This allows for regions on the mass-radius plane to be traced out, which are already comparable to constraints obtained from other methods to determine NS mass and radius. Moreover, in Chapter 4 I perform the first reflection study of the NS transient XTE J1709−267 as the source transitions

to a higher accretion rate. Hence, I analyze these states separately to track changes in the inner accretion disk, but disk properties remain consistent. In Chapter 5, I demonstrate that Fe lines can be used to estimate the magnetic field strength in these systems to first-order by comparing to estimates from pulsations seen in accreting millisecond X-ray pulsars.

With the growing number of *NuSTAR* observations of reflection spectra in NS LMXBs, I am able to look at the sample as a whole to explore how the inner disk radius changes as a function of mass accretion rate (Chapter 6). There is no clear correlation between the inner disk position and mass accretion rate; confirming previous studies. The recent launch of *NICER* now affords the opportunity to search for low-energy relativistic lines down to 0.25 keV using detectors that are also free of distortions at high flux levels. In Chapter 7, I perform the first *NICER* spectral study using observations of Serpens X-1. This confirmed the reflection nature of the Fe L blend for the first time in a NS system.

Reflection studies of NS LMXBs provides information on NS radii, magnetic field strengths, potential boundary layers between the inner accretion flow and NS surface, as well as properties of the accreting material. The combined bandpass and sensitivity of *NuSTAR* and *NICER* opens a new opportunity to reveal the entire reflection spectrum, and to measure different observables within these systems (Chapter 8). Future studies will enhance our understanding of accretion and how matter behaves under ultradense, cold conditions.

CHAPTER I

Introduction

1.1 Neutron Stars

Neutron stars (NSs) are the densest observable objects in the Universe, since black holes (BHs) are hidden behind event horizons. Their existence was first proposed in the early 1930s by Lev Landau when he hypothesized the formation of a giant nucleus when atomic nuclei are forced into close contact in massive stars (Landau, 1932). It was Walter Baade and Fritz Zwicky that suggested the formation mechanism of these objects is supernovae in 1934 (Baade & Zwicky, 1934). The first observable evidence for the existence on NSs didn't occur until decades later when Jocelyn Bell Burnell discovered radio pulses from a rapidly rotating object (Hewish et al., 1968). It was quickly determined that for such a rapid spin period (< 1 s) the object must be more massive, yet smaller, than white dwarfs (see section 1.2) so as to not surpass break-up velocities (centrifugal force $>$ gravitational force). This required that the pulsating object, dubbed "pulsar" after pulsating star, contains densities on the order of an atomic nucleus.

In the innermost regions of NSs, the internal density exceeds several times the density of an atomic nucleus, ρ_0 (Oppenheimer & Volkoff, 1939), while existing in a cold state (available thermal energy $<$ Coulomb energy per nucleon). We are unable to reproduce this ultra-dense, cold state of matter in Earth based laboratories. Heavy-

ion collisions probe matter at nuclear densities and below ($\rho \leq \rho_0$) at very high temperatures (T > 100 MeV). As a consequence, the only way to understand how matter behaves under ultradense ($\rho \geq \rho_0$) and cold (T < 100 keV) conditions is to determine the equation of state (EoS) of NSs. The EoS sets the mass and radius of the NS through the Tolman-Oppenheimer-Volkoff equations (Tolman 1934, 1939; Oppenheimer & Volkoff 1939), which trace out a unique track on the mass−radius (M−R) plane. Numerous theoretical EoSs have been generated based on different assumptions of internal composition and how the matter behaves, but these can only be narrowed down through observations of NSs. Therefore, in principle, by measuring the radius of NSs of different masses, we can provide tight constraints on the EoS. Section 1.4 presents a brief overview of the state of the field to determine the NS EoS.

1.2 Formation

Stars form from the gravitational collapse of cold gas. As the gas contracts, it heats up to the point where nuclear fusion of hydrogen can occur. This process releases energy in the star's core causing an outward radiation pressure that stabilizes the star from further gravitational collapse. Stars with an initial mass exceeding ~ 10 times that of our Sun ($M_\odot$) are able to fuse elements up to iron (Fe) (Fowler & Hoyle, 1964). The exact amount of energy released in nuclear reactions is related to the difference in the binding energy of the lighter elements and the resulting product since energy must be conserved. The binding energy per nucleon is the energy required to remove a nucleon from the atomic nucleus. See Figure 1.1 for the binding energy per nucleon of different atomic elements. The process of nuclear fusion into heavier elements liberates energy up to Fe; at which point heavier atomic elements start to have a lower binding energy which causes nuclear reactions to become endothermic (requires energy). The only nuclear reaction that can release energy from these elements is through the process of fission, which breaks the heavier elements into lighter constituents. Carroll

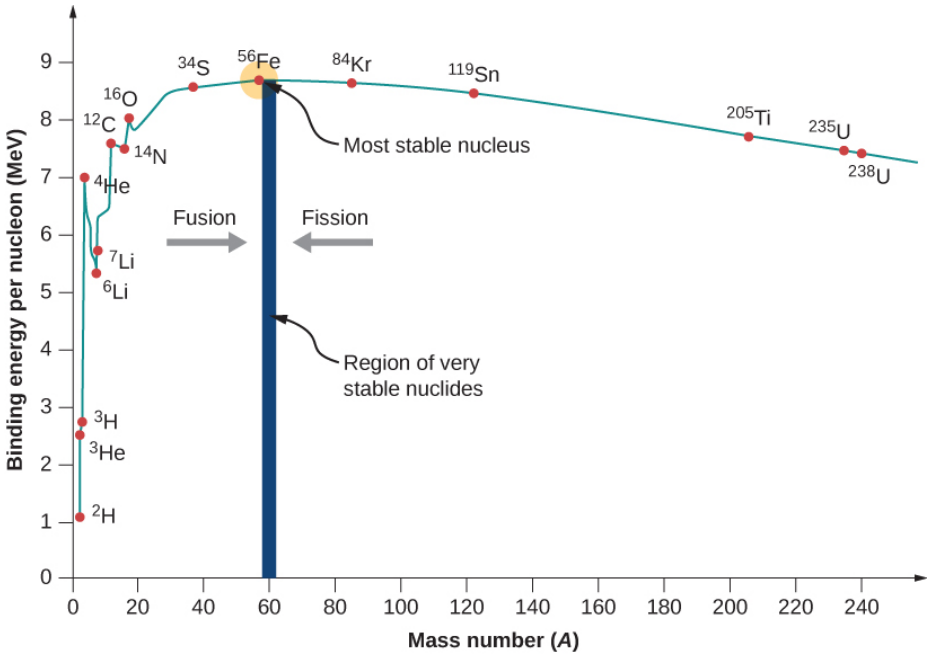

Figure 1.1 Binding energy per nucleon. The mass number A is the number of protons, Z, and neutrons, N, in the atomic nucleus. Image Credit: Ling et al (2016).

& Ostile (2007) and Prialnik (2009) provide an in-depth review of binding energy per nucleon and the various stages of stellar evolution that are not described in detail here.

With the removal of radiation pressure, the core contracts due to its own self-gravity. The core will contract until the electrons within this region become degenerate due to the Pauli Exclusion principle (only one fermion can occupy a given state at a time). For lower mass stars, the core would become stable resulting in the remnant core becoming a white dwarf. However, the core in stars $\gtrsim 10\ M_{\odot}$ are sufficiently massive that degeneracy pressure can not halt the gravitational collapse (Chandrasekhar, 1931). This mass at which gravity overcomes degeneracy pressure is known as the Chandrasekhar mass limit and occurs for degenerate electrons at $\sim 1.46\ M_{\odot}$. Above this mass, the medium will continue to contract until the core is hot enough ($> 2.3\times10^{10}$ K) for photons to photodisintegrate the Fe within this region, generating 13 helium nuclei, 4 neutrons, and 124 MeV of energy per Fe atom. The

collapse continues until the core is hot enough for photons to break-up He into protons and neutrons ($\gamma + {}^4\mathrm{He} \rightarrow 2n + 2p$) at $\sim 7 \times 10^{10}$ K. The medium becomes so dense that the protons can undergo electron capture and become neutrons ($p + e^- \rightarrow n + \nu_e$). This continues until the density is high enough for neutrons to become degenerate at 10^{15} g/cm^3 (Prialnik, 2009). The collapse of the core occurs on a timescale of < 1 s. If the resulting core of predominantly degenerate neutrons is stable, this is the birth of a neutron star.

1.3 Internal Structure

It is difficult to ascertain the exact mass and size of NSs, but they can theoretically have masses and radii between $1 - 3\ M_\odot$ and $8 - 16$ km, respectively (Lattimer & Prakash, 2004). The upper limit of $3\ M_\odot$ is set by causality (Rhoades & Ruffini, 1972), where the speed of sound within the NS must be less than the speed of light. When this is violated, the NS is unstable to perturbations. The minimum mass for a static NS is $\sim 0.1\ M_\odot$, which is increased by rotation (Haensel et al., 2002), but such a small mass seems unlikely given the formation mechanism of core collapse of massive stars discussed in the previous section.

Figure 1.2 provides the internal structure for a canonical NS of 10 km. In accreting NS systems, the envelope is composed of low Z elements (H/He) that are supplied by the infalling material from the companion star. Molecular dynamic simulations show that chemical separation occurs quickly so that the liquid phase is rich in low Z elements while the newly formed solid crust is enriched with high Z elements (Fe) due to the large surface gravity (Brown & Cumming, 2009). The material is buried as more matter accretes. The density rises and the material forms a crystalline lattice of ions and degenerate electrons (Haensel & Zdunik, 1990). This is the crust region, which makes up $10 - 20\%$ of the radial extent of the NS. The crystal lattice formation occurs since nucleons are correlated at short distances by strong interaction and anti-

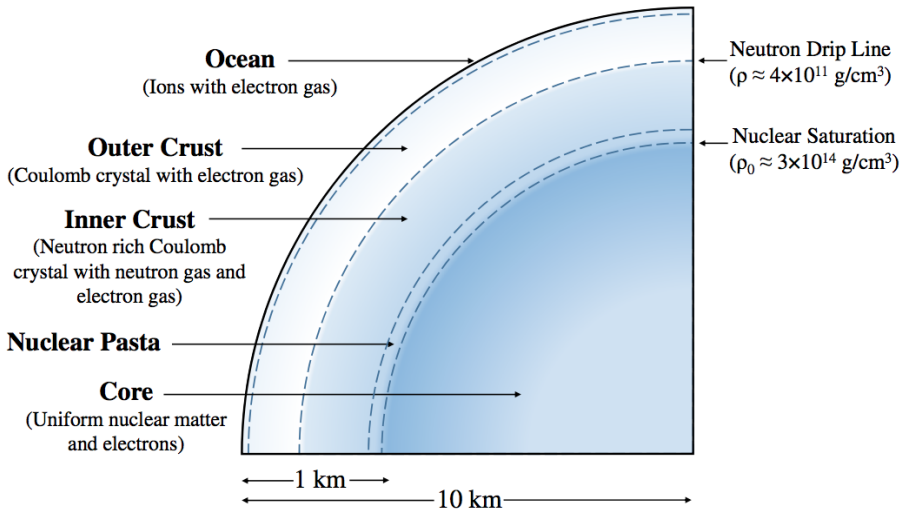

Figure 1.2 Cross section of a neutron star courtesy of Caplan & Horowitz (2017). The crust constitutes $10-20\%$ of the NS radius. The core holds 99% of the mass of the NS (Lattimer & Prakash, 2004).

correlated at large distance by Coulomb repulsion between nuclei. The matter freezes into a crystal structure because the Coulomb energy is larger than the thermal energy, so this is the lowest stable energy configuration.

The outer crust occurs at densities greater than 10^8 g/cm^3 in NSs. The matter is strongly degenerate and relatively cold (T$< 10^8$ K), so thermonuclear reactions are blocked by the Coulomb barrier (Haensel & Zdunik, 1990). The increasing density within this region causes an increase in the Fermi energy of the electrons that drives electron capture, which progressively causes the crust to become more neutron-rich. The original capture reaction occurs in a quasi-equilibrium manner. The resulting nucleus is an odd nucleus, in terms of the number of protons and neutrons, which is unstable in dense matter. As a consequence, the nucleus quickly captures another electron in a non-equilibrium manner (Haensel & Zdunik 1990, 2003) that releases energy on the order of half an MeV/nucleon to become stable (Gupta et al., 2007).

The medium becomes so neutron-rich that neutrons can begin to drip out of

nuclei. This signifies the transition between the outer and inner crust (Caplan & Horowitz, 2017). The inner crust has a density above 10^{11} g/cm^3 and is characterized by the existence of neutron gas surrounding the Coulomb crystal. Since the number of protons is much less than neutrons due to the electron capture reactions in the outer crust, the Coulomb barrier ($U \propto Z^2e^2/r$) prohibiting the nucleus-nucleus reactions lowers. The lack of protons combined with the decrease in the mean distance between the neighboring nuclei allows for pycnonuclear reactions to occur (see Haensel & Zdunik 2008 for a review). These are density-driven reactions that release on the order of 1.5 MeV/nuc in the crust (Haensel & Zdunik, 1990).

At the base of the crust, there may be a layer of nuclear pasta where the nuclei begin to distort due to competing nuclear attraction and Coulomb repulsion when nuclei begin to touch (Caplan & Horowitz, 2017). When the nuclear attraction and Coulomb repulsion length-scales become comparable, the nuclei become distorted into shapes such as tubes like spaghetti or layers like lasagna, hence the term nuclear pasta (Horowitz et al., 2015). Past this region, we encounter the core of the NS. We are uncertain of the exact composition or state of the matter since densities exceed ρ_0. It could simply be a collection of nucleonic matter with electrons and muons. Or perhaps exotic matter such as hyperons or Bose condensates of pions or kaons may arise (Lattimer & Prakash, 2004). Or it could be dense enough that deconfined (up and down) quark matter (QM) can develop (Glendenning, 1992). If the available energy in this region is high enough, then strange quarks can be created in the QM from weak interactions between the up and down quarks (Alcock & Olinto, 1988). This strange quark matter (SQM) has more degrees of freedom, which lowers the energy of the system, and is therefore more stable than nonstrange QM (Witten, 1984). Figure 1.3 demonstrates theoretical mass-radius curves based on assumed internal composition. The only way to know the behavior of matter within the core of NSs is by determining the EoS.

1.4 State of the Field to Determine the EoS

The mass of a binary system can be measured from the binary mass function via the principle of Kepler's third law:

$$f(M) = \frac{M_x^3 \sin^3 i}{(M_c + M_x)^2} = \frac{P_{orb} K^3}{2\pi G} \tag{1.1}$$

where M_x is the mass of the compact object, M_c is the mass of the companion, K is the radial velocity of the companion ($v_c \sin i$), i is the orbital inclination, P_{orb} is the orbital period, and G is the gravitational constant. This can be used to determine the mass of compact objects from observable measurements of the radial velocity and orbital period. The orbit and radial velocity can be measured from Doppler shifts of emission lines such as the Bowen blend (Bowen, 1934) from X-rays irradiating the companion star. The binary mass function can set a lower limit on the M_x if inclination or M_c are unknown. Once the mass of the companion star and inclination is determined, then the degeneracy between the total mass of the system is broken and the mass of the NS is known.

One of the best measurements of a NS's mass we have is through utilization of the Shapiro delay of millisecond pulsar PSR J1614−2230 as pulsations pass through the gravitational potential of the companion star. Shapiro delay refers to an increase in time for light to reach Earth due to passing close to a massive object and time moving slower deeper in the potential well (Shapiro, 1964). The delay of the pulsations during orbital conjunction depends sensitively on the mass of the companion white dwarf (WD). With the mass of the WD combined with orbital information, this led to the discovery of a 2 $M_\odot$ NS (1.97 ± 0.04 $M_\odot$: Demorest et al. 2010), which was the largest NS mass measurement at the time with such certainty. This ruled out EoSs that cannot produce stable NSs of 2 $M_\odot$ (as can be seen in Figure 1.3). A few years later, Antoniadis et al. (2013) reported a second NS with a mass near

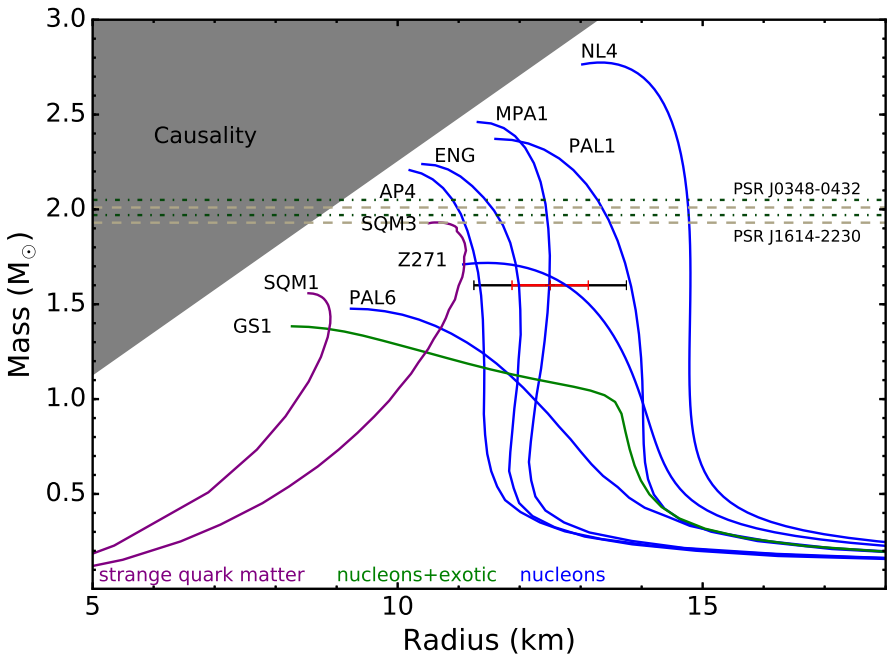

Figure 1.3 The M−R plane for NSs with different theoretical EoS. The gray region is excluded because causality is violated, i.e., the speed of sound > the speed of light inside the NS. A range of M−R curves are shown (Akmal et al. 1998, Horowitz & Piekarewicz 2001, Lattimer & Prakash 2001). Blue indicates nucleonic interior composition, green is a combination of nucleonic and exotic matter (e.g., hyperons or kaon condensates), and purple is strange quark matter. This is not comprehensive, but demonstrative of the behavior of the different internal compositions. The NS mass measurements of PSR J1614−2230 (Demorest et al., 2010) and PSR J0348+0432 (Antoniadis et al., 2013) are denoted by horizontal dashed and dot-dashed lines, respectively. The black and red horizontal bar region indicates the 10% and 5% error on radius for a theoretical NS of $M = 1.6\ M_\odot$ and $R = 12.5$ km.

2 $M_\odot$(PSR J0348+0432: $2.01 \pm 0.04\ M_\odot$) through optical classification of the WD companion type to disentangle the individual masses from the total binary mass; therefore strengthening the constraints on the EoS of supranuclear matter present in NSs.

However, there are still a wide range of theoretical M−R tracks that agree with these more massive NS measurements. It becomes clear that we need radius measurements as well to truly further narrow down the EoS of ultradense, cold matter. The radius is more difficult to measure, but perhaps more important since the radius

is a slowly varying function over a large range in mass for many of the remaining EoS due to three-body interactions between nucleons within the NS (Lagaris & Pandharipande, 1981). Determining the radius to an error of 10% is competitive at ruling out proposed theoretical tracks (e.g., the black horizontal line in Figure 1.3), but tighter constraints are needed to make further progress.

There have been a number of observational methods developed to push on the EoS. One such method is to use emission from Type-I X-ray bursts to indirectly constrain the radius and mass of NSs. Type-I X-ray bursts are thermonuclear runaway events on the surface of a NS due to unstable burning of H/He. These are characterized by a sharp increase in the X-ray intensity on the order of seconds followed by an exponential decay as the ashes cool on timescales of tens to hundreds of seconds. The thermal emission released is gravitationally redshifted and, in principle, the blackbody radius inferred can place an upper limit on the mass of the NS (van Paradijs , 1979). A subset of these events can release enough energy to surpass the local Eddington limit (where radiation pressure exceeds the gravitational pull) and lift the photosphere from the surface of the NS. This is known as a photospheric radius expansion (PRE) burst. By determining the apparent surface area of the blackbody emission during the cooling tail of the burst and the flux when the photosphere has "touchdown" on the surface can return uncorrelated constraints on the masses and radii of NSs when the distance is known (Özel et al. 2010, 2016a). After taking into account errors on distance, the atmosphere composition, and how electron scattering impacts the spectral shape, this produces mass and radius constraints that have $> 10\%$ error.

Another recent effort that is led by the Neutron Star Interior Composition Explorer (*NICER*: Gendreau et al. 2012) payload on the International Space Station (ISS) is to model the X-ray modulations in lightcurves that are produced from hot spots rotating into and out of our line of sight as the NS spins (Bogdanov et al., 2008). Deformations in the sinusoidal wave-form are related to gravitational and relativistic

effects on the NS that depend on its compactness (M/R) and spin rate. The goal of the mission is to constrain the radius to 5% for a few pulsating sources of known mass (see Özel et al. 2016b for more details). This will provide the best constraints to date (see the red horizontal line in Figure 1.3 for visualization), but requires detailed knowledge of the number of hot spots on the surface, their shape, latitude, and temperature profile. Each of these is difficult to precisely determine.

Gravitational waves offer another exciting pathway into narrowing down the EoS with the discovery of event GW170817 (Abbott et al., 2017). NS-NS mergers place an upper limit on the maximum allowed mass of a NS, as well as a minimum radius, based upon arguments for stability (see Bauswein et al. 2017). If the NS-NS merger produces a delayed or no-collapse remnant, then we obtain a lower limit on the threshold mass for BH formation. If the merger results in an immediate collapse to a BH, then this produces tighter limits on the mass division between NSs and BHs. This in-turn can lead to lower-limits on radii for NS, producing conservative regions of exclusion on the M−R plane (Bauswein et al., 2017). With sensitivity updates prior to initiating its third observing run in early 2019, LIGO is projected to detect a handful of NS-NS mergers each year. This will strengthen lower limits on NS radii.

Ultimately, when determining the exact EoS of NSs, each of these methods must produce similar constraints in order to provide independent verification of any previous results. Nature has serendipitously provided the perfect astrophysical laboratory for learning more about NSs, as well as accretion phenomena: low-mass X-ray binaries (LMXBs).

1.5 NS Low-mass X-ray Binaries and Disk Reflection

LMXBs consist of a roughly stellar mass companion that transfers material onto a compact object via Roche-lobe overflow. Figure 1.4 shows an artist impression of a NS LMXB. These systems are ideal for studying accretion disk physics since all

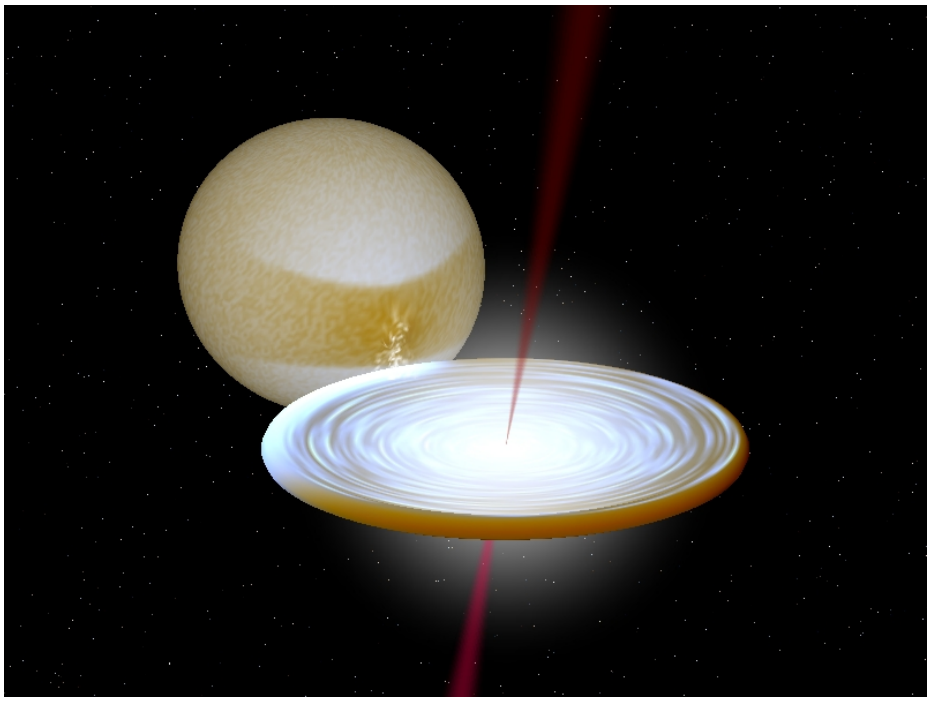

Figure 1.4 Artist impression of a NS LMXB courtesy of Rob Hynes. Material is transferred from the stellar companion via Roche-lobe overflow. The infalling matter forms an accretion disk around the compact object to conserve angular momentum.

accretion occurs via a disk. This is in contrast to high-mass X-ray binaries in which accretion can also take place via winds leading to variable and intrinsic absorption within these systems that can complicate spectral analysis. Bright, persistent NSs in LMXBs are divided into two categories based upon X-ray spectral properties and variability: "atoll" and "Z" type (Hasinger & van der Klis, 1989). The two classes acquire their name from the tracks that the sources trace out in the hardness-intensity diagram and color-color diagram. The mass accretion rate, $\dot{m}$, is often thought to be one of the main reasons for the difference in behavior seen between atoll and Z sources. The mass accretion rate is related to the luminosity by $L = \eta\ \dot{m}\ c^2$, where η is the efficiency of accretion and c is the speed of light. The maximum luminosity is set by the balance between radiation and gravity and is known as the Eddington luminosity, $\mathrm{L_{Edd}}$ (Eddington, 1916). Atoll sources probe a lower range in luminosity ($\sim 0.01 - 0.5\ \mathrm{L_{Edd}}$) in comparison to the near-Eddington Z sources ($\sim 0.5 - 1.0\ \mathrm{L_{Edd}}$;

van der Klis 2006).

There are also transient NS LMXBs that alternate between periods of active accretion and quiescence. This provides the unique opportunity to probe behavior of neutron stars at low and high $\dot{m}$ in a short period of time. Some of these systems even exhibit behaviors seen in both atoll and Z sources over a single outburst (e.g., XTE J1701−462, Homan et al. 2010), which is suggestive of a trend with average $\dot{m}$. Mass accretion rate is likely not the sole driver in the difference of behavior. The strong magnetic fields surrounding neutron stars may also likely play a role (Hasinger & van der Klis 1989; White & Zhang 1997; Ford et al. 2000).

In many instances, the accretion disks in these systems are illuminated by hard X-rays coming either from the boundary layer (where the material from the disk reaches the NS; Popham & Sunyaev 2001), the surface of the NS, a hot electron corona (Sunyaev et al., 1991). The exact location and geometry of the corona is not known, but is often considered to be a compact region close to the NS (see Degenaar et al. 2018 for a review). Regardless of where the hard X-rays originate, the disk reprocesses theses illuminating photons and re-emits them as a continuum with a series of atomic features and Compton backscattering hump superimposed, known as the "reflection" spectrum.

The most prominent feature that arises as a result of disk reflection is the iron K-shell (Fe K) emission line between $6.4 - 6.97$ keV. This intrinsically narrow line profile is broadened by strong Doppler and relativistic effects due to the disk's rotational velocity and proximity to the compact object (Fabian et al., 1989). Figure 1.5 demonstrates these effects on the Fe line profile. The extent of the red wing thereby enables important physical insights to be derived from these systems. Furthermore, the blueshifted emission of the Fe line profile gives an indication of how inclined the disk is due to Doppler effects becoming more prominent with increasing inclination (Dauser et al. 2010). This feature has been reported in both BH (e.g., Miller 2002)

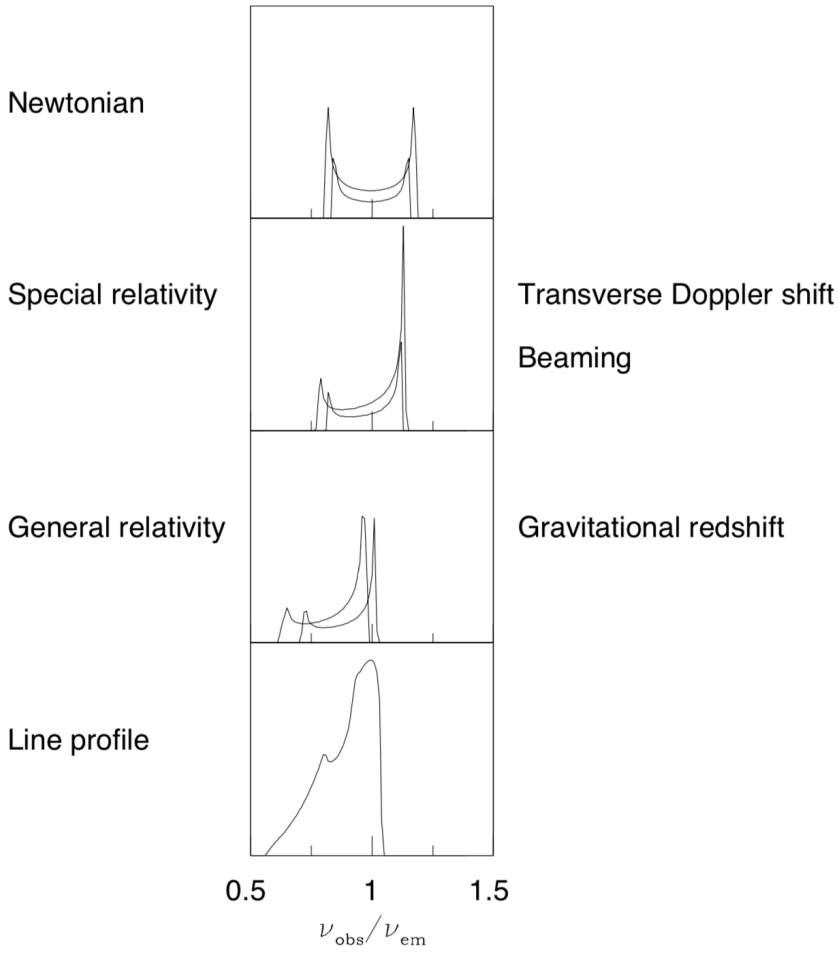

Figure 1.5 Broadening of the Fe K component from the inner accretion disk courtesy Fabian et al. (2000). The top panel shows broadening due Newtonian motion from Keplerian orbits within the disk. The second panel shows the asymmetry induced from the rapid rate at which the matter is moving. This causes the red and blue wings to experience Doppler boosting from the receding and approaching portions of the disk. The third panel shows the gravitational redshift of the line to lower energies due to the large gravitational potential well close to the NS. The lower panel shows the cumulative line profile from these effects summed over radii within the disks.

and NS (e.g., Bhattacharyya & Strohmayer 2007; Cackett et al. 2008) LMXBs, pointing towards a similar accretion geometry despite the difference in mass between the compact objects and the presence of a surface.

The strong Doppler and relativistic effects within the innermost region of the disk impact the entire reflection spectrum. Figure 1.6 shows the rest frame reflected emission utilizing the model XILLVER (García & Kallman 2010; García et al. 2013) and

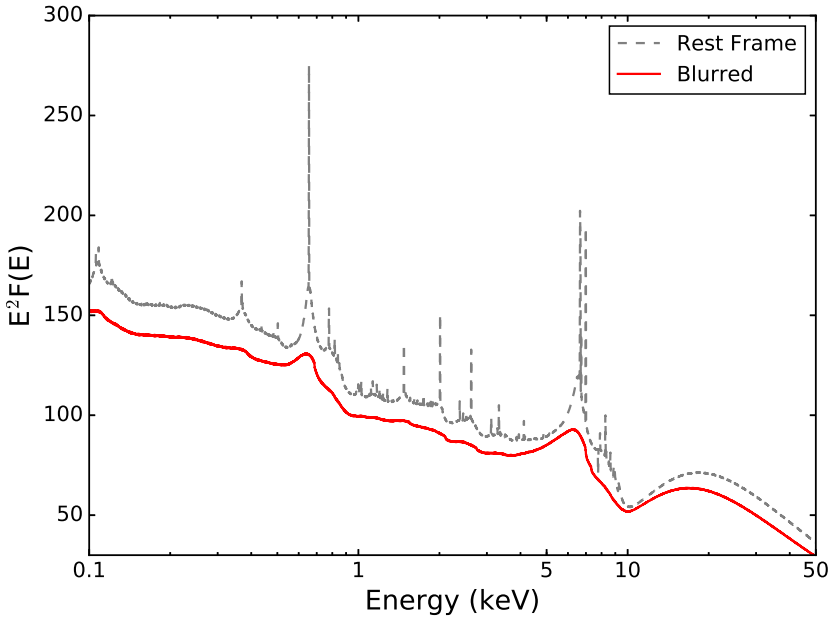

Figure 1.6 Effects of relativistic blurring on the reflection spectrum assuming a power-law with photon index of $\Gamma = 2$ and the material has an ionization of $\log \xi = 3.5$. The rest frame reflection spectrum is generated using XILLVER. The blurred spectrum is generated using RELXILL, which convolves XILLVER with a general relativistic blurring kernal. The disk extends down to $R_{\rm ISCO}$ with a dimensionless spin parameter of $a = 0$.

the resulting blurred spectrum when convolved with general relativistic blurring using the model RELXILL (García et al., 2014). Further details on these models are given in the following chapters. For brevity, the reflection spectrum depends on the illuminating continuum, the abundance of the disk, the disk density, and the inclination at which the system is viewed. The resulting blurred reflection spectrum depends on the dimensionless spin parameter, $a = cJ/GM^2$ (mass normalized description on the total angular momentum of the compact object). The spin parameter determines the position of the inner radius of the accretion disk in general relativity (Misner, Thorne, & Wheeler, 1973). This radius is know as the innermost stable circular orbit (ISCO) and is the smallest radius that a particle can orbit stably. Figure 1.7 shows how $R_{\rm ISCO}$ translates to gravitational radii ($R_g = GM/c^2$) for a given spin parameter. Inside $R_{\rm ISCO}$ the specific angular momentum needed to maintain a stable orbit tends to infinity (Bardeen et al., 1972), so particles quickly fall towards the compact ob-

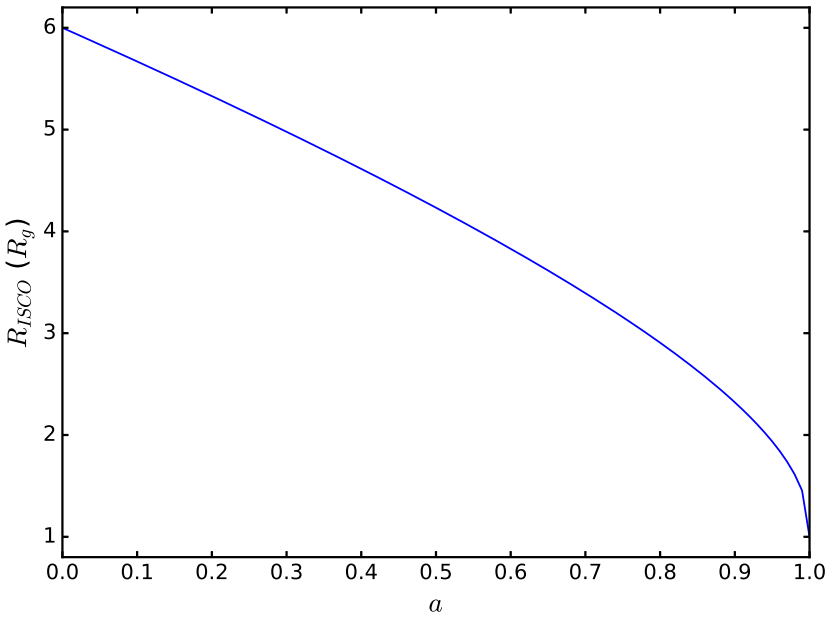

Figure 1.7 Translation from the innermost stable circular orbit $R_{\rm ISCO}$ to gravitational radii R_g for prograde values of the spin parameter, a, using the framework laid out in Bardeen et al. (1972).

ject. Additionally, the reflection spectrum depends on the ionization state, ξ, of the emitting material. Less ionized material will have more bound electrons to absorb incoming radiation and undergo atomic transitions than an accretion disk with higher ionization. This becomes apparent in Figure 1.8 which shows the effect of ionization on the emergent reflection spectrum.

For neutron stars in particular, reflection features can be used to place a limit on the radius of the star since the disk must truncate at or before the surface (Cackett et al. 2008, 2010; Miller et al. 2013; Ludlam et al. 2017a). In the cases where the disk is truncated farther out than $R_{\rm ISCO}$ it is likely due to the magnetosphere of the neutron star or a boundary layer extending from the surface. By assuming that the location of the inner disk inferred from the Fe K line corresponds to the Alfvén radius (where the energy density of the accreting material is balanced by the magnetic energy density outward), we can place estimates on the strength of the magnetic field in these systems (Cackett et al. 2009; Ibragimov & Poutanen 2009).

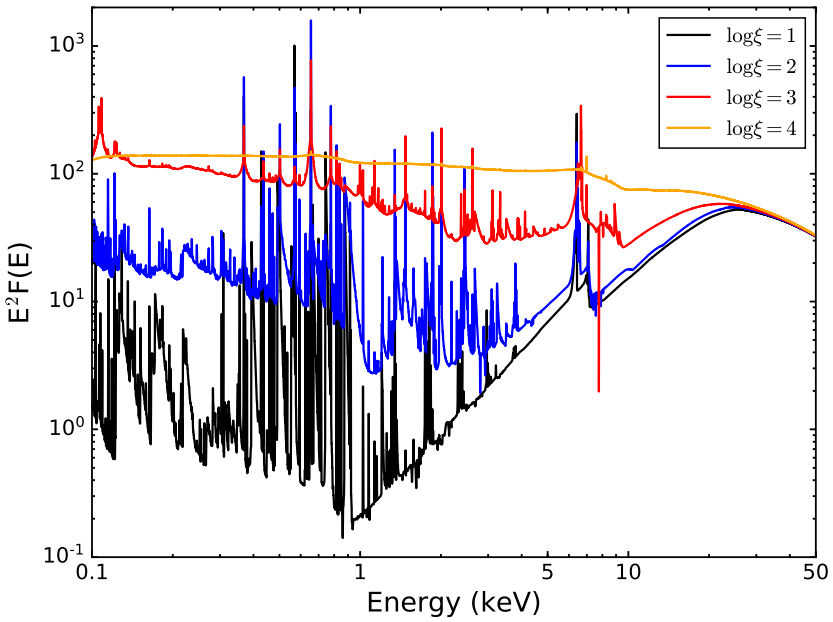

Figure 1.8 The effect of ionization of the emitting material on the reflection spectrum using an input continuum spectrum of a power-law with photon index of $\Gamma = 2$. The material is assumed to have solar abundance.

1.6 X-ray Telescopes and Analysis

X-rays are unable to penetrate the Earth's atmosphere, therefore X-ray observatories need to be lifted above the atmosphere by balloons, rockets, and spacecrafts. The data presented in this work was acquired via spacecraft X-ray telescopes. As a result, it is important to understand how X-rays are collected prior to discussing the missions that are used in this dissertation. The incoming X-ray photons need to be focused onto a detector, but the photons are so energetic that nearly half of them would travel straight through mirrors when the angle of incidence is close to 90° (Kitchin, 2009). Most X-ray telescopes use a Wolter type I design in order to focus X-rays (Arnaud et al., 2011). This utilizes grazing incidence angles from nested shells of reflective surfaces that achieve an angle of incidence of $< 5°$ with the incoming photons. It is worth noting that the grazing angle for X-ray reflection is $\theta_c \propto \sqrt{Z}/E$ (Arnaud et al., 2011). Hence, mirrors are often coated in high-Z elements (e.g., gold, platinum,

etc.) in order to obtain larger fields of view. Figure 1.9 provides a schematic of the focusing mechanism using nested shells of paraboloidal and hyperboloidal mirrors. The concentric shells of nested mirrors allows more photons to be collected from the source in comparison to a single annulus of mirror.

Different detectors can be placed at the focus to record the incoming radiation, such as charge-coupled devices (CCDs), cadmium zinc telluride (CZT) detectors, and silicon drift detectors (SDDs). Each of these are able to determine the incoming photons energy based on the amount of ionization that is produced within the detector. For CCDs, the incoming X-ray generates electron-hole pairs within the semiconductor substrate, which is typically made of silicon and sensitive from a few 100 eV to 10 keV (Arnaud et al., 2011). The number of electrons that are produced is proportional to the energy of the photon. An electric field is applied to the to collect the electrons which are shuffled from pixel to pixel across gates by changing the voltage between adjoining gates. This continues until the charge cloud reaches the readout amplifier. Here the electrons are sensed and the pulse height can be digitized in analog-to-digital units (ADU). The pulse height is a measure of the number of electrons generated by the event photon and, therefore, can be scaled to energy by the gain of the detector.

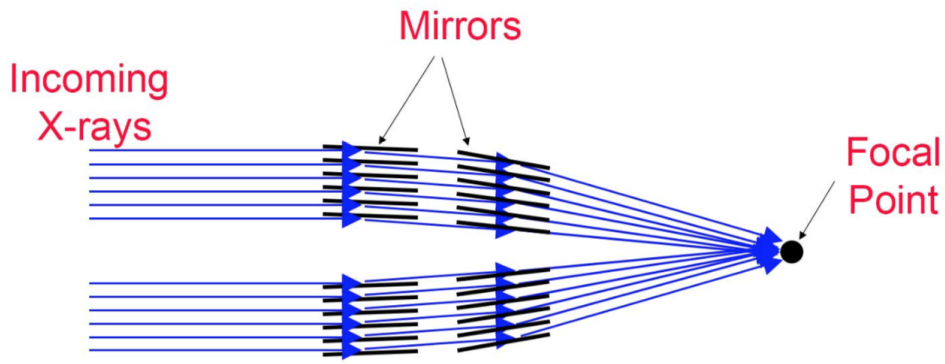

Figure 1.9 X-ray focusing optics for a Wolter Type 1 telescope from NASA's Imagine the Universe. Grazing incidence angles are needed to focus these high energy photons. Nested shells allow for more X-ray photons to be collected at once.

CZT detectors and SDDs are solid-state detectors which do not transfer charges across rows or columns. CZT detectors are small (< 1 mm), but can be placed in an array with individual readouts to increase collecting area. Their main advantage is sensitivity to photon events above 10 keV (Arnaud et al., 2011). When an X-ray photon passes into the material it creates electron-hole pairs that are collected by the electrodes on the top and bottom of the semiconductor (Kitchin, 2009). The resulting pulse height is recorded by the electronics onboard. SDDs again work in a similar manner. There is a potential gradient in the radial direction which guides electrons generated from an incident X-ray towards the central anode where they are then amplified and converted into a signal (Prigozhin et al, 2012).

Some of the initial work on Fe lines in bright galactic sources was complicated by "pile-up" effects from CCD detectors. Pile-up occurs when two or more low-energy photons interact with the CCD during a single frame readout and register as one higher energy photon. This causes issues in skewing the overall shape of the Fe line profile (Ng et al. 2010; Miller et al. 2010). The line profile becomes artificially narrowed by this effect, leading to the position of inner accretion disk being systematically under-predicted (i.e., larger inferred radii). In order to attempt to address this issue, generally there are different operational modes that need to be used when observing these bright sources (e.g., *XMM-Newton*'s Burst or Timing modes, *Neil Gehrels Swift Observatory*'s Window Timing mode, or *Suzaku*'s Windowed Burst mode). These modes tend to group chips and have much shorter read out times, but often do not fully eliminate pile-up or lack rigorous calibration.

The Nuclear Spectroscopic Telescope Array (*NuSTAR*: Harrison et al. 2013), launched in 2012, is the first hard X-ray focusing telescope with a bandpass from $3 - 79$ keV. In order to focus these higher energy X-rays, *NuSTAR* has 133 nested glass shells with a $\sim$ 10 meter focal length achieved by a deployable mast. The glass shells are coated in tungsten/silicon (W/Si) for the outer 44 shells and plat-

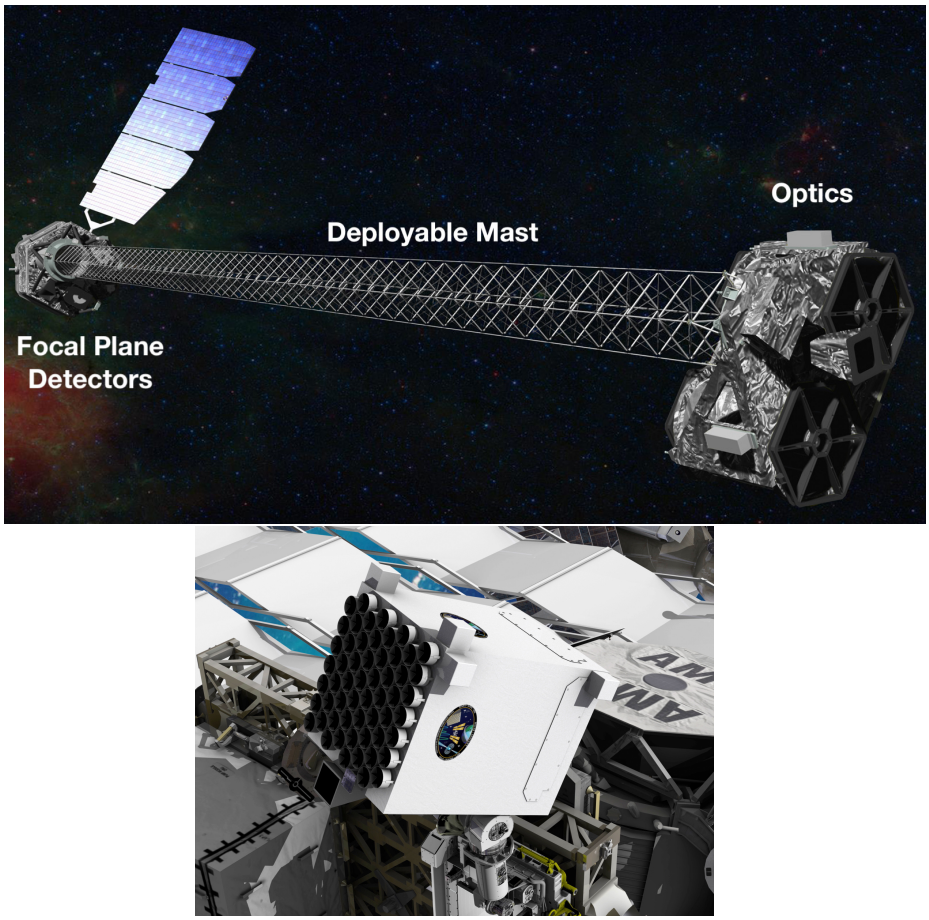

Figure 1.10 Artist's concept of *NuSTAR* in orbit (credit: NASA/JPL-CalTech) and *NICER* mounted on the International Space Station (credit: NASA).

inum/carbon (Pt/C) for the inner 89 shells. Figure 1.10 shows the *NuSTAR* mission with the mast deployed in orbit. *NuSTAR* is in a low-inclination orbit to minimize time spent passing through the South Atlantic Anomaly (SAA). The SAA is a region of increased high-energy particle radiation where the Earth's magnetic field is weakest. Rather than using CCDs to read out events, *NuSTAR* has two focal plane modules with four detectors that have 32×32 individual CZT pixels that read out detector events. This provides a high throughput with no pile-up effects until a threshold of 10^5 counts s^{-1}, which is orders of magnitude larger than CCD based missions. The spectral energy resolution is 400 eV at 6 keV and 900 eV at 60 keV with a timing resolution of 0.1 ms. This is superior energy resolution in comparison to previous

hard X-ray instruments like *Suzaku*/HXD (4000 eV at 17 keV: Takahashi et al 2007), *RXTE*/HEXTE (9000 eV at 60 keV: Rothschild et al. 1998), or *INTEGRAL*/IBIS (8000 eV at 100 keV: Hermsen & Winkler 1998). The collecting area of *NuSTAR* is ~ 800 cm^2 at 6 keV with a field of view of 10 arcminutes.

The recent installation of *NICER* on the ISS in 2017, which is comprised of 56 (52 operational) individual concentrating optics with silicon drift detectors, provides access to the lower energy bandpass from 0.2-12 keV that is free from pile-up effects as well. See Figure 1.10 for an image of the *NICER* mission on the ISS. Each individual concentrating optic has 24 nested shells with a SDD pair that is able to record events to within 300 ns. *NICER* does not have imaging capabilities, but it does have a large peak collecting area of 1900 cm^2 at 1.5 keV with a field of view of 6 arcminutes in diameter. The energy resolution is 140 eV at 6 keV. More information on the *NICER* mission can be found in Gendreau et al. (2012).

In X-ray spectral analysis, we have to rely on our knowledge of how the detectors respond to the incoming radiation in order to derived knowledge from the detected source events (see Arnaud et al. 2011). This is often referred to as "forward-folding". The detectors record photon counts per channel. The redistribution matrix file (RMF) provides the probability that the detector would register an incoming photon of a given energy within a specific channel, thereby enabling the conversion from channel to energy for source counts. The ancillary response file defines the effective collecting area of the instrument as a function of energy. Anticipated models to describe the actual source spectrum are folded through the detector specific responses and statistically compared to the photons that were collected to determine the goodness-of-fit, χ^2 (see Arnaud et al. 2018). The goodness-of-fit is defined as $\chi^2 = \Sigma(C(I) - C_P(I))^2/(\sigma(I))^2$, where $C(I)$ and $C_P(I)$ are the counts per channel and predicted counts per channel, respectively. $\sigma(I)$ is the error in channel I and is given by $\sqrt{C(I)}$ since we are in a photon limited regime. This is the standard fit routine for the field that is executed

through the X-ray spectral fitting package XSPEC (Arnaud, 1996).

1.7 Dissertation Overview

In Chapter 2, I perform the reflection study of the transient NS LMXB 1RXS J180408.9−34205 while in the hard spectral state during its 2015 outburst. The combined bandpass of *NuSTAR* with the reflection grating spectrometer aboard *XMM-Newton* revealed multiple reflection features. These features are generated at different ionization states suggesting that they arise from different regions within the accretion disk. I attempt to measure the radius at which these features occur.

In Chapter 3, I analyze a sample of three persistently accreting NSs: 4U 1636−53, GX 17+2, and 4U 1702−44. The extent of the inner edge of the accretion disk is close to the NS in two out of three of the systems. Combined with previously reported spin frequencies, I am able to explore constraints on the M−R plane. Additionally, I combed literature to explore how the inner extent of the accretion disk changed with mass accretion rate based upon *NuSTAR* observations.

In Chapter 4, I report on the first spectral study of emission features in the NS transient XTE J1709−267. The source was captured during its 2016 outburst with *NuSTAR* Director Discretionary Time. The source underwent a change in flux during the observation which I separate into low and high flux intervals. I attempt to probe changes in the inner accretion disk, but the results agree at the 3σ level. The disk was truncated prior to $R_{\rm ISCO}$ allowing for conservative limits to be placed on the magnetic field strength of the neutron star.

In Chapter 5, we target the iconic transiently accreting millisecond X-ray pulsar Aquila X-1 with *NuSTAR* during its 2016 outburst. Since the source was observed with *NuSTAR* during its previous outburst in 2014, I was able to compare and contrast the spectral features. I compare the magnetic field strengths ascertained from Fe lines to the ones obtained from X-ray pulsations. I confirm that Fe lines can be used to

measure magnetic field strengths to first order.

In Chapter 6, I look at a sample of four persistently accreting atoll sources: GX 3+1, 4U 1702−429, 4U 0614+091, and 4U 1746−371. These sources probe a lower range of apparent luminosity from $0.006 - 0.11$ L_{Edd} than in the previous chapters. Broad reflection features are detected in three out of four sources. I am able to measure the extent of the innermost accretion disk and place limits on the magnetic field strength in these systems. The final source does not require reflection to describe the spectrum. I discuss possible explanations for the lack of reflection in this system and revisit how the position of the inner disk depends on the mass accretion rate.

In Chapter 7, I execute the first spectral study of Serpens X-1 with *NICER*. This is the third *NICER* publication post launch, as well as the first spectral analysis published with *NICER* data. Due to *NICER*'s energy resolution and bandpass, I am able to resolve the Fe L blend at ~ 1 keV in a neutron star system for the first time. This is detected concurrently with an Fe K feature at ~ 6.4 keV, which allows us to test new reflection models and localize the emission region of these features.

Chapter 8 provides concluding remarks and a look toward the future for reflection studies in NS LMXBs.

CHAPTER II

NuSTAR and *XMM-Newton* Observations of the Neutron Star X-ray Binary 1RXS J180408.9-34205

2.1 Preface

This chapter appears in the Astrophysical Journal, Volume 824, page 37 (Ludlam et al., 2016) and is co-authored by Jon M. Miller, Edward M. Cackett, Andy C. Fabian, Matteo Bachetti, Michael L. Parker, John A. Tomsick, Didier Barret, Lorenzo Natalucci, Vikram Rana, and Fiona A. Harrison. The paper is reproduced here under the non-exclusive rights of republication granted by the American Astronomical Society to the authors of the paper.

2.2 Abstract

We report on observations of the neutron star (NS) residing in the low-mass X-ray binary 1RXS J180408.9-34205 taken 2015 March by *NuSTAR* and *XMM-Newton* while the source was in the hard spectral state. We find multiple reflection features (Fe K_α detected with *NuSTAR*; N VII, O VII, and O VIII detected in the RGS) from different ionization zones. Through joint fits using the self consistent relativistic reflection model RELXILL, we determine the inner radius to be $\leq 11.1\ R_g$. For a 1.4 $M_\odot$ NS with a spin of $a_* = 0$, this is an inner disk radius of ≤ 22.2 km. We

find the inclination of the system to be between 18°-29°. If the disk is truncated at a radius greater than the neutron star radius, it could be truncated by a boundary layer on the neutron star surface. It is also possible that the disk is truncated at the magnetospheric radius; conservative estimates would then imply $B \leq (0.3-1.0)\times10^9$ G at the magnetic poles, though coherent pulsations have not been detected and the source is not identified as a pulsar.

2.3 Introduction

Low-mass X-ray binaries (LMXBs) consist of a compact object that accretes matter via Roche-lobe overflow from a roughly stellar mass companion. Broad iron line profiles have been seen in these accreting systems that harbor a black hole (BH; e.g. Fabian et al. 1989; Miller 2007; Reis et al. 2008, 2009a) or a neutron star (NS; e.g. Bhattacharyya & Strohmayer 2007; Papitto et al. 2008; Cackett et al. 2008, 2009, 2010; Di Salvo et al. 2009; Egron et al. 2013; Miller et al. 2013) as the primary accreting compact object. The asymmetrically, broadened profile of the Fe K_α line gives a direct measure of the position of inner disk since the effects of gravitational redshift and Doppler redshift/boosting on the emission line become stronger closer to the compact object (Fabian et al., 1989).

The Fe K_α line in NS LMXBs can be used to set an upper limit for the radius of NS since the disk must truncate at or before the surface (Cackett et al. 2008, 2010; Reis et al. 2009b; Miller et al. 2013; Degenaar et al. 2015). Constraining the radius of the NS can, in turn, lead to narrowing down the equation of state of the cold, dense matter under extremely dense physical conditions (Lattimer, 2011). On the other hand, if the accretion rate is low, it may be possible to constrain the stellar magnetic field based on the radius at which the disk truncates (Cackett et al. 2009; Papitto et al. 2009; Miller et al. 2011; Degenaar et al. 2014).

1RXS J180408.9-34205 (hereafter 1RXS J1804) was classified as a neutron star

LMXB after Type I X-ray bursts were detected during the INTEGRAL Galactic Bulge Monitoring in 2012 May (Krimm et al., 2015a). The bursts provided an upper limit of 5.8 kpc as the distance to the binary system. Follow up observations with *Swift* less than a month later showed that the neutron star had returned to quiescence (Kaur & Heinke, 2012).

The source remained quiet until early 2015 when it began to show a steady increase of hard X-rays in the 15-50 keV as seen with *Swift*/BAT (Krimm et al., 2015a). MAXI/GSC also detected a gradual increase in the 2-20 keV band (Negoro et al., 2015) confirming that 1RXS J180408 had indeed gone into outburst. The hard X-ray brightness increased until plateauing at 100 mCrab on 2015 February 5 with a flux $\sim$ 160 times the quiescent rate (Krimm et al., 2015a). Type I X-ray bursts were again seen during this observation (Krimm et al., 2015a), reaffirming the source's classification as having a neutron star as its primary. Krimm et al. (2015a) noted that the X-ray spectrum seen was adequately described by a simple absorbed power law model.

Radio observations performed with the VLA in 2015 March detected the presence of a jet (Deller et al., 2015). *Swift* X-ray spectra were still described by a single power law placing J180408's location on the radio/X-ray luminosity plane consistent with hard-state neutron star LMXBs (Deller et al., 2015). However, in early April a drop in the hard X-rays was seen with *Swift*/BAT in conjugation with an increase in softer X-ray emission seen by MAXI/GSC (Degenaar et al., 2015a). This suggests that the source entered a soft spectral state. *Swift* spectra could no longer be described by a simple power law but required the presence of an additional disk component and black body component (Degenaar et al., 2015a).

We report on observations taken 2015 March by *NuSTAR* and *XMM-Newton* while the source was still in the hard spectral state. We focus on the importance of constraining the neutron star's inner radius from its reflection spectrum in this state

since it is not obscured by thermal emission in the lower energies.

2.4 Observations and Data Reduction

2.4.1 *NuSTAR*

NuSTAR (Harrison et al., 2013) observed the target for ≃80 ks between 9:21 UT on 2015 March 5 and 7:36 UT March 6 (Obs ID 80001040002). Lightcurves and spectra were created using 120″ circular extraction region centered around the source and another region of the same dimensions away from the source as a background using the NUPRODUCTS tool from NUSTARDAS v1.3.1 with CALDB 20150123. There were a total of 5 Type 1 X-ray bursts present in the lightcurves. We will report on the bursts in a separate paper. We created good time intervals (GTIs) to remove 100 – 170 s after the initial fast rise (depending on the duration of the individual burst) to separate these from the steady emission. These GTIs were applied during the generation of the spectra for both the FPMA and FPMB. Initial modeling of the steady spectra with a constant fixed to 1 for the FPMA and allowed to float for the FPMB was found to be within 0.95-1.05. We proceeded to combine the two source spectra, background spectra, and ancillary response matrices via ADDASCASPEC. We use ADDRMF to create a single redistribution matrix file. The spectra were grouped using GRPPHA to have a minimum of 25 counts per bin (Cash, 1979). The net count rate was 39.9 counts/s.

2.4.2 *XMM-Newton*

XMM-Newton observed the target on 2015 March 6 (Obs ID 0741620101) on revolution 2791 for 57 ks. The EPIC-pn camera was operated in 'timing' (∼41.1 ks) and 'burst' (∼9.5 ks) mode during this time with a medium optical blocking filter. The RGS cameras were also operational for ≃55.8 ks. The data were reduced

using SAS ver. 13.5. We are primarily interested in the spectra obtained from RGS due to the high-resolution. Moreover, the Epic-pn 'timing' mode and 'burst' mode spectra suffer from pile-up and calibration issues (Walton et al., 2012). Even when eliminating the central most columns from the observation, the spectra obtained in the different modes did not agree with *NuSTAR* or even each other. *NuSTAR* does not suffer from photon pile-up, so we chose to characterize the spectrum through the Fe K band using only *NuSTAR*. During the observation, there were 7 Type 1 X-ray bursts which were filtered from the data by GTIs that removed 125 – 225 s after the initial fast rise depending on the duration of each burst. We then created spectra through RGSPROC that were grouped using GRPPHA to have a minimum of 25 counts per bin to allow the use of χ^2 statistics. There were an average of 2.6 counts/s for RGS1 and 3.3 counts/s for RGS2.

2.5 Spectral Analysis and Results

We use XSPEC version 12.8.1 (Arnaud, 1996) in this work. All errors are quoted at $\geq$ 90% confidence level. We account for the neutral column hydrogen density along the line of sight via tbnew[1]. The solar abundance was set to WILM (Wilms et al., 2000) and VERN cross sections (Verner et al., 1996) were used. The RGS and *NuSTAR* were considered between 0.45-2.1 keV and 3.5-50.0 keV, respectively. The choice of the lower energy bound of *NuSTAR* data was motivated by two high bins in the low energy of the spectrum.

2.5.1 NuSTAR

We start with investigating the *NuSTAR* data alone. Initial fits were performed with an absorbed power law with two Gaussian lines at 10.1 keV and 11.5 keV to ac-

[1]Wilms, Juett, Schulz, Nowak, in prep, http://pulsar.sternwarte.uni-erlangen.de/wilms/research/tbabs/index.html

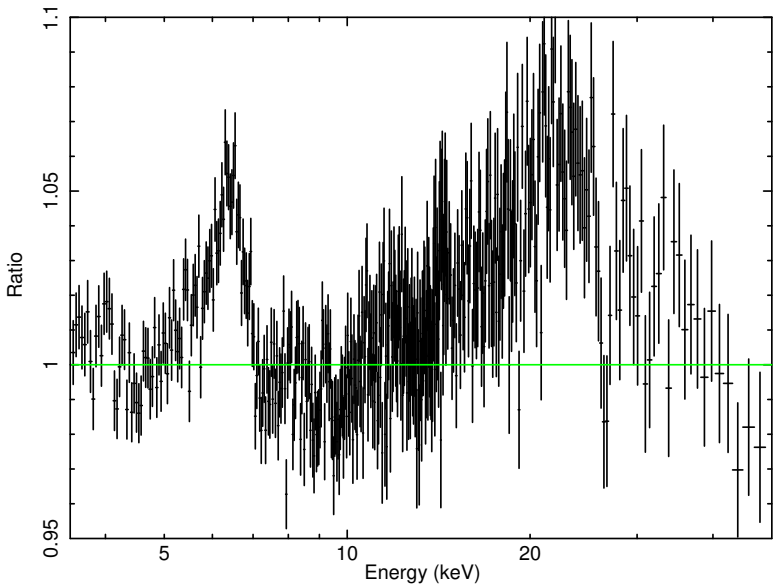

Figure 2.1 Ratio of the data to the continuum model for *NuSTAR* observation of 1RXS J180408. A simple cut-off power law was fit over the energies of 3.5-5 keV, 8-15 keV, and 30.0-50.0 keV. The iron line region from 5-8 keV and reflection hump was ignored to prevent the feature from skewing the fit. We ignore the region above 15 keV in this fit due to the presence of a X-ray reflection hump that peaks between 20-30 keV. The data was rebinned for plotting purposes.

count for instrumental response features (Harrison et al., 2013). These Gaussians will be present in all *NuSTAR* fits hereafter. This gives a particularly poor fit (χ^2/dof = 9545/1159). The addition of a blackbody to account for thermal component in the spectrum did not improve the goodness of fit (χ^2/dof = 9545/1157). The absence of a thermal component is consistent previous investigations of 1RXS J1804 in the hard state (Negoro et al. 2015; Krimm et al. 2015a; Deller et al. 2015).

A prominent Fe K_α line centered $\sim$ 6.4 keV with a red wing extending to lower energies and Fe edges can be seen rising above the continuum in Figure 2.1. There is also a prominent reflection hump in the higher energies above 10 keV. These reflection features not being properly described lend to the poor goodness of fit. Since a thermal component is not necessary to describe the spectrum, the only source of emission is a power law. This means the disk is being illuminated by a source of hard X-ray photons and likely follows a radial dependence R^{-3} profile.

To properly describe the reflection features and relativistic effects present in the data we employ the model RELXILL (García et al., 2014). This model self-consistently models for X-ray reflection and relativistic ray tracing for a power law irradiating an accretion disk. The parameters of this model are as follows: inner emissivity (q_{in}), outer emissivity (q_{out}), break radius (R_{break}) between the two emissivities, spin parameter (a_*), inclination of the disk (i), inner radius of the disk (R_{in}), outer radius of the disk (R_{out}), redshift (z), photon index of the power law(Γ), log of the ionization parameter ($log(\xi)$), iron abundance (A_{Fe}), cut off energy of the power law (E_{cut}), reflection fraction (f_{refl}), angleon, and normalization.

A few reasonable conditions were enforced when making fits with RELXILL. First, we tie the outer emissivity index, q_{out} to the inner emissivity index, q_{in}, to create a constant emissivity index that is allowed to vary between 1 to 3. Next, we fix the spin parameter, a_* (where $a_* = cJ/GM^2$), in the model RELXILL to 0 in the subsequent fits since NS in LMXBs have $a_* \leq 0.3$ (Miller et al. 2011; Galloway et al. 2008). This does not hinder our estimate of the inner radius since the position of the inner most stable circular orbit (ISCO) is relatively constant for low spin parameters. In fact, Miller et al. (1998) found that corrections for frame-dragging for $a_* < 0.3$ give errors $\ll 10\%$. Further, the outer disk radius has been fixed to 400 R_g (where $R_g = GM/c^2$). Lastly, to ensure that the inclination is properly taken into account in the reflection from the disk, we set angleon=1 rather than 0 (angle averaged).

Fits with TBNEW*RELXILL and two Gaussian components, again account for instrument response features, provide a significantly better fit ($\chi^2/dof = 1213/1151$). This is well over a 20σ improvement. Values for model parameters are given in Table 2.1. Figure 2.2 shows the modeled spectrum and ratio of the model to the data. The absorption column density is $(2.0 \pm 2.0) \times 10^{21}$ cm^{-2}. The large uncertainties are due to the lack of data in the low energy range where X-ray absorption is prevalent. The photon index is consistent with the hard limit of 1.4 at the 90% confidence level. The

Table 2.1 Relxill Fitting of *NuSTAR* and RGS

Component	Parameter	NuSTAR	RGS	NuSTAR + RGS
TBNEW	$N_H(10^{22})$	0.2 ± 0.2	0.360 ± 0.002	0.345 ± 0.001
	A_O	...	1.77 ± 0.01	1.71 ± 0.01
RELXILL	$q_{in} = q_{out}$	$2.4^{+0.5}_{-0.4}$	< 1.9	1.3 ± 0.2
	a'_*	0	0	0
	$i(^\circ)$	25 ± 4	$18.4^{+0.5}_{-0.2}$	18.3 ± 0.2
	$R_{in}(ISCO)$	$1.9^{+1.4}_{-0.8}$	$1.2^{+3.3}_{-0.2}$	≤ 1.85
	$R_{out}(R_g)'$	400	400	400
	z'	0	0	0
	Γ	< 1.424	< 1.402	1.402 ± 0.001
	$log(\xi)$	$2.4^{+0.4}_{-0.1}$	3.14 ± 0.03	2.75 ± 0.01
	A_{Fe}	$0.83^{+0.4}_{-0.3}$	< 0.51	< 0.51
	$E_{cut}(keV)$	45^{+2}_{-1}	30 ± 3	47.3 ± 0.3
	f_{refl}	0.15 ± 0.02	0.21 ± 0.01	0.15 ± 0.01
	angleon$'$	1	1	1
	norm (10^{-2})	$9.5^{+0.3}_{-0.6}$	9.81 ± 0.04	9.35 ± 0.01
RELLINE	E_{line}	...	0.569 ± 0.001	0.569 ± 0.001
	norm (10^{-3})	...	6.7 ± 0.8	3.9 ± 0.6
	χ^2_ν(dof)	1.05 (1151)	1.48 (2804)	1.34 (3963)

$'$ = fixed

Note.— Errors are quoted at ≥ 90 % confidence level. Setting angleon=1 takes the inclination into account when modeling reflection. A constant was allowed to float between *NuSTAR* and the RGS data. The *NuSTAR* was frozen at the value of 1.0, RGS1 was fit at 1.234 ± 0.006, and RGS2 was fit at 1.182 ± 0.005. The emissivity index, inclination, and inner radius in RELLINE were tied to the values in RELXILL. The unabsorbed flux from the combined *NuSTAR*+RGS fit from 0.45-50.0 keV is $F_{unabs,(0.45-50.0\ \mathrm{keV})} = 1.71 \times 10^{-9}$ ergs cm^{-2} s^{-1}. This gives a luminosity of $L_{(0.45-50.0\ \mathrm{keV})} = 6.8 \times 10^{36}$ erg s^{-1} ($\sim 3 - 4\%$ L_{Edd}).

power law cut off energy is 45^{+2}_{-1} keV. The inclination of the disk is $25^\circ \pm 4^\circ$. The parameter of most interest is the inner radius, R_{in}, which was found to be $1.9^{+1.4}_{-0.8}$ ISCO.

2.5.2 RGS

The RGS spectra showed prominent broad features rising above the continuum emission (modeled with an absorbed power law) at ~ 0.50 keV, ~ 0.57 keV, and ~ 0.65 keV corresponding to H-like N VII, He-like O VII, and H-like O VIII, respectively

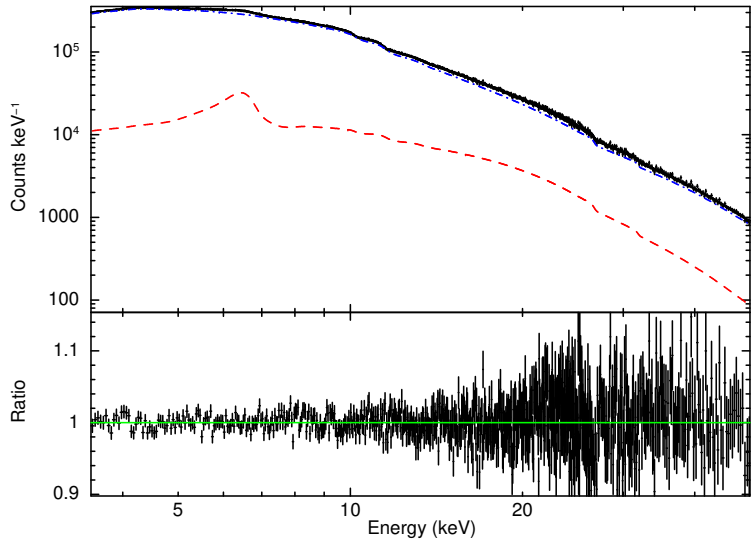

Figure 2.2 *NuSTAR* spectrum fit with TBNEW∗(RELXILL+GAUSS+GAUSS) (χ^2_{red} = 1.05). Gaussians were fit at 10.1 keV and 11.5 keV to account for instrumental response features. The red dashed line shows the reflection spectrum from the RELXILL model. The blue dot-dash line shows the power law component within the RELXILL model. The lower panel shows the ratio of the data to model. Spectrum has been rebinned for plotting purposes. Parameter values can be seen in the third column of Table 2.1.

(see Figure 2.3). Applying simple Gaussian lines place their centroid energy at 0.501± 0.002 keV, 0.568 ± 0.002 keV, and 0.655 ± 0.001 keV detected at the 3.2σ, 5.9σ, and 9σ confidence level. To test the robustness of these lines to different assumptions about the ISM we applied ISMABS (Gatuzz et al., 2014) with the same power law continuum. The abundance of each element is left as a free parameter so that the photoelectric absorption edges in ISMABS have the greatest possible opportunity to model the data in a way that would remove line-like features. The lines are still present in the spectra though their significance has decreased slightly with N VII line only being marginally significant. We believe the N VII to be a real feature but due to its location at the edge of the effective area of the detector we are unable to model it properly in subsequent fits. See Table 2.2 for the values obtained for the Gaussian lines with each absorption model.

Table 2.2 Emission Line in RGS Spectra

Abs Model	Ion	Lab E (keV)	$E_{centroid}$ (keV)	σ (keV) (10^{-2})	norm (10^{-4})	Significance (σ)
TBNEW	N VII	0.5003	0.501 ± 0.002	0.6 ± 0.2	1.6 ± 0.5	3.2
	O VII	0.574	0.568 ± 0.002	1.1 ± 0.2	2.9 ± 0.5	5.9
	O VIII	0.654	0.655 ± 0.001	1.2 ± 0.2	4.5 ± 0.5	9
ISMABS	N VII	0.5003	0.501 ± 0.002	0.6 ± 0.3	1.3 ± 0.5	2.6
	OVII	0.574	0.571 ± 0.001	0.8 ± 0.2	2.2 ± 0.5	4.4
	O VIII	0.654	0.654 ± 0.001	1.0 ± 0.2	3.4 ± 0.6	5.7

Note.— In TBNEW, all abundances were set to solar with $N_H = 2.0 \times 10^{21}$ cm^{-2} (Dickey & Lockman, 1990). Normalization is given in units of photons cm^{-2} s^{-1}. An absorbed power law was used to model the continuum. In ISMABS, elemental abundances were allowed to vary. The continuum was modeled with a power law of photon index 1.4.

We then applied the self consistent reflection model RELXILL in combination with TBNEW to describe the lines simultaneously. We allowed the abundance of O to be a free parameter in TBNEW to fully account for the O VIII K-edge at 0.53 keV that can be seen in Figure 3. The model was not able to account for the He-like O VII line with the other two H-like lines, likely due to the lower ionization parameter needed to create the line. We employ the relativistic line model RELLINE to describe this feature. The emissivity index, inclination, and inner radius were tied to the parameters in RELXILL. The limb parameter was set to 2 for consistency with RELXILL which assumes limb brightening. We only allowed the normalization and line energy to be free. The addition of the RELLINE component to RELXILL improves the overall fit by $\Delta\chi^2 = 147$ (for 2 d.o.f.). The resulting best fit can be seen in Table 2.1. The probability of the additional component improving the fit by chance was found to be negligibly small (3.19×10^{-24}) via an F-test. This is a 9.6σ improvement. The unfolded model can be seen in Figure 2.4. Figure 2.5 shows the RELXILL only model decomposed into the continuum and reflection components that are comprised in the model.

The cut energy and emissivity are not well constrained likely due to limited band width. Again, the photon index is consistent with the hard limit of 1.4 at the 90% confidence level. The absorption column is better constrained than in the previous fit with $N_H = 3.60 \pm 0.02 \times 10^{21}$ cm^{-2} with an oxygen abundance 1.77 ± 0.01 solar. The reflection fraction is higher than that of the *NuSTAR* spectrum meaning it is dominated by more reflection. The high reflection fraction reaffirms that the emission lines are reflection features. The inclination is several degrees lower than the inclination found in the higher energy range, but is generally consistent. The location of the inner disk ($1.2^{+3.3}_{-0.2}$ ISCO) is compatible with the iron line region.

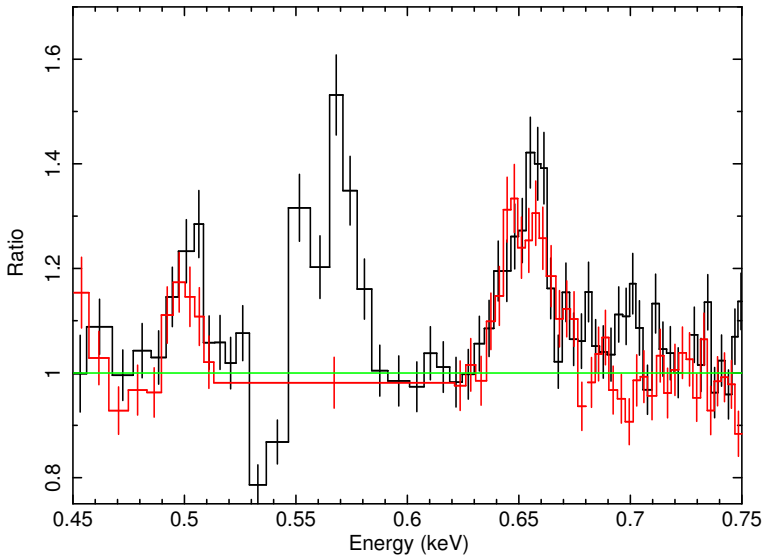

Figure 2.3 Ratio of the data to the continuum model for *XMM-Newton* RGS1 (black) and RGS2 (red) showing three emission lines (N VII, O VII, O VIII) and O VIII K edge. The continuum was modeled with a simple absorbed power law was fit over the energies of 0.45-2.1 keV. The N VII line is located near the edge of the effective area of the detector and therefore not modeled in subsequent fits. The data was rebinned and the x-axis was rescaled for plotting purposes.

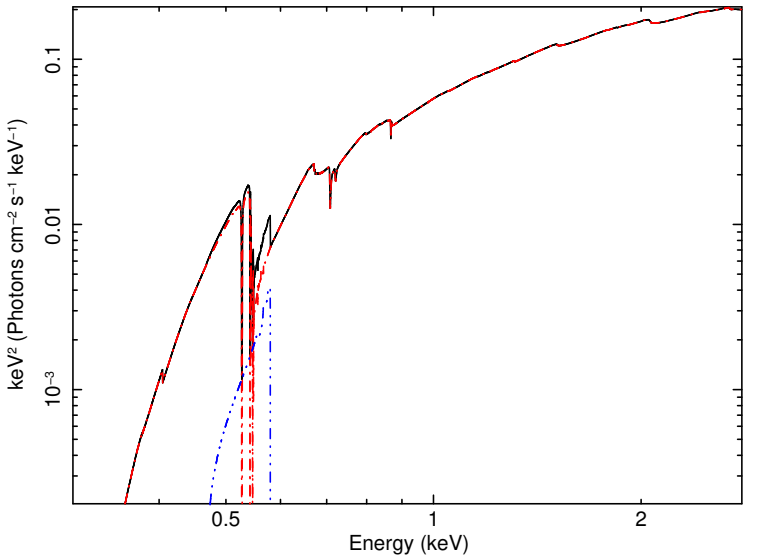

Figure 2.4 Unfolded model spectrum for *XMM-Newton* RGS. The blue component corresponds to RELLINE. The red component illustrates RELXILL which includes the power law.

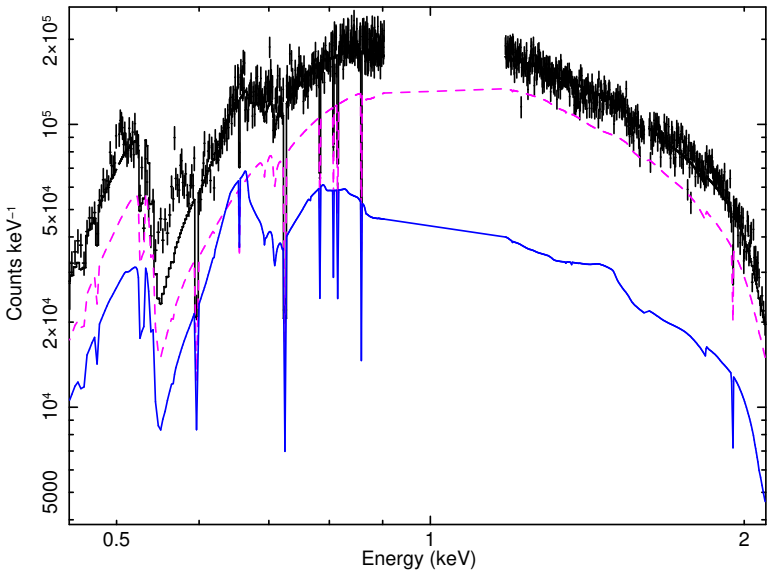

Figure 2.5 Decomposed RELXILL model spectrum for *XMM-Newton* RGS1 showing the reflection component (solid blue) and power law continuum (dashed purple). The RELLINE component is not shown to illustrate the models ability to fit the O VIII line.

2.5.3 NuSTAR+RGS

Due to the limited energy bandwidth of the RGS, we fit the *NuSTAR* and RGS together in order to obtain better estimates of the spectral parameters of interest. Tying the RGS data with the *NuSTAR* data provides an opportunity to fit multiple relativistic reflection features over a wide energy range (∼0.45-50.0 keV) and from different ionized regions in the disk. A constant was allowed to float between the two observations, but all other model parameters were tied. The constant was frozen at the value of 1.0 for *NuSTAR* and free to vary for RGS1 and RGS2. The constant for RGS1 was found to be $c = 1.234 \pm 0.006$ and $c = 1.182 \pm 0.005$ for RGS2. The model we first use is TBNEW∗(RELXILL+RELLINE+GAUSS+GAUSS) to model the relativistic reflection features with X-ray absorption along the line of sight. The Gaussian lines are to account for instrumental response features. See Table 2.1 and Figure 2.6.

Simultaneous fits return a neutral absorption column density $N_H = (3.45 \pm 0.01) \times 10^{21}$ cm^{-2} with a slight over abundance in oxygen, O= 1.71±0.01 solar. The emissivity

index, $q = 1.3 \pm 0.2$, suggests that a large area of the disk is being illuminated by a hard X-ray source. The ionization parameter being $log(\xi) = 2.75 \pm 0.01$ is within reason for an accreting source in the LHS (Cackett et al., 2010), although there are a number of cases where lower ionizations are found for a NS in the LHS (SAX J1808.4-3658: Papitto et al. 2009; Cackett et al. 2009, 4U 1705-44: D'Aì et al. 2010; Di Salvo et al. 2015). The iron abundance was allowed to be a free parameter and is consistent with the hard limit of 0.5 at the 90% confidence level. The photon index of the power law component that is responsible for producing the reflection spectrum is on the harder side with $\Gamma = 1.402 \pm 0.001$. The reflection fraction, f_{refl}, is 0.15 ± 0.01. The inclination agrees with the previous individual fit to the RGS data alone. The inner radius, $R_{in} \leq 1.85$ ISCO, is consistent within uncertainties with the individual fits to *NuSTAR* and RGS alone. Figure 2.7 shows the change in χ^2 when stepping the inner disk radius parameter out to 5 ISCO using the "steppar" command in XSPEC.

To explore the multiple ionization parameters that seem prevalent in the RGS data, we remove the RELLINE component and apply a double RELXILL model to the joint spectra. The idea is to be able to map the X-ray interactions with accretion disk radii. We tie the emissivity index, inclination, inner radius, photon index, and iron abundance between the two RELXILL components and allow the ionization, reflection fraction, and normalization to change between them. Parameter values can be seen in Table 2.3.

The higher ionization parameter agrees with the values obtained in the previous fits. The lower ionization value accounts for the production of the O VII line. The inner radius, $R_{in} < 4.1$ ISCO, agrees with the value obtained in the previous model when using RELLINE to describe the O VII line, which does not make assumptions about the underlying gas physics like RELXILL does. The reflection fraction for each component are consistent with one another, though the normalization is not well constrained. We do not expect these two different ionization states to occur at the same

radii, and as such, tried to free the inner radius in each of the RELXILL components to map the radius at which the X-ray interactions with the disk occurred. We were unable to obtain radii that were statistically distinct. The goodness of fit of the double RELXILL model is comparable to the simpler fit with just one RELXILL component and RELLINE. We chose to use the parameter values from the simpler model fits in subsequent calculations.

If the inner disk is truncated substantially above the neutron star surface itself, as allowed by our upper limits on R_{in}, then the disk may instead be truncated by a boundary layer extending from the stellar surface. The upper limit on R_{in} would require a boundary layer that is a few times the stellar radius in size. Alternatively, the disk could be truncated by magnetic pressure. We can place an upper limit on the strength of the field using the upper limit of $R_{in} = 1.85$ ISCO. Assuming a mass of 1.4 $M_\odot$, taking the distance to be 5.8 kpc (Krimm et al., 2015a), and using the unabsorbed flux from 0.45-50.0 keV of 1.71×10^{-9} erg cm^{-2} s^{-1} as the bolometric flux, we can determine the magnetic dipole moment, μ, from Equation (1) taken from Cackett et al. (2009).

$$\mu = 3.5 \times 10^{23}\ k_A^{-7/4}\ x^{7/4} \left(\frac{M}{1.4 M_\odot}\right)^2 \times \left(\frac{f_{ang}}{\eta} \frac{F_{bol}}{10^{-9} \text{erg cm}^{-2}\ \text{s}^{-1}}\right)^{1/2} \frac{D}{3.5\text{kpc}}\ \text{G cm}^3 \tag{2.1}$$

If we make the same assumptions about geometry and accretion efficiency (i.e. $k_A = 1$, $f_{ang} = 1$, and $\eta = 0.1$), then $\mu \simeq 1.62 \times 10^{26}$ G cm^3. This corresponds to a magnetic field strength of $B \simeq 3.2 \times 10^8$ G at the magnetic poles for a NS of 10 km. Moreover, if we assume a different conversion factor $k_A = 0.5$ (Long et al., 2005) then the magnetic field strength at the poles would be $B \simeq 1.0 \times 10^9$ G. We note, however, that coherent pulsations have not been detected in 1RXS J1804, and the source is not identified as a pulsar.

However, if the disk does extend closer to the ISCO, then we can place a lower

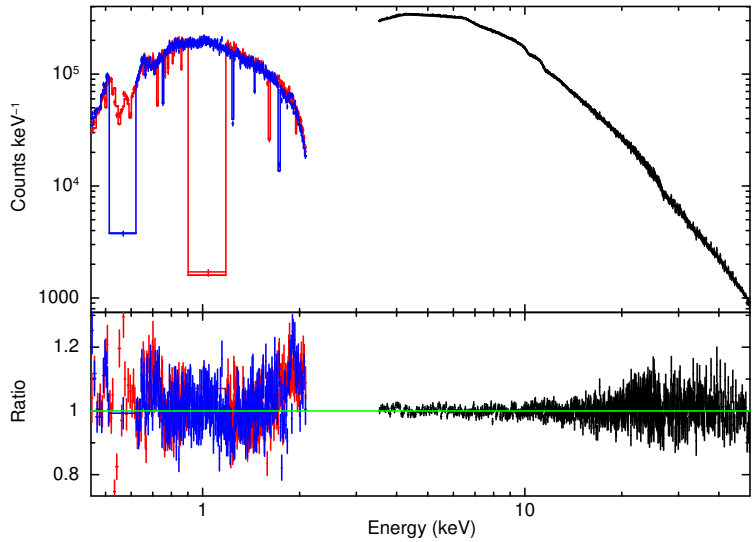

Figure 2.6 Joint fit of RGS and *NuSTAR* with TBNEW*(RELXILL+GAUSS+GAUSS +RELLINE) ($\chi^2_{red} = 1.34$). The additional RELLINE parameter is needed to model the He-like O VII line. Gaussians were fit at 10.1 keV and 11.5 keV to account for instrumental response features. Spectrum has been rebinned for plotting purposes. Parameter values can be seen in the fifth column of Table 2.1.

limit on the gravitational redshift from the NS surface, z_{NS}. Gravitational redshift is given by $z+1 = 1/\sqrt{1-2GM/R_{in}c^2}$. For $R_{in} = 1.1$ ISCO, assuming a 1.4 $M_\odot$ NS and $a_* = 0$, the $z_{NS} \geq 0.2$ given that the neutron star is smaller than the radius of the disk. Our measurement for R_{in} does extend down to 1 ISCO. If this were the case, then the $z_{NS} \geq 0.22$ for a 12 km NS.

To be thorough, we fix the spin to 0.12 and 0.24 to test our assumption that the position of the inner disk radius changes slowly for low spin parameters as per Miller et al. 2013. The inner radius changes only marginally for the highest spin of $a_* = 0.24$, confirming that our fits are not highly dependent upon the choice of spin parameter.

2.6 Discussion

We have analyzed observations taken of the NS LMXB 1RXS J180408.9-34205 in the hard spectral state. We find clear evidence of a prominent iron line at 6.4

Table 2.3 Double Relxill Fitting of *NuSTAR* and RGS

Component	Parameter	Values
TBNEW	$N_H(10^{22})$	0.340 ± 0.003
	A_O	1.689 ± 0.03
RELXILL	$q_{in} = q_{out}$	< 1.2
	a'_*	0
	$i(^\circ)$	$18.11^{+0.3}_{-0.2}$
	$R_{in}(ISCO)$	$1.13^{+2.98}_{-0.13}$
	$R_{out}(R_g)'$	400
	z'	0
	Γ	< 1.41
	$log(\xi)_1$	2.9 ± 0.1
	$log(\xi)_2$	1.5 ± 0.2
	A_{Fe}	< 0.54
	$E_{cut}(keV)$	$45.1 \pm 0.$
	$f_{refl,1}$	0.2 ± 0.1
	$f_{refl,2}$	0.22 ± 0.02
	angleon$'$	1
	norm$_1$ (10^{-2})	$4.73^{+2.2}_{-1.3}$
	norm$_2$ (10^{-2})	$4.68^{+4.7}_{-1.0}$
	χ^2_ν(dof)	1.36 (3962)

$'$ = fixed

Note.— Errors are quoted at ≥ 90 % confidence level. Setting angleon=1 takes the inclination into account when modeling reflection. A constant was allowed to float between *NuSTAR* and the RGS data. The *NuSTAR* was frozen at the value of 1.0, RGS1 was fit at 1.25 ± 0.01, and RGS2 was fit at 1.19 ± 0.01.

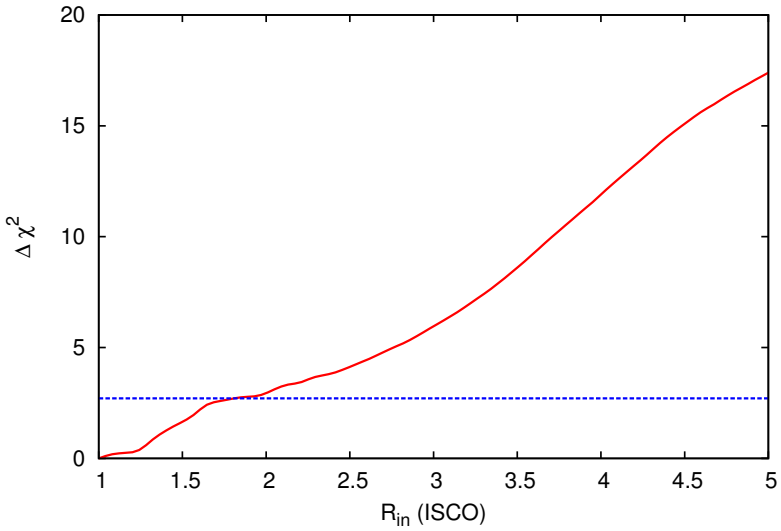

Figure 2.7 The change in goodness-of-fit versus inner disk radius for the *NuSTAR* +RGS column in Table 2.1 taken over 50 evenly spaced steps generated with XSPEC "steppar". The inner disk radius was held constant at each step while the other parameters were free to adjust. The blue dashed line shows the 90% confidence level.

keV in the *NuSTAR* spectra and three reflection lines in the *XMM-Newton*/RGS corresponding to N VII, O VII, and O VIII. This is the first time that a broad iron line has been detected in conjunction with multiple lower energy lines in the RGS.

We have found that when tying the *NuSTAR* and RGS data together, 1RXS J1804 has an $R_{in} \leq 1.85$ ISCO with an inclination between 18°-29°. This translates to ≤ 22.2 km for a 1.4 $M_{\odot}$ NS with $a_* = 0$. Further, we are close to being able to map how ionization varies with radius in the disk. Individual fits to *NuSTAR* and RGS suggest that the O region may be located farther out in the disk than the Fe line region, but uncertainties do not exclude their mutual location.

There are a growing number of NS LMXB with small inner radii measurements, such as Serpens X-1 (Miller et al. 2013; Chiang et al. 2016a) and 4U 1608-52 (Degenaar et al., 2015). These objects were in a higher spectral state with softer photon indices that required the addition of thermal components in contrast to 1RXS J1804. Both objects had relativistic iron lines emerging from $R_{in} = 6.2 - 7.2\ R_g$ (Miller et al.,

2013) for Serpens X-1 and $R_{in} = 7 - 10\ R_g$ (Degenaar et al., 2015) for 4U 1608-52. Additionally, Cackett et al. (2010) looked at 7 other NS LMXBs in addition to Serpens X-1. Nearly all of the objects were found to have an inner radius between $6 - 15\ R_g$. The relatively small inner radius measurement obtained for 1RXS J1804 suggests that the disk does not necessarily become highly truncated in the hard state. Similar behavior for the location of the inner radius was also seen for 4U 1705-44 (Di Salvo et al., 2015). The disk radius in the hard state was comparable with the soft state.

The ionization parameter for 1RXS J1804 is comparable to the values seen for other NS reflections studies for the iron line region, $2.3 < log(\xi) < 4.0$ (Cackett et al. 2010; Miller et al. 2013; Degenaar et al. 2015). However, other studies find lower ionization parameter values for a NS in the LHS (Papitto et al. 2009; Cackett et al. 2009; D'Aì et al. 2010; Di Salvo et al. 2015). Though it is likely that some of the emergent flux in the iron line region for 1RXS J1804 is partially from a region of lower ionization. Again, we are close to tracing out the ionization as a function of disk radius and will push toward this goal in future work by achieving better overall data quality (higher signal to noise). We will focus on obtaining deeper observation with RGS for objects like 1RXS J1804 in the hard state with little to no thermal component to drown out the low energy reflection features.

If the disk is not truncated at the stellar surface, it may be truncated at the magnetospheric radius. Using conservative methods, we find that the upper limit on R_{in} implied by our fits would limit the magnetic field at the poles to $B \leq (0.3 - 1.0) \times 10^9$ G (magnetic field strength at the poles is twice as large as at the magnetic equator). However, pulsations are not seen in this source and thus our estimate should be considered an upper limit. An alternative explanation for disk truncation may be the presence of a boundary layer between the NS and inner disk (see D'Aì et al. 2010 for more details).

CHAPTER III

A Hard Look at the Neutron Stars and Accretion Disks in 4U 1636-53, GX 17+2, and 4U 1705-44 with *NuSTAR*

3.1 Preface

This chapter appears in the Astrophysical Journal, Volume 836, page 140 (Ludlam et al., 2017a) and is co-authored by Jon M. Miller, Matteo Bachetti, Didier Barret, Allison C. Bostrom, Edward M. Cackett, Nathalie Degenaar, Tiziana Di Salvo, Lorenzo Natalucci, John A. Tomsick, Frits Paerels, and Michael L. Parker. The paper is reproduced here under the non-exclusive rights of republication granted by the American Astronomical Society to the authors of the paper.

3.2 Abstract

We present *NuSTAR* observations of neutron star (NS) low-mass X-ray binaries: 4U 1636-53, GX 17+2, and 4U 1705-44. We observed 4U 1636-53 in the hard state, with an Eddington fraction, $F_{\rm Edd}$, of 0.01; GX 17+2 and 4U 1705-44 were in the soft state with fractions of 0.57 and 0.10, respectively. Each spectrum shows evidence for a relativistically broadened Fe K_{α} line. Through accretion disk reflection modeling,

we constrain the radius of the inner disk in 4U 1636-53 to be $R_{in} = 1.03 \pm 0.03$ ISCO (innermost stable circular orbit) assuming a dimensionless spin parameter $a_* = cJ/GM^2 = 0.0$, and $R_{in} = 1.08 \pm 0.06$ ISCO for $a_* = 0.3$ (errors quoted at 1 σ). This value proves to be model independent. For $a_* = 0.3$ and $M = 1.4\ M_\odot$, for example, 1.08 ± 0.06 ISCO translates to a physical radius of $R = 10.8 \pm 0.6$ km, and the neutron star would have to be smaller than this radius (other outcomes are possible for allowed spin parameters and masses). For GX 17+2, $R_{in} = 1.00 - 1.04$ ISCO for $a_* = 0.0$ and $R_{in} = 1.03 - 1.30$ ISCO for $a_* = 0.3$. For $a_* = 0.3$ and $M = 1.4\ M_\odot$, $R_{in} = 1.03 - 1.30$ ISCO translates to $R = 10.3 - 13.0$ km. The inner accretion disk in 4U 1705-44 may be truncated just above the stellar surface, perhaps by a boundary layer or magnetosphere; reflection models give a radius of 1.46-1.64 ISCO for $a_* = 0.0$ and 1.69-1.93 ISCO for $a_* = 0.3$. We discuss the implications that our results may have on the equation of state of ultradense, cold matter and our understanding of the innermost accretion flow onto neutron stars with low surface magnetic fields, and systematic errors related to the reflection models and spacetime metric around less idealized neutron stars.

3.3 Introduction

The equation of state (EOS) of ultradense matter is not yet known. Earth laboratories are unable to replicate the necessary environment to constrain the EOS. Thus, the only way to study matter under these extreme conditions is through observations of neutron stars (NS). The EOS sets the mass and radius of the NS. Theoretical mass-radius tracks have been compiled for different theoretical models (see Lattimer & Prakash 2016 for a review). Three-body interactions between nucleons make the radius of the NS the most important quantity in determining the EOS because it does not change quickly as a function of mass. Hence, constraining the radius of the NS can, in turn, lead to a determination of the EOS of the cold, dense matter under

extremely dense physical conditions (Lattimer, 2011).

Low-mass X-ray binaries (LMXBs) are one setting in which we can attempt to constrain the EOS through observations. LMXBs consist of a roughly stellar-mass companion that transfers matter onto a compact object via Roche-lobe overflow. Broad iron line profiles have been seen in these accreting systems that harbor a black hole (BH; e.g. Fabian et al. 1989; Miller 2002, 2007; Reis et al. 2008, 2009a) or NS (e.g. Bhattacharyya & Strohmayer 2007; Papitto et al. 2008; Cackett et al. 2008, 2009, 2010; Di Salvo et al. 2009, 2015; Egron et al. 2013; Miller et al. 2013) as the primary accreting compact object. LMXBs are ideal laboratories for conducting radius measurements through reflection studies since all accretion occurs via the disk, as opposed to their high-mass X-ray binary (HMXB) counterparts which can accrete via stellar winds.

X-ray disk lines are produced from an external hard X-ray source irradiating the accretion disk. In the case of NSs, the hard X-ray source could be a hot corona, the stellar surface, or a boundary layer and may be thermal or non-thermal in nature. Regardless of the nature of the hard X-ray emission, the asymmetrically broadened profile of the Fe K_α line gives a direct measure of the position of inner disk since the effects of gravitational redshift and Doppler redshift/boosting on the emission line become stronger closer to the compact object (Fabian et al., 1989).

The Fe K_α line in NS LMXBs can set an upper limit for the radius of NS since the disk must truncate at or before the surface (Cackett et al. 2008, 2010; Reis et al. 2009b; Miller et al. 2013; Degenaar et al. 2015). Since the magnetic field could also truncate the accretion disk, studies of disk reflection can also be used to set an upper limit on the magnetic field strength (Cackett et al. 2009; Papitto et al. 2009; Miller et al. 2011; Degenaar et al. 2014, 2016; King et al. 2016; Ludlam et al. 2016).

We analyze *NuSTAR* (Harrison et al., 2013) observations of NS LMXBs 4U1636-53, GX 17+2, and 4U1705-44. 4U 1636-53 and 4U 1705-44 are categorized as atoll

sources while GX 17+2 is a "Z" source, according to the classification of Hasinger & van der Klis (1989). Atoll sources have lower luminosities ($\sim 0.01 - 0.2\ L_{\rm Edd}$) than Z sources (see Done et al. (2007) for a review). The Z sources have soft X-ray spectra that can be described by two thermal components (multicolor disk blackbody and single temperature blackbody; Lin et al. 2007). Atolls can have soft or hard spectra with transitional phases in between. The hard state can be modeled well by a powerlaw and thermal component when needed (Lin et al., 2007).

Further, the spectral state may be associated with the level of disk truncation (Done et al., 2007). A study of 4U 1608-52 by Gierliński & Done (2002) found that at low luminosity the accretion disk was truncated while at high luminosity the inner radius of the disk moved inwards. Pintore et al. (2016) found similar behavior for SAX J1748.9-2021. However, Sanna et al. (2014) found that the inner disk did not seem to be correlated with the spectral state for 4U 1636-53. The inner disk radius of Serpens X-1 (Ser X-1) also does not appear to change much for a range of luminosities (Chiang et al., 2016b).

4U 1636-53 was in the hard state at the time of the *NuSTAR* observation, while GX 17+2 and 4U 1705-44 were in the soft state. We focus on constraining the inner disk radius in these sources and the implications this has on the EOS for ultradense, cold matter. The following sections (§3.3.1, 3.3.2, 3.3.3) give a brief introduction about each source. Section 3.4 provides details on the observations of each source and how the data were reduced. Section 3.5 presents our analysis and results. Section 3.6 discusses those results and we conclude in section 3.7.

3.3.1 4U 1636-53

4U 1636-53 is a well studied, persistent LMXB that exhibits Type 1 X-ray bursts and has a spin frequency of 581 Hz (Zhang et al. 1997; Strohmayer & Markwardt 2002). The source is located a maximum of 6.6 kpc away from inspection of the Type

1 X-ray bursts (assuming the brightest type-I X-ray bursts hit the Eddington limit; Galloway et al. 2008). The companion star is a 0.4 $M_{\odot}$, 18th magnitude star with an orbital period of 3.8 hours (Pedersen et al. 1982; van Paradijs et al. 1990). kHz quasi-periodic oscillations (QPOs) suggest that 4U 1636-53 may harbor a NS as large as 2 $M_{\odot}$ (Barret et al. 2006; Casares et al. 2006). The system regularly undergoes state transitions on ~ 40 day time intervals (Shih et al., 2005).

Reflection studies suggest this source has a high inclination, but a lack of dips in the X-ray light curve limits the inclination $\sim 70^{\circ}$ (Frank et al. 1987; Casares et al. 2006; Sanna et al. 2013). Pandel et al. (2008) found the inner disk radius was consistent with the innermost stable circular orbit (ISCO) when looking at observations taken with *XMM-Newton* and *RXTE* while in the transitional and soft state. Cackett et al. (2010) found larger inner disk radii at $\sim 8 \pm 4$ ISCO (assuming $a_* = 0$) when applying blurred reflection models to the low flux state, but values consistent with the ISCO were measured in the soft state. Additionally, Sanna et al. (2013) analyzed the source in the soft and transitional states with two additional observations. They measure the inner disk radius to be as large as 4.45 ISCO in low flux states, which is smaller but consistent with Cackett et al. (2010). Lyu et al. (2014) used observations from *Suzaku*, *XMM-Newton*, and *RXTE* to see if the inner disk radius inferred from Fe line changed over flux states. They used available disk line models (DISKLINE, LAOR, KRYLINE) to account for relativistic broadening and found that the Fe line did not change significantly. They conclude that the line is broadened by mechanisms other than just relativistic broadening, though the data are consistent with a disk remaining at the ISCO if timing parameters trace the mass accretion rate rather than the inner radius.

3.3.2 GX 17+2

GX 17+2 is a burster located a maximum distance of 13.0 kpc (Galloway et al., 2008) with a spin frequency of 293.2 Hz (Wijnands et al., 1997). The counterpart of GX 17+2 is not known currently. It may be NP Ser (Tarenghi & Reina, 1972) or star "A" proposed by Deutsch et al. (1999) from optical and IR variability studies. However, Callanan et al. (2002) proposed that the IR variability could be explained by synchrotron flares. The system has an inclination of less than 45° (Cackett et al. 2010, 2012). Di Salvo et al. (2000) performed the first extensive spectral analysis of GX 17+2. They were able to limit the radius of the NS between 10-19 km based upon comptonization of photons within their spectra. Cackett et al. (2010) found a similarly small limit through modeling the Fe reflection in the accretion disk.

3.3.3 4U 1705-44

4U 1705-44 is a persistently bright source that shows Type 1 X-ray bursts (Langmeier et al., 1987) which place it at a maximum distance of 7.8 kpc (Galloway et al., 2008). The source has been observed in both the hard and soft states (Barret & Olive 2002; Piraino et al. 2007). Broad Fe emission has been in each of these states. The inclination of the system is between $20° - 50°$ (Piraino et al., 2007). Di Salvo et al. (2009) found evidence for multiple emission lines for SXVI, Ar XVIII, and Ca XIX in addition to iron in observations taken with *XMM-Newton*. These lines gave an inner disk radius of 2.3 ± 0.3 ISCO (assuming $a_* = 0$). Reis et al. (2009b) found an inner disk radius of $1.75^{+0.17}_{-0.28}$ ISCO when using observations obtained with *Suzaku*. Cackett et al. (2010) used both *XMM-Newton* and *Suzaku* observations and found that the inner disk ranged from 1.0-6.5 ISCO. The inner disk of 4U 1705-44 appears to be truncated in many studies though the degree of truncation varies.

Table 3.1 *NuSTAR* Observation Information

Source	Obs ID	Date	Net Exp (ks)	Net Rate (cts/s)
4U 1636-53	30101024002	06/06/2015	19.2	40
GX 17+2	30101023002	03/22/2016	23.3	361
4U 1705-44	30101025002	04/22/2016	28.7	174

3.4 Observations and Data Reduction

The details of each *NuSTAR* observation are listed in Table 3.1. Lightcurves and spectra were created using a 120″ circular extraction region centered around the source using the NUPRODUCTS tool from NUSTARDAS v1.5.1 with CALDB 20160421. A background was generated and subtracted using another region of the same dimension in a region away from the source. There were a total of 6 Type 1 X-ray bursts present in the lightcurves for 4U 1636-53 and a single Type 1 X-ray burst for 4U 1705-44. We will report on the bursts in a separate paper. We created good time intervals (GTIs) to remove ∼10 – 150 s after the initial fast rise (depending on the duration of the individual burst) to separate these from the steady emission. These GTIs were applied during the generation of the spectra for both the FPMA and FPMB. Initial modeling of the persistent emission spectra with a constant, fixed to 1 for the FPMA and allowed to float for the FPMB, found the floating constant to be within 0.95-1.05 in each case. We proceeded to combine the two source spectra, background spectra, and ancillary response matrices via ADDASCASPEC. We use ADDRMF to create a single redistribution matrix file. The spectra were grouped using GRPPHA to have a minimum of 25 counts per bin (Cash, 1979).

3.5 Spectral Analysis and Results

We use XSPEC version 12.8.1 (Arnaud, 1996) in this work. All errors are quoted at 1σ (68%) confidence level and were calculated from Monte Carlo Markov Chain (MCMC) of length 100,000. We perform fits over the energy range in which the

spectrum is not background dominated for each source. We account for the neutral column hydrogen density along the line of sight via TBABS (Wilms et al., 2000). The solar abundance was set to WILM (Wilms et al., 2000) and VERN cross sections (Verner et al., 1996) were used.

We experimented with different phenomenological one, two, and three-component models to describe the spectral continua. None of the sources required three components. The continuum of the spectrum obtained from 4U 1636−53 was well described with a cut-off power-law model. The cut-off energy may reflect the electron temperature of the corona, and the simple continuum component may only be an approximation of a region dominated by Comptonization. The spectral continua of GX 17+2 and 4U 1705−44 were well described by a combination of disk blackbody (Mitsuda et al., 1984) and simple blackbody components. It is possible to infer radii from both disk blackbody and simple blackbody components; however, it is also clear that scattering can harden emergent spectra and cause falsely small radii to be inferred (e.g., London et al. 1986; Shimura & Takahara 1995; Merloni et al. 2000). Low temperature, optically-thick Comptonization can sometimes be approximated as a blackbody; it is likely that our simple blackbody component accounts for this process in the boundary layer (e.g., Gilfanov et al. 2003). Given the many complexities and possible distortions, we do not look to the continua for robust physical inferences; rather, we utilize disk reflection for this purpose.

To properly describe the reflection features and relativistic effects present in the data for 4U 1636-53 we employ the model RELXILL (García et al., 2014). This model self-consistently accounts for X-ray reflection and relativistic ray tracing for a power law irradiating an accretion disk while properly taking into account the inclination in the reflection from the disk. The parameters of this model are as follows: inner emissivity (q_{in}), outer emissivity (q_{out}), break radius (R_{break}) between the two emissivities, spin parameter ($a_* = cJ/GM^2$), inclination if the disk (i), inner radius of the

disk (R_{in}) in units of ISCO, outer radius of the disk (R_{out}), redshift (z), photon index of the power law(Γ), log of the ionization parameter ($log(\xi)$), iron abundance (A_{Fe}), cut off energy of the power law (E_{cut}), reflection fraction (f_{refl}), and normalization.

We apply BBREFL (Ballantyne, 2004) to GX 17+2 and 4U 1705-44 in order to model the emergent reflection emission from a disk assuming an irradiating blackbody continuum, and convolve it with RELCONV (Dauser et al., 2010). The iron abundance in BBREFL comes in two flavors: solar abundance and twice solar abundance. The parameters of BBREFL are as follows: log of the ionization parameter ($log(\xi)$), temperature of the incident blackbody in keV (kT), iron abundance (A_{Fe}), reflection fraction (f_{refl}), redshift (z), and normalization. The parameters of RELCONV are as follows: inner emissivity index (q_{in}), outer emissivity index (q_{out}), dimensionless spin parameter (a_*), inner disk radius in units of ISCO (R_{in}), and outer disk radius in units of gravitational radii (R_{out}).

Additionally, we use REFLIONX (Ross & Fabian, 2005) to test the robustness of our results obtained with RELXILL and the nature of the Fe K_α line in our BBREFL. In the case of the 4U 1636-53, we use a version of REFLIONX[1] that has a variable high energy cut-off. We convolve this model with the relativistic blurring kernel KERRCONV (Brenneman & Reynolds, 2006). This provides a completely model independent check to values obtained with RELXILL. In the case of GX 17+2 and 4U 1705-44, we have a version of REFLIONX[2] that has been modified to assume a blackbody is illuminating the disk. This reflection model does not represent an independent check on BBREFL since they are derived from the same parent code (Ross & Fabian, 1993). It can, however, be used to verify that the Fe K_α line is dynamically broadened and not a result of gas broadening. This is because the REFLIONX model contains additional physics that accounts for gas effects. It has a broader range of elements, charge states, and ionization while it accounts for the local radiation field at each point. Hence, if

[1]https://www-xray.ast.cam.ac.uk/∼mlparker/reflionx_models/reflionx_hc.mod
[2]http://www-xray.ast.cam.ac.uk/∼mlparker/reflionx_models/reflionx_bb.mod

we are able to obtain similar values for various parameters, then the line profile is dynamical in origin.

A few reasonable conditions were enforced when making fits with RELXILL and RELCONV. First, we tie the outer emissivity index, q_{out} to the inner emissivity index, q_{in}, to create a constant emissivity index. Next, we fix the spin parameter, a_* (where $a_* = cJ/GM^2$), in the model RELCONV to 0.0 and 0.3 in the subsequent fits since NS in LMXBs have $a_* \leq 0.3$ (Miller et al. 2011; Galloway et al. 2008). This does not hinder our estimate of the inner radius since the position of the ISCO is relatively constant for low spin parameters (corrections for frame-dragging for $a_* < 0.3$ give errors $\ll 10\%$; Miller et al. 1998). Further, the outer disk radius has been fixed to 990 R_g (where $R_g = GM/c^2$). In the case that we use KERRCONV, we tie the emissivity indices to create one emissivity index and fix the outer disk radius to 400 ISCO.

3.5.1 4U 1636-53

As noted above, initial fits were performed from 3.0-50.0 keV with an absorbed cut-off power law to model the continuum emission. Although the continuum is well described, this model gives a poor fit ($\chi^2/dof = 2435.47/876$) since it does not account for the reflection present within the spectrum. A broad Fe K_α line centered ~ 7 keV with a red wing extending to lower energies and blue wing extending up to 9 keV, implying a high inclination, can be seen in the top panel of Figure 3.1. The addition of a thermal component improved the overall fit, but the temperature was unfeasibly low for the sensitivity of *NuSTAR* (0.18 ± 0.02 keV) and the normalization was not physically possible ($3.6^{+23.2}_{-3.4} \times 10^7$), hence we excluded it from subsequent modeling.

We performed two fits with TBABS*RELXILL for the different spin values. Each of these provide a significantly better fit (28σ improvement) over the absorbed cut-off

Table 3.2 4U 1636 Relxill Modeling for Different Spin Parameters

Component	Parameter	RELXILL	
TBABS	$N_H(10^{22})^{\dagger}$	0.3	0.3
RELXILL	q	2.25 ± 0.05	2.19 ± 0.04
	$a_*^{\dagger}$	0.0	0.3
	$i(^\circ)$	78.2 ± 1.67	78.5 ± 1.22
	$R_{in}(ISCO)$	1.03 ± 0.03	1.08 ± 0.06
	$R_{out}(R_g)^{\dagger}$	990	990
	$R_{in}(km)$	12.4 ± 0.4	10.8 ± 0.6
	$z^{\dagger}$	0.0	0.0
	Γ	1.74 ± 0.01	1.74 ± 0.01
	$log(\xi)$	3.3 ± 0.1	3.26 ± 0.06
	A_{Fe}	4.9 ± 0.1	4.8 ± 0.1
	$E_{cut}(keV)$	20.5 ± 0.3	20.5 ± 0.3
	f_{refl}	0.42 ± 0.05	0.40 ± 0.04
	norm (10^{-3})	2.21 ± 0.06	2.22 ± 0.03
	$F_{\mathrm{unabs,3.0-50.0\ keV}}$	8.9 ± 0.2	8.9 ± 0.1
	$L_{\mathrm{unabs,3.0-50.0\ keV}}$	4.6 ± 0.1	4.63 ± 0.06
	$F_{\mathrm{unabs,0.5-50.0\ keV}}$	12.8 ± 0.3	12.8 ± 0.2
	$L_{\mathrm{unabs,0.5-50.0\ keV}}$	6.7 ± 0.2	6.67 ± 0.09
	χ^2_ν(dof)	1.06 (862)	1.06 (862)

† = fixed

Note.— Errors are quoted at 1σ confidence level. The absorption column density was fixed to the Dickey & Lockman (1990) value and given in units of cm^{-2}. The spin parameter is pegged at an upper limit of 0.3. The inner disk radius in units of km assumes a NS mass of 1.4 $M_\odot$. Flux is given in units of 10^{-10} ergs cm^{-2} s^{-1}. Luminosity is calculated at a maximum of 6.6 kpc and given in units of 10^{36} ergs s^{-1}.

Table 3.3 4U 1636 Reflionx Modeling for Different Spin Parameters

Component	Parameter	REFLIONX	
TBABS	$N_H(10^{22})^{\dagger}$	0.3	0.3
CUTOFFPL	Γ	1.74 ± 0.01	1.75 ± 0.01
	$E_{cut}(keV)$	20.7 ± 0.3	20.6 ± 0.3
	norm	0.20 ± 0.01	0.20 ± 0.01
KERRCONV	q	2.33 ± 0.04	2.28 ± 0.05
	$a_*^{\dagger}$	0.0	0.3
	$i(^\circ)$	78.6 ± 1.2	78.3 ± 1.2
	$R_{in}(ISCO)$	1.02 ± 0.02	1.08 ± 0.06
	$R_{out}(ISCO)^{\dagger}$	400	400
	$R_{in}(km)$	12.2 ± 0.2	10.8 ± 0.6
REFLIONX	ξ	1800 ± 600	1100 ± 500
	A_{Fe}	4.4 ± 0.5	4.6 ± 0.3
	f_{refl}	0.6 ± 0.2	0.6 ± 0.3
	$z^{\dagger}$	0	0
	norm (10^{-7})	2.7 ± 0.9	6.8 ± 4.0
	$F_{\text{unabs,3.0-50.0 keV}}$	9 ± 3	9 ± 5
	$L_{\text{unabs,3.0-50.0 keV}}$	5 ± 2	5 ± 3
	$F_{\text{unabs,0.5-50.0 keV}}$	14 ± 5	14 ± 8
	$L_{\text{unabs,0.5-50.0 keV}}$	7 ± 2	7 ± 4
	χ^2_ν(dof)	1.25 (862)	1.23 (862)

† = fixed

Note.— Errors are quoted at 1σ confidence level. The absorption column density was fixed to the Dickey & Lockman (1990) value and given in units of cm^{-2}. The spin parameter is pegged at an upper limit of 0.3. The REFLIONX model used has a variable high energy cut off which we tied to the cut off energy of the cut off power law used to model the continuum emission. Additionally, we tied the photon index between REFLIONX and CUTOFFPL. The inner disk radius in units of km assumes a NS mass of 1.4 $M_\odot$. Flux is given in units of 10^{-10} ergs cm^{-2} s^{-1}. Luminosity is calculated at a maximum of 6.6 kpc and given in units of 10^{36} ergs s^{-1}.

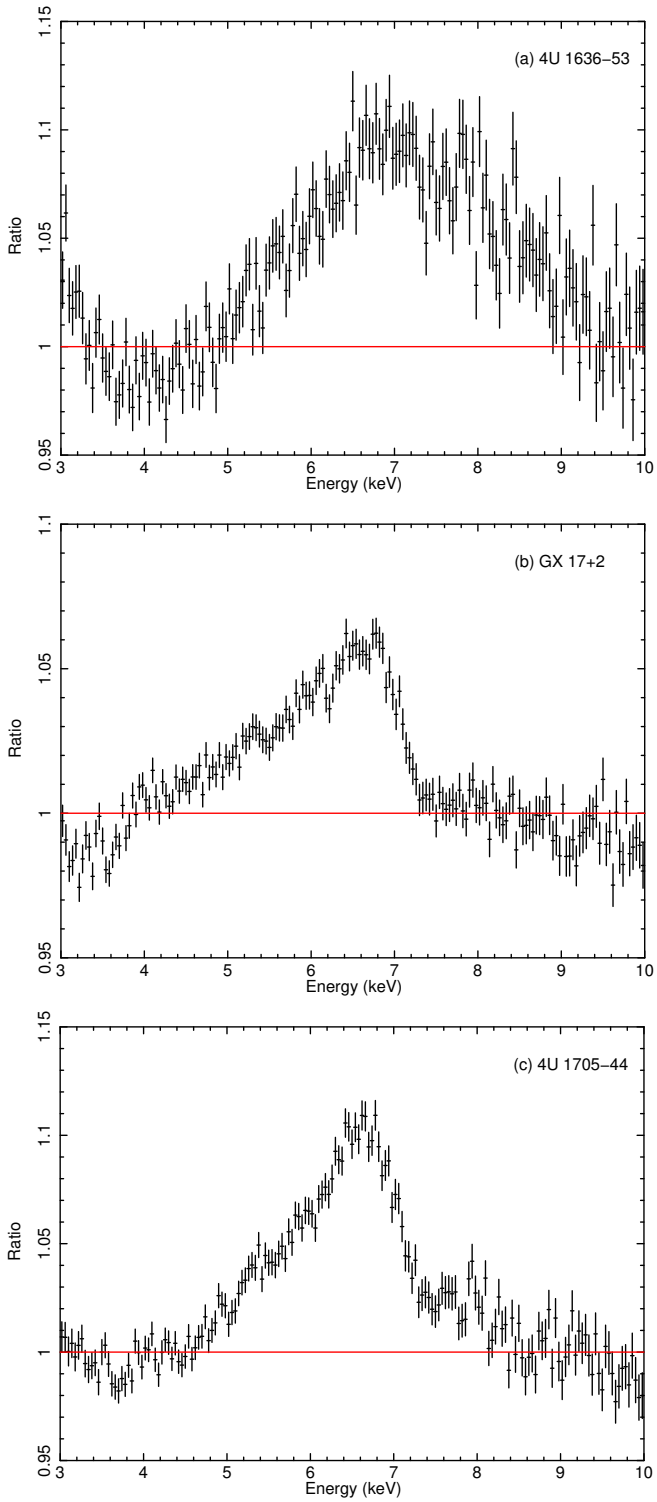

Figure 3.1 Ratio of the data to the continuum model in the Fe K band for *NuSTAR* observation of 4U 1636-53, GX 17+2, and 4U 1705-44. The iron line region from 5-8 keV was ignored to prevent the feature from skewing the fit. The data were rebinned for plotting purposes. (a) A simple cut-off power law was fit over the energies of 3.0-5.0 keV and 8.0-50.0 keV. For panels (b) and (c), a simple disk blackbody and single temperature blackbody was fit over the energies of 3.0-5.0 keV and 8.0-30.0 keV.

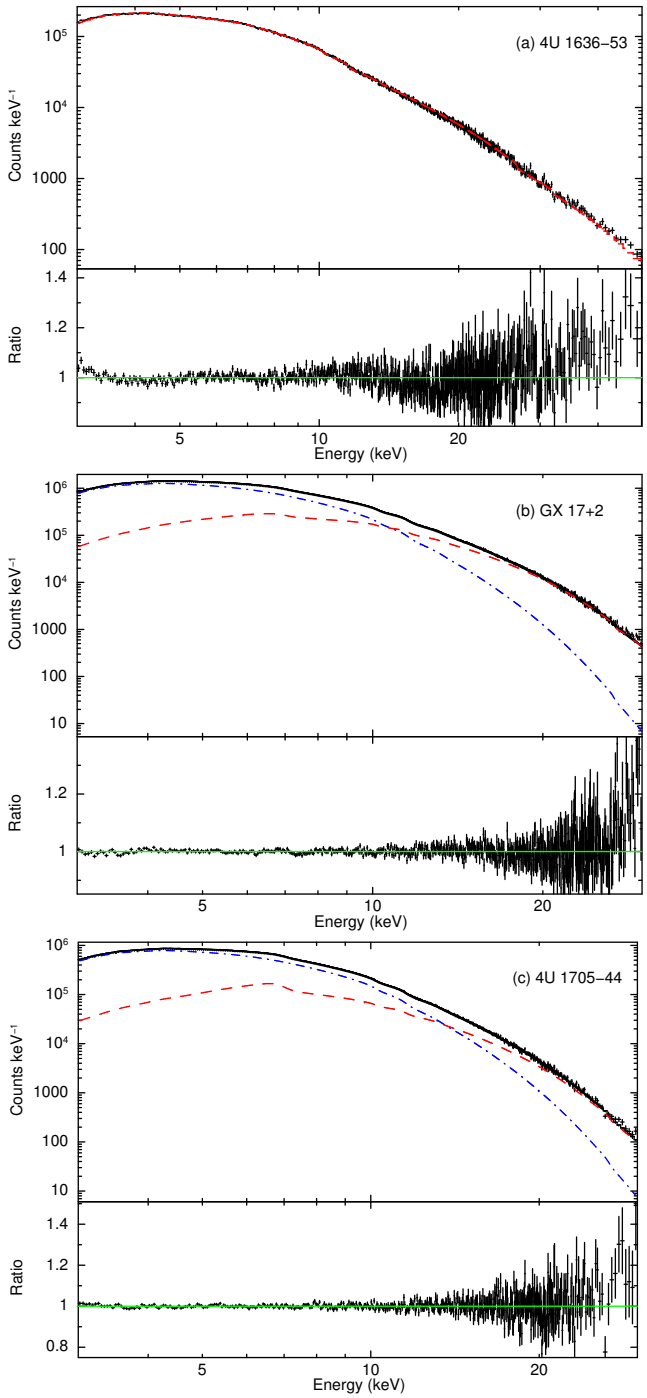

Figure 3.2 (a) 4U 1636-53 spectrum fit from 3.0-50.0 keV with RELXILL (red dash line) for the fit in Table 3.2. The panel below shows the ratio of the data to the model. (b) GX 17+2 spectrum fit from 3.0-30.0 keV with DISKBB (blue dot-dash line) and BBREFL (red dash line) for the fit in Table 3.4. The panel below shows the ratio of the data to the model. (c) 4U 1705-44 spectrum fit from 3.0-30.0 keV with DISKBB (blue dot-dash line) and BBREFL (red dash line) for the fit in Table 3.5. The panel below shows the ratio of the data to the model. The data were rebinned for plotting purposes.

power law and can be seen in Table 3.2. The ionization parameter is reasonable for accreting sources across all fits. The iron abundance is large, but fixing it to lower values does not change the inner disk radius. Regardless of the iron abundance, each fit consistently gives a small inner disk radius of $R_{in} = 1.03 \pm 0.03$ ISCO for $a_* = 0.0$ and $R_{in} = 1.08 \pm 0.06$ ISCO for $a_* = 0.3$. The fit returns a high inclination of $76.5° - 79.9°$ for each spin value. The photon index is 1.74 ± 0.01 with a cut off energy at ~ 20.5 keV. The best fit spectrum can be seen in Figure 3.2. Figure 3.3 shows the goodness-of-fit versus the inner disk radius (top panel).

To check that the values obtained with our RELXILL modeling of 4U 1636-53 are not model dependent, we apply the model REFLIONX to characterize the emergent reflection spectrum arising from an incident cut-off power law continuum. We blur the emergent reflection with the relativistic convolution model KERRCONV. This version of REFLIONX has an adjustable cut-off energy which we tie with the cut-off power law model used to model the continuum emission. This model, however, is angle averaged, unlike RELXILL, which properly takes into account the inclination of the disk when tracing each photon from the disk.

The resulting fit can be seen in Table 3.3 for a spin of 0.0 and 0.3. The inner disk radius is consistent with the values found in the RELXILL modeling. Additionally, the photon index, high energy cut-off, emissivity index, spin parameter, ionization, and inclination are within error for the values found with RELXILL. This demonstrates that the inner disk radius measurement is robust.

3.5.2 GX 17+2

Initial fits were performed from 3.0-30.0 keV with an absorbed single temperature blackbody and a multi-temperature blackbody component. This gives a poor fit ($\chi^2/dof = 4289.59/670$) because the reflection spectrum is not yet modeled. The Fe K_α emission can be seen in the middle panel in Figure 3.1. The red wing extends

down to ~ 4 keV while the blue wing drops around ~ 7 keV.

We use BBREFL to model the emergent reflection emission and convolve it with RELCONV. The overall model we used was TBABS*(DISKBB+RELCONV*BBREFL). This model provides a better fit with $\chi^2/dof = 793.2/665$ (33σ improvement for the highest χ^2_ν). Parameters and values can be seen in Table 3.4. Figure 3.2 shows the best fit spectrum. For $a_* = 0.0$, the inner disk radius is tightly constrained to $R_{in} = 1.00 - 1.02$ ISCO for $A_{Fe} = 1.0$ and $R_{in} = 1.00 - 1.04$ ISCO for $A_{Fe} = 2.0$. For the higher value of spin, $a_* = 0.3$, $R_{in} = 1.15^{+0.15}_{-0.08}$ ISCO for $A_{Fe} = 1.0$ and $R_{in} = 1.10 \pm 0.07$ ISCO for $A_{Fe} = 2.0$. The emissivity index is high in each case (ray tracing assuming either a hot spot at a modest latitude, or a heated equatorial region, both predict $q = 3.0$; D. Wilkins, priv. comm.). The inclination lies between $25^\circ - 38^\circ$ for all fits. Figure 3.3 shows the change in goodness-of-fit versus the inner disk radius (middle panel).

To test the origin of the Fe K_α line, we use a version of REFLIONX that assumes a blackbody is illuminating the accretion disk. Table 3.4 shows parameters and values using this model. The overall fit is worse, but still requires a small inner disk radius of $R_{in} = 1.00 - 1.02$ ISCO for both values of spin. The inclination and ionization is consistent with the values found in the previous fits with BBREFL. The emissivity index is close to simple expectations. Regardless, the small inner radii measured with REFLIONX imply that dynamical broadening is dominant in shaping the iron line, and any atmospheric effects are secondary.

Table 3.4 GX 17+2 Reflection Modeling

Component	Parameter	BBREFL				REFLIONX	
TBABS	$N_H(10^{22})^\dagger$	0.9	0.9	0.9	0.9	0.9	0.9
DISKBB	T_{in}	1.93 ± 0.04	1.992 ± 0.001	1.93 ± 0.05	1.92 ± 0.06	1.92 ± 0.01	1.92 ± 0.01
	$norm$	26 ± 1	23.8 ± 0.1	26 ± 2	26 ± 2	26.8 ± 0.4	26.7 ± 0.4
BLACKBODY	kT	...	...	...	...	2.86 ± 0.01	2.86 ± 0.01
	norm (10^{-2})	...	...	...	...	2.9 ± 0.1	2.9 ± 0.1
RELCONV	q	$8.1^{+0.8}_{-1.0}$	$3.7^{+4.7}_{-0.3}$	6.0 ± 3.0	4.5 ± 1.5	3.5 ± 0.1	3.2 ± 0.1
	$a_*^\dagger$	0.0	0.3	0.0	0.3	0.0	0.3
	$i(^\circ)$	$35.1^{+0.2}_{-0.6}$	30^{+8}_{-2}	30 ± 5	30 ± 4	25.9 ± 0.2	25.8 ± 0.2
	$R_{in}(ISCO)$	$1.00^{+0.02}$	$1.15^{+0.15}_{-0.08}$	1.02 ± 0.02	1.10 ± 0.07	1.01 ± 0.01	1.01 ± 0.01
	$R_{out}(R_g)^\dagger$	990	990	990	990	990	990
	$R_{in}(km)$	$12.0^{+0.2}$	$11.5^{+1.5}_{-0.8}$	12.2 ± 0.2	11.0 ± 0.7	12.1 ± 0.1	10.1 ± 0.1
BBREFL	$log(\xi)$	$2.47^{+0.07}_{-0.01}$	2.45 ± 0.01	$2.33^{+0.09}_{-0.01}$	2.40 ± 0.06	...	...
	kT (keV)	$3.15^{+0.01}_{-0.07}$	$3.12^{+0.04}_{-0.01}$	$3.03^{+0.05}_{-0.01}$	3.03 ± 0.02	...	...
	$A_{Fe}^\dagger$	1.0	1.0	2.0	2.0	...	...
	f_{refl}	$1.69^{+0.04}_{-0.67}$	$1.52^{+0.67}_{-0.01}$	$1.2^{+0.2}_{-0.4}$	$1.27^{+0.04}_{-0.50}$	...	...
	$z^\dagger$	0	0	0	0	...	...
	norm (10^{-26})	$8.83^{+0.60}_{-0.01}$	$8.61^{+0.02}_{-0.36}$	$13.0^{+1.0}_{-0.03}$	$13.1^{+0.08}_{-0.01}$	...	...
REFLIONX	ξ	...	...	...	...	240 ± 20	230 ± 7
	A_{Fe}	...	...	...	...	2.1 ± 0.4	2.1 ± 0.4
	f_{refl}	...	...	...	...	0.9 ± 0.1	0.9 ± 0.1
	$z^\dagger$	...	...	...	...	0	0
	norm	...	...	...	...	1.7 ± 0.2	1.8 ± 0.1
	$F_{\rm unabs,3.0-30.0keV}$	$7.3^{+0.6}_{-0.3}$	$7.30^{+0.04}_{-0.31}$	$7.3^{+0.8}_{-0.6}$	7.3 ± 0.1	7.3 ± 0.9	7.3 ± 0.5
	$L_{\rm unabs,3.0-30.0keV}$	1.5 ± 0.1	$1.48^{+0.01}_{-0.06}$	$1.5^{+0.2}_{-0.1}$	1.48 ± 0.02	1.5 ± 0.2	1.5 ± 0.1
	$F_{\rm unabs,0.5-30.0keV}$	$10.7^{+0.8}_{-0.4}$	$10.7^{+0.1}_{-0.4}$	$10.7^{+1.2}_{-0.8}$	10.7 ± 0.8	11.0 ± 1.3	11.0 ± 0.7
	$L_{\rm unabs,0.5-30.0keV}$	$2.2^{+0.2}_{-0.1}$	$2.16^{+0.01}_{-0.08}$	2.2 ± 0.2	2.2 ± 0.2	2.2 ± 0.3	2.2 ± 0.1
	χ^2_ν(dof)	1.06 (665)	1.13 (665)	1.19 (665)	1.18 (665)	1.28 (664)	1.26 (664)

† = fixed

Note.— Errors are quoted at 1σ confidence level. The absorption column density was fixed to the Dickey & Lockman (1990) value and given in units of cm^{-2}. Limb brightening was assumed. The emissivity index was pegged at the hard limit of 3.0. The REFLIONX model used has been modified for a blackbody illuminating the accretion disk. The inclination for REFLIONX was pegged within the limits found with the BBREFL due to the model being angle averaged and not able to constrain the inclination. The ionization parameter was also pegged within the BBREFL values since it was unconstrained on its own. The blackbody temperature in REFLIONX was tied to the temperature of the blackbody used to model the continuum emission. The emissivity index was pegged at the hard limit of 3.0. The inner disk radius in units of km assumes a NS mass of 1.4 $M_\odot$. Flux is given in units of 10^{-9} ergs cm^{-2} s^{-1}. Luminosity is calculated at a maximum of 13.0 kpc and given in units of 10^{38} ergs s^{-1}.

Table 3.5 4U 1705-44 Reflection Modeling

Component	Parameter	BBREFL				REFLIONX	
TBABS	$N_H(10^{22})^\dagger$	0.7	0.7	0.7	0.7	0.7	0.7
DISKBB	T_{in}	2.13 ± 0.01	2.13 ± 0.01	2.00 ± 0.01	2.00 ± 0.01	1.95 ± 0.02	1.95 ± 0.03
	$norm$	9.65 ± 0.02	9.6 ± 0.1	11.48 ± 0.02	11.60 ± 0.01	12.3 ± 0.5	12.4 ± 0.6
BLACKBODY	kT	...	...	...	...	2.54 ± 0.02	2.54 ± 0.03
	norm (10^{-2})	...	...	...	...	1.15 ± 0.05	1.15 ± 0.08
RELCONV	q	3.1 ± 0.1	3.1 ± 0.1	3.2 ± 0.1	3.2 ± 0.1	2.8 ± 0.3	2.7 ± 0.3
	$a_*^\dagger$	0.0	0.3	0.0	0.3	0.0	0.3
	$i(^\circ)$	24.4 ± 0.4	24.4 ± 0.4	24.6 ± 0.5	25.6 ± 0.5	13 ± 11	16 ± 6
	$R_{in}(ISCO)$	1.54 ± 0.08	1.82 ± 0.09	1.50 ± 0.07	1.78 ± 0.09	1.21 ± 0.18	1.37 ± 0.27
	$R_{out}(R_g)^\dagger$	990	990	990	990	990	990
	$R_{in}(km)$	18.4 ± 1.0	18.2 ± 0.9	18.0 ± 0.8	17.8 ± 0.9	14.5 ± 2.2	13.7 ± 2.7
BBREFL	$log(\xi)$	2.67 ± 0.02	2.66 ± 0.02	2.74 ± 0.04	2.74 ± 0.04	...	...
	kT (keV)	2.83 ± 0.01	2.84 ± 0.02	2.67 ± 0.01	2.67 ± 0.01	...	...
	$A_{Fe}^\dagger$	1.0	1.0	2.0	2.0	...	...
	f_{refl}	2.0 ± 0.1	2.1 ± 0.2	0.74 ± 0.02	0.74 ± 0.02	...	...
	$z^\dagger$	0	0	0	0	...	...
	norm (10^{-26})	1.24 ± 0.06	1.24 ± 0.08	2.1 ± 0.2	2.1 ± 0.2	...	...
REFLIONX	ξ	...	...	...	...	430 ± 20	430 ± 20
	A_{Fe}	...	...	...	...	2.0 ± 0.4	2.0 ± 0.6
	f_{refl}	...	...	...	...	0.72 ± 0.06	0.72 ± 0.08
	$z^\dagger$	...	...	...	...	0	0
	norm	...	...	...	...	0.57 ± 0.04	0.60 ± 0.05
	$F_{\rm unabs,3.0-30.0keV}$	3.4 ± 0.2	3.4 ± 0.2	3.4 ± 0.3	3.4 ± 0.3	3.4 ± 0.3	3.4 ± 0.4
	$L_{\rm unabs,3.0-30.0keV}$	2.5 ± 0.1	2.5 ± 0.2	2.5 ± 0.2	2.5 ± 0.2	2.5 ± 0.2	2.5 ± 0.3
	$F_{\rm unabs,0.5-30.0keV}$	5.0 ± 0.2	5.0 ± 0.3	5.0 ± 0.5	5.0 ± 0.5	5.2 ± 0.5	5.2 ± 0.6
	$L_{\rm unabs,0.5-30.0keV}$	3.7 ± 0.2	3.7 ± 0.2	3.7 ± 0.3	3.7 ± 0.3	3.8 ± 0.3	3.8 ± 0.5
	χ^2_ν(dof)	1.16 (665)	1.16 (665)	1.19 (665)	1.19 (665)	1.21 (664)	1.21 (664)

† = fixed

Note.— Errors are quoted at 1σ confidence level. The absorption column density was fixed to the Dickey & Lockman (1990) value and given in units of cm^{-2}. Limb brightening was assumed. The REFLIONX model used has been modified for a blackbody illuminating the accretion disk. The inclination for REFLIONX was pegged within the limits found with the BBREFL due to the model being angle averaged and not able to constrain the inclination. The ionization parameter was also pegged within the BBREFL values since it was unconstrained on its own. The blackbody temperature in REFLIONX was tied to the temperature of the blackbody used to model the continuum emission. Inner disk radius in units of km assumes a NS mass of 1.4 $M_\odot$. Flux is given in units of 10^{-9} ergs cm^{-2} s^{-1}. Luminosity is calculated at a maximum of 7.8 kpc and given in units of 10^{37} ergs s^{-1}.

3.5.3 4U 1705-44

Initial fits were performed from 3.0-30.0 keV with an absorbed single temperature blackbody and a multi-temperature blackbody component. This gives a poor fit ($\chi^2/dof = 4504.9/670$) since the strong disk reflection spectrum has not been modeled. See the bottom panel of Figure 3.1 for the Fe K_α line.

We use BBREFL to model the emergent reflection emission and convolve it with RELCONV (Dauser et al., 2010). The overall model we used was TBABS*(DISKBB+ RELCONV*BBREFL). This provides a better overall fit (34σ improvement for the highest χ^2_ν). Parameters and values can be seen in Table 3.5. The inner disk radius is slightly truncated prior to the neutron star surface between 1.46-1.64 ISCO for $a_* = 0.0$ for both values of iron abundance. For $a_* = 0.3$, the inner disk radius is truncated at 1.69-1.93 ISCO. The inclination is between $24.0° - 26.1°$ for all fits. The change in goodness-of-fit versus the inner disk radius can be seen in the bottom panel of Figure 3.3.

Again, we test the origin of our Fe K_α line in this truncated disk with the version REFLIONX that has been modified for a blackbody illuminating the disk. The resulting fits can be seen in Table 3.5. Even though the overall fit is slightly worse, the disk still requires a truncation of $R_{in} = 1.21 \pm 0.18$ ISCO for $a_* = 0.0$ and $R_{in} = 1.37 \pm 0.27$ ISCO for $a_* = 0.3$. Neither model strongly requires that the disk extends to the ISCO, though the ISCO is within 2 sigma of the nominal best-fit values found with REFLIONX. This confirms that dynamical broadening is the dominant mechanism for the iron line shape.

Since the disk does not extend down to the ISCO, we calculate the extent of a possible boundary layer and place an upper limit on the magnetic field strength since these are plausible scenarios for disk truncation. Popham & Sunyaev (2001) lay out the Newtonian framework for boundary layer behavior for different mass accretion rates. We estimate the mass accretion for 4U 1705-44 to be $(3.4 \pm 0.4) \times 10^{-9}$ $M_\odot$

yr^{-1} from the 0.5-30.0 keV unabsorbed luminosity and using an efficiency of $\eta = 0.2$ (Sibgatullin & Sunyaev, 2000). Using Equation (25) in Popham & Sunyaev (2001), we estimate that the boundary layer extends out to ~ 1.2 ISCO (assuming 1.4 $\mathrm{M}_{\odot}$ & $a_* = 0.0$). Additional factors, such as spin and viscosity in the layer, can extend this region to be consistent with the truncation of the inner disk.

If the disk is impeded by the magnetosphere, we can place an upper limit on the strength of the field using the upper limit of $R_{in} = 9.8$ R_g. Assuming a mass of 1.4 $\mathrm{M}_{\odot}$, taking the distance to be 7.8 kpc, and using the unabsorbed flux from 0.5-30.0 keV of 5.2×10^{-9} erg cm^{-2} s^{-1} as the bolometric flux, we can determine the magnetic dipole moment, μ, from Equation (1) taken from Cackett et al. (2009). If we make the same assumptions about geometry (i.e. $k_A = 1$, $f_{ang} = 1$) and use an accretion efficiency of $\eta = 0.2$, then $\mu \simeq 2.2 \times 10^{26}$ G cm^3. This corresponds to a magnetic field strength of $B \simeq 4.3 \times 10^8$ G at the magnetic poles for a NS of 10 km. Moreover, if we assume a different conversion factor $k_A = 0.5$ (Long et al., 2005) then the magnetic field strength at the poles would be $B \simeq 1.5 \times 10^9$ G. Note that the magnetic field strength at the pole is twice as strong as at the equator. However, the type 1 X-ray burst that occurred during the observation mean material is still reaching the surface of the NS and no pulsations have been seen.

3.6 Discussion

Using *NuSTAR*, we have taken a hard look at three well-known neutron star X-ray binaries. Our observations captured 4U 1636−53 in the hard state, while GX 17+2 and 4U 1705−44 were caught in soft states. Owing to *NuSTAR*'s broad bandpass and its ability to measure robust spectra at high flux levels, we are able to constrain different properties of these sources through modeling of reflection from their disks. Different disk reflection spectra are considered for each source in order to examine how inferred radii depend on modeling assumptions. For plausible combinations of neutron

star masses and dimensionless angular momenta, our results imply that disks extend to an ISCO, that neutron stars are smaller than their ISCO, and the results begin to place meaningful constraints on neutron star radii. In this section, we consider the results within the context of the neutron star equation of state, implications for the inner accretion flow onto neutron stars, and evaluate possible systematic errors and avenues for improvement in future studies.

3.6.1 Neutron Star Radius Constraints

4U 1636-53 is found to have an inner disk radius of 1.00-1.03 ISCO for $a_* = 0.0$ and 1.02-1.14 ISCO for $a_* = 0.3$ as constrained from RELXILL modeling of the reflection spectrum. We applied another reflection model, REFLIONX, to test the robustness of our measurement. The resulting fit gave a nearly identical inner disk measurement. For $a_* = 0.3$ and 1.4 $M_\odot$, 1.08 ± 0.06 ISCO translates to 10.8 ± 0.6 km. For the lower value of $a_* = 0.0$ and 1.4 $M_\odot$, 1.03 ± 0.03 ISCO translates to 12.4 ± 0.4 km. This small inner disk radius is in agreement with previous measurements for this source that were consistent with the ISCO (Pandel et al. 2008; Cackett et al. 2010; Sanna et al. 2013). The high inclination of 4U 1636-53 is consistent with previous reflection studies (Frank et al. 1987; Casares et al. 2006; Cackett et al. 2010; Sanna et al. 2013).

Similarly, the inner disk radius in GX 17+2 is tightly constrained to 1.00-1.02 ISCO for $a_* = 0.0$ and 1.03-1.30 ISCO for $a_* = 0.3$ by using the blackbody reflection model BBREFL. We found a tighter constraint on the inner disk radius of 1.00-1.01 ISCO when we applied a REFLIONX model that was modified for a blackbody illuminating the disk. For $a_* = 0.0$ and 1.4 $M_\odot$, $1.00 - 1.02$ ISCO translates to $12.0 - 12.2$ km. For the higher value of $a_* = 0.3$ and 1.4 $M_\odot$, $1.03 - 1.30$ ISCO translates to $10.3 - 13$ km. The inclination was found to be $25° - 38°$. Cackett et al. (2010) found similarly small inner disk radii and low inclination for this system.

Thus, in the most sensitive and robust spectra of 4U 1636−53 and GX 17+2 yet

obtained, the innermost extent of the accretion disk is found to be close to the ISCO, with consequences for the neutron star radii. There may still be a boundary layer present on the surface of the NS, but in this case it would have to be quite small. Given that 1 ISCO corresponds to 12 km, for $a_* = 0$ and 1.4 $M_\odot$, and using the fiducial neutron star radius of 10 km, the boundary layer would be about $\sim$2 km. The inner disk radii are not strongly dependent upon the reflection models that are utilized. We therefore proceed to examine the implications of the results for the EOS of ultradense matter in a more generalized way. Rather than assuming specific values $a = cJ/GM^2$, we need to determine the likely range of a given the measured spin frequencies for these sources.

4U 1636-53 and GX 17+2 have known rotation frequencies: $\nu_{1636-53} = 581.0$ Hz (Galloway et al., 2008) and $\nu_{17+2} = 293.2$ Hz (Wijnands et al., 1997), respectively. The total angular momentum, J, can be obtained from the spin frequency assuming a reasonable range of mass and radius for a neutron star and a solid sphere ($J = \frac{2}{5}MR^2\omega$ where $\omega = 2\pi\nu_{spin}$). For 4U 1636$-$53, $\nu = 581$ Hz then implies $0.10\pm0.08 < a_{1636-53} < 0.45 \pm 0.25$, and $\nu = 293.2$ Hz implies $0.05 \pm 0.04 < a_{17+2} < 0.23 \pm 0.12$. These values assume a mass range of $1.3 \leq M_{\rm NS}/M_\odot \leq 2.1$, consistent with the range of masses that have been measured directly (Jacoby et al. 2005; Demorest et al. 2010; Freire et al. 2011; Kiziltan et al. 2013). The lower limit of the radius range was determined by where causality approximately intersects the largest measure NS. The upper limit of the radius range was limited by break up ($a_* = 0.7$).

The radius of the ISCO around a compact object in units of gravitational radii is depends on its spin Bardeen et al. (1972); the ranges above therefore enable a translation to gravitational radii and then into kilometers. Figure 3.4 plots these ranges in the mass versus radius plane used to characterize the EOS. Several equations of states from Akmal et al. (1998), Lattimer & Prakash (2001), and Horowitz & Piekarewicz (2001) are also plotted, as well as known NS masses from pulsar timing

methods and binaries. The regions allowed by our models must be considered upper limits on the radius of neutron stars, since the neutron star can be smaller than its ISCO. Disk reflection is not yet able to rule out plausible EOS; however, deeper X-ray spectra and/or mass measurements in these systems can greatly reduce the allowed regions in this mass–radius plane.

3.6.2 Implications of Disk Truncation in 4U 1705−44

In 4U 1636−53 and GX 17+2, the inner disk appears to extend to the ISCO, and we cannot place any constraints on the magnetic field in these sources. In contrast, 4U 1705-44 has an inner disk radius of 1.46-1.64 ISCO for $a_* = 0.0$ and $1.69 - 1.93$ ISCO for $a_* = 0.3$. For a spin of 0.0 and stellar mass of 1.4 $M_\odot$, 1.46-1.64 ISCO translates into 17.5-19.7 km. A spin of 0.3 and stellar mass of 1.4 $M_\odot$, 1.69-1.93 ISCO translates into 16.9-19.3 km.

The similarity between the results of our fits and prior work suggests that such modeling is converging on a relatively consistent set of physical constraints. A truncated disk has been indicated in 4U 1705−44 in several prior investigations (Di Salvo et al. 2009, 2015; Reis et al. 2009b; Egron et al. 2013; Cackett et al. 2010, 2012). Our results closely match those of Reis et al. (2009b); that work reported the disk of 4U 1705−44 was truncated above the stellar surface with a gap of ∼3.5 km. Our models find that the inclination of the inner disk is between $24.0° - 26.1°$; this is again largely consistent with previous reflection studies ($20° - 50°$, Piraino et al. 2007; $\leq 35°$, Reis et al. 2009b; D'Aì et al. 2010; Cackett et al. 2010, 2012; Egron et al. 2013). Di Salvo et al. (2015) find a slightly larger inclination than we do of $43° \pm 5°$.

Disks around neutron stars can be truncated by a boundary layer, or by magnetic pressure. It is also possible that the inner disk may evaporate at low accretion rates, qualitatively similar to the expected truncation of disks around black holes at low mass accretion rates. Evidence of this may be seen in HETE J1900.1-2455 (Papitto

et al., 2013).

In Section 3.3, we estimated that the boundary layer could push out to 1.2 ISCO based on the arguments in Popham & Sunyaev (2001). This is smaller than the radius implied by most of our disk reflection models, but the predicted extent of the boundary layer can be increased for specific combinations of radiative efficiency and stellar spin. D'Aì et al. (2010) estimated that the boundary layer in 4U 1705−44 extended out to $\sim 2\ R_{\rm NS}$ in the soft state. Our estimate is consistent with this picture assuming a NS radius of 10 km.

If the neutron star magnetosphere is truncating the disk, we place an upper limit on the magnetic field strength at the poles to be $B \leq 0.4 - 1.5 \times 10^9$ (see Section 3.3). A recent study by King et al. (2016) also found a truncated disk surrounding the well-known neutron star X-ray binary and pulsar Aql X-1. An inner disk radius of $R_{in} = 15 \pm 3\ R_g = 2.88 \pm 0.58$ ISCO was measured via disk reflection. If the disk was not truncated by a boundary layer and instead by the neutron star magnetic field, an upper limit of $B < 5 \pm 2 \times 10^8$ G results (King et al., 2016). Aql X-1 had a Type 1 X-ray burst during the observation, suggesting that some material was still reaching the surface, like 4U 1705−44.

3.6.3 Inner accretion flows and $\dot{M}$

It is expected that the inner radius of an accretion disk is partly set by the mass accretion rate through the disk (see, e.g., González Martínez-País et al. 2014). Indeed, as noted above, several mechanisms might truncate the inner accretion disk around a neutron star, but each truncation mechanism becomes more effective at lower mass accretion rates. Indeed, the radial extent of the inner disk may be an important factor in determining the phenomena manifested in different parts of the "Z" and "atoll" tracks followed by many persistent neutron star X-ray binaries, and even the position of the source along such tracks.

The sensitive spectra that we have obtained with *NuSTAR* have permitted particularly strong radius constraints. Prior *NuSTAR* observations of neutron stars have also measured inner disk radii. It is now pragmatic to consider what a modest collection of robust spectral constraints implies about the evolution of the inner accretion disk around neutron stars as a function of the mass accretion rate. For consistency, we carefully replicated the models considered in prior work within XSPEC, and extrapolated the models to a common energy range (0.5–50 keV). We then use the maximum distance to each source to convert unabsorbed fluxes to luminosities, and divided by an Eddington limit of 3.8×10^{38} ergs s^{-1} as per Kuulkers et al. (2003) to obtain the Eddington fraction.

Table 3.7 lists the key data that result from this exercise. Figure 3.5 plots the inner disk radius versus Eddington fraction for a set of eight neutron stars observed with *NuSTAR*. Across almost two orders of magnitude in Eddington fraction – implying an equivalent range in mass accretion rate if the efficiency is independent – the inner disk appears to remain very close to the ISCO. The most obvious exception to the overall trend is Aql X-1; however, this source is known to be a pulsar and it may have a slightly higher magnetic field than other sources in the sample.

Cackett et al. (2010) found similar results when looking at the inner disk radius dependence on Eddington fraction for a sample of 10 neutron stars that were observed with *XMM-Newton* and *Suzaku*. Chiang et al. (2016b) recently looked at *Suzaku* observations of Ser X-1 over a range of flux states and found that the inner disk radius changes little between $0.2 - 0.6\ L_{\rm Edd}$. Disk reflection studies undertaken with *NuSTAR* have the advantages of a broad, continuous bandpass that enables better characterization of the direct continuum and stronger constraints on the total reflection spectrum, and spectroscopy that is not distorted by photon pile-up (which can falsely skew the shape of the line: Ng et al. 2010; Miller et al. 2010).

3.6.4 Potential systematic errors and modeling issues

We have obtained spectra with very high statistical quality, and therefore spectral fitting results with small statistical errors. Systematic errors are likely to be comparable or larger, and should be considered. In practice, the most important sources of systematic errors are difficult to quantify, but they are important to mention.

All measures of black hole spin that utilize the accretion disk, and all limits on neutron star radii that utilize the disk (including disk reflection and QPOs), assume that gas in the disk orbits as test particles would orbit. If real fluid disks push slightly inward of the ISCO defined for test particles, it amounts to a systematic error on such measurements. There is no astrophysical test of this assumption, but numerical simulations can potentially provide some insights. Explorations of disks around black holes suggest that accretion disks do generally obey the test particle ISCO (Reynolds & Fabian, 2008). Similar simulations have not been performed in the presence of a neutron star, and the influence of a boundary layer may also induce small changes. New simulations can help to address such systematics.

Apart from the reaction of the accretion disk to the potential, it is possible that our assumption of a Kerr metric is itself a source of systematic error. The neutron star that we have studied may have a small quadrupole moments, and this could change the effective potential in which the disk orbits. One treatment suggests that systematic errors related to quadrupole-induced deviations from a pure Kerr metric are $\leq$10% even for a dimensionless spin parameter of $a = 0.3$ (Sibgatullin & Sunyaev, 1998).

The blurred reflection models themselves can potentially be sources of systematic error. Some ancillary parameters of the reflection models require a note of caution. We now turn to these issues.

For 4U 1636−53, both RELXILL and RELCONV×REFLIONX return small and formally consistent inner disk radii. Different runs with RELCONV×BBREFL and REL-

CONV ×REFLIONX all return small radii consistent with $R_{in} \leq 1.1$ ISCO in fits to GX 17+2. In some cases, the errors are formally different at the 1σ level of confidence, but the values are consistent over more conservative ranges. In these two cases, the models are in close agreement and suggest that the radius values that emerge can be taken seriously. For 4U 1705−44, a greater range of inner disk radii emerges with different models and parameter selections. The most recent model, REFLIONX, returns radii that are nearly consistent with the ISCO at 1σ; other models return values as large as $R_{in} = 1.8$ ISCO, and the majority of models – and the best overall fits – measure a truncated disk. Deeper observations of 4U 1705−44 may be required to obtain a more definitive picture of that source.

The emissivity profile of the accretion disk encodes the geometry of the emitting source and space time of the innermost environment. An emissivity index of $q = 3$ is expected for a point source emitter in a (nearly) Schwarzschild spacetime, and different plausible geometries for neutron stars (boundary layers, hot spots) appear to produce the same emissivity profile (D. Wilkins, priv. comm.). Both families of reflection models prefer a flatter emissivity in fits to the spectrum of 4U 1636−53. This may be the result of a more extended corona in the hard state. Fits to the spectrum of GX 17+2 with BBREFL generally prefer a much steeper index, but fits with the more recent REFLIONX model are only slightly steeper than $q = 3$. This is broadly consistent with the direct continuum, which suggests that a boundary layer or hot spot is likely irradiating the disk. The models for 4U 1705−44 are all broadly consistent with $q = 3$.

The abundance of iron affects the local *strength* of reflection relative to the direct continuum, not the shape of the line. It is the *shape* of the disk reflection spectrum – and particularly the shape of the Fe K emission line – that is used to infer the inner radius of the accretion disk, and to thereby set an upper limit on the radius of the neutron star. The abundance of iron does not directly affect our radius measurements.

However, it is interesting to consider this parameter and whether or not it is accurately determined. Both families of reflection models prefer an iron overabundance of 4.5–5.0 relative to solar values, in fits to 4U 1636−53. It is unlikely that the abundance of iron is that high in the low mass companion star in 4U 1636−53, but it is possible that this measurement correctly describes the atmosphere of the accretion disk. There, the ionization structure may skew the relative abundances of different elements to values that do not reflect the overall abundances within the accretion flow. Fits to the spectra of GX 17+2 and 4U 1705−44 are consistent with iron abundances of 1.0–2.0 times solar values, but these fits also return lower ionization parameters, potentially consistent with ionization affecting abundance measurements. It is also possible that the enhanced abundances may the result of effects in especially dense gas. In these cases, the abundance would increase to replicate the continuum for a lower density disk allowed by the atomic data set within the current reflection models (García et al., 2016).

Finally, we simply note that the ionization parameters measured in different fits to each source spectrum are comparable to the values seen for other NS reflection studies, $2.3 < log(\xi) < 4.0$ (Cackett et al. 2010; Miller et al. 2013; Degenaar et al. 2015).

3.7 Conclusions

We have measured the inner disk radius for three different NSs that were observed with *NuSTAR*. 4U 1636-53 and GX 17+2 have a small inner disk radius that is constrained to the ISCO. This value has proven to be model independent for 4U 1636-53 and suggest that the NS is smaller than their ISCO. Converting ISCO to km for a range of spin parameters and NS masses provides a range in which allowed theoretical EOSs must lie. 4U 1705-44 possesses a truncated disk which we used to explore the possibility of a magnetic field or a boundary layer. We estimate the upper

Table 3.6 NS Inner Disk Radii & Eddington Fraction Observed with *NuSTAR*

Source	R_{in} (ISCO)	$F_{\rm Edd}$	ref.
Ser X-1	1.03-1.20	0.34	1
4U 1705-44	1.46-1.93	0.10	
4U 1636-53	1.00-1.14	0.01	
GX 17+2	1.00-1.30	0.57	
RXS J1804	1.00-1.85	0.02	2
	1.0-1.5	0.10	3
Aql X-1	2.31-3.46	0.13	4
4U 1608-52	1.3-2.0	0.03	5
4U 1728-34	1.0-2.0	0.04	6

Note.— (1) Miller et al. 2013; (2) Ludlam et al. 2016; (3) Degenaar et al. 2016; (4) King et al. 2016; (5) Degenaar et al. 2015; (6) Sleator et al. 2016.

limit of the magnetic field surrounding the NS to be $B \leq 0.4-1.5\times10^9$ G at the poles and depends on assumed conversion factor between disk and spherical accretion. We estimate the extent of a possible boundary layer out to ~ 1.2 ISCO.

Disk reflection has proven a valuable tool in determining properties of NSs, such as limits on the extent of the NS radius, boundary layer, and magnetic field strength. It provides another method to narrowing down the elusive EOS of ultradense, cold matter that makes up the NS. The advantage of this method being that the distance to the source is not needed and short observations can provide a clear look at Fe K_α emission. Furthermore, complementary mass estimates can yield further constraints to the EOS.

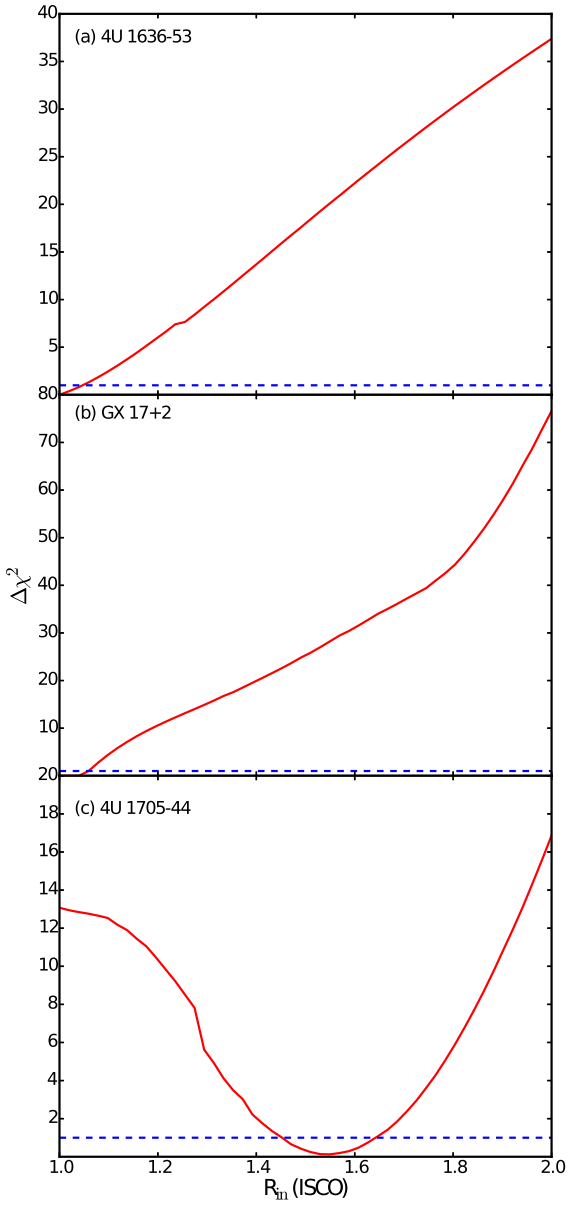

Figure 3.3 The change in goodness-of-fit versus inner disk radius for the *NuSTAR* observations of 4U 1636-53, GX 17+2, and 4U 1705-44 taken over 50 evenly spaced steps generated with XSPEC "steppar". The inner disk radius was held constant at each step while the other parameters were free to adjust. The blue dashed line shows the 68% confidence level. (a) 4U 1636-53 fit corresponding to the first column in Table 3.2. (b) GX 17+2 fit corresponding to the fifth column in Table 3.4. (c) 4U 1705-44 fit corresponding to the first column in Table 3.5.

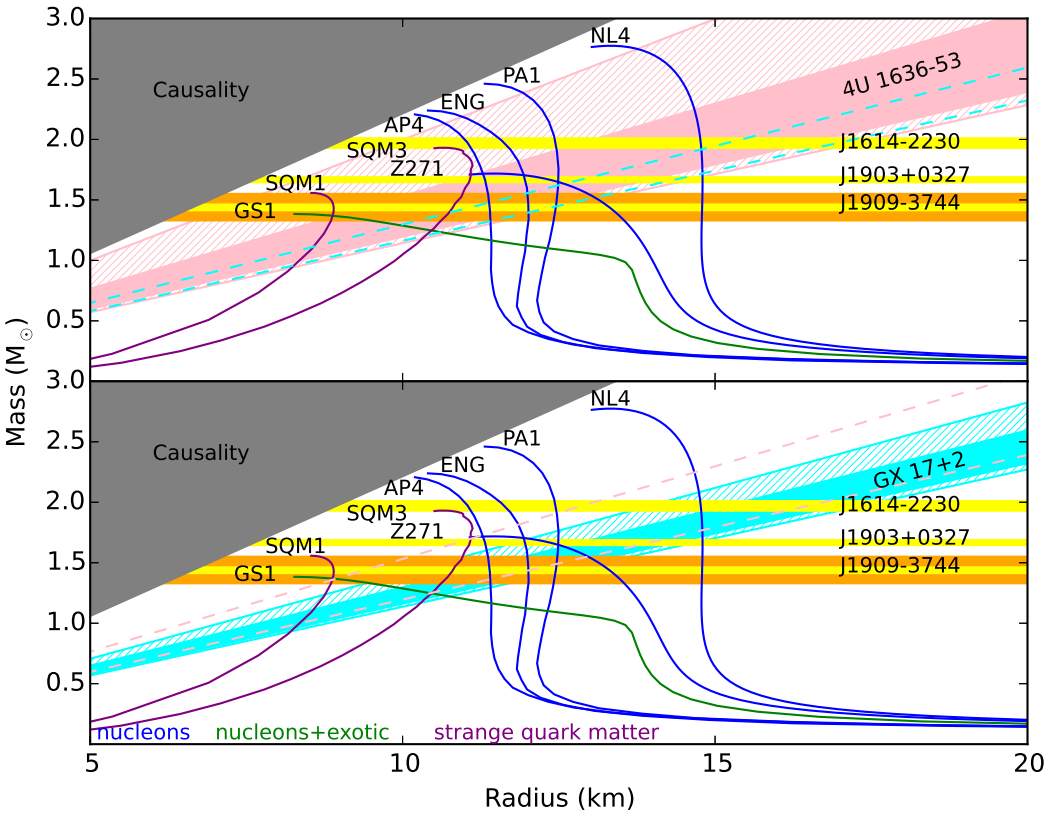

Figure 3.4 Constraints on the cold, ultradense matter equation of state from Fe K_α reflection modeling to determine the inner disk radius, assuming that the stellar surface is truncating the disk. The gray region is excluded by causality (the speed of sound must be less than the speed of light). The curve labeled NL4 is from Akmal et al. (1998) and Z271 is from Horowitz & Piekarewicz (2001). All other mass-radius curves are labeled as in Lattimer & Prakash (2001). The shaded regions for 4U 1636-53 and GX 17+2 correspond to the allowed values for mass and radius given a spin frequency of 581.0 Hz (Galloway et al., 2008) and 293.2 Hz (Wijnands et al., 1997), respectively. For reasonable values for mass and radius, a spin frequency of 581.0 Hz relates to a spin parameter of $0.10 \pm 0.08 < a_* < 0.45 \pm 0.25$ and 293.2 Hz gives $0.05 \pm 0.04 < a_* < 0.23 \pm 0.12$. The hatched area represents the errors on the spin parameter. The dashed lines in each panel represent the solid area constraints from the NS in the other panel. The yellow horizontal lines are the measured masses for the NSs PSR J1614-2230 ($M = 1.97 \pm 0.04\ M_\odot$; Demorest et al. 2010), PSR 1903+0327 ($M = 1.667 \pm 0.021\ M_\odot$; Freire et al. 2011) and PSR J1909-3744 ($M = 1.438 \pm 0.024\ M_\odot$; Jacoby et al. 2005). The orange region represents mass range found for a NS in a double NS system ($M = 1.33 - 1.55\ M_\odot$; see Kiziltan et al. 2013 for a review).

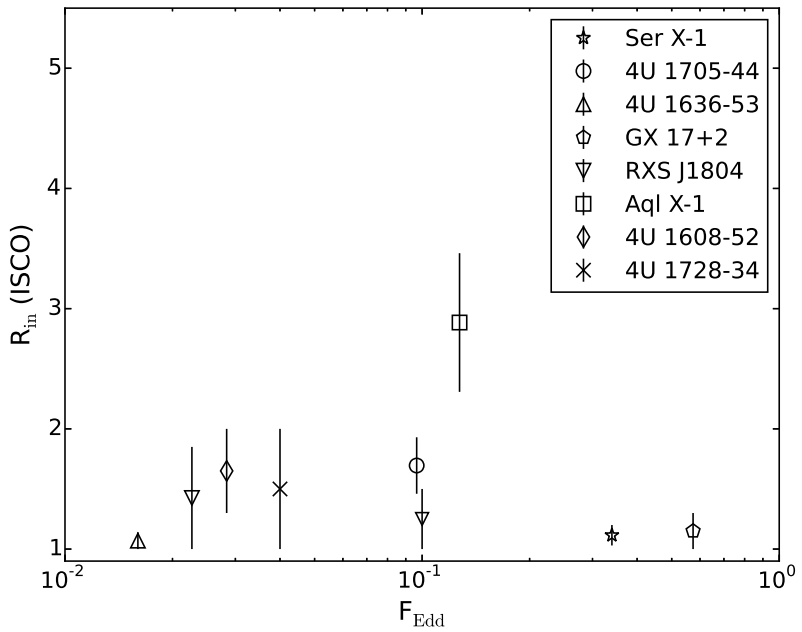

Figure 3.5 Comparison of Eddington fraction and measured inner disk radii for NSs observed with *NuSTAR*. Inner disk radius and Eddington fractions for 4U 1608-52, Ser X-1, Aql X-1, and 4U 1728-34 are obtained from Degenaar et al. (2015), Miller et al. (2013), King et al. (2016), and Sleator et al. (2016), respectively. Values for RXS J1804 are taken from Ludlam et al. (2016) and Degenaar et al. (2016). See Table 3.7 for inner disk radii and Eddington fractions.

CHAPTER IV

Relativistic Disk Reflection in the Neutron Star X-ray Binary XTE J1709-267 with *NuSTAR*

4.1 Preface

This chapter appears in the Astrophysical Journal, Volume 838, page 79 (Ludlam et al., 2017b) and is co-authored by Jon M. Miller, Edward M. Cackett, Nathalie Degenaar, and Allison C. Bostrom. The paper is reproduced here under the non-exclusive rights of republication granted by the American Astronomical Society to the authors of the paper.

4.2 Abstract

We perform the *first* reflection study of the soft X-ray transient and Type 1 burst source XTE J1709-267 using *NuSTAR* observations during its 2016 June outburst. There was an increase in flux near the end of the observations, which corresponds to an increase from $\sim$0.04 L_{Edd} to $\sim$0.06 L_{Edd} assuming a distance of 8.5 kpc. We have separately examined spectra from the low and high flux intervals. Both spectra were soft and show evidence of a broad Fe K line, consistent with relativistically blurred reflection from the inner accretion disk. Fits to these intervals with relativistic disk reflection models have revealed some properties of the inner accretion flow onto the

neutron star. We find the disk to be truncated $2.3^{+0.5}_{-0.3}$ ISCO (innermost stable circular orbit) for the low flux spectrum and $4.0^{+1.8}_{-0.9}$ ISCO for the high flux spectrum at the 90% confidence level. For a spin parameter of $a_* = 0$, where $a_* = cJ/GM^2$, this corresponds to $13.8^{+3.0}_{-1.8}$ R_g (where $R_g = GM/c^2$) for the lower flux and $24.0^{+10.8}_{-5.4}$ R_g for the higher spectrum. The disk is likely truncated by a boundary layer surrounding the neutron star or the magnetosphere. Based on the measured luminosity and using the accretion efficiency for a disk around a neutron star, we estimate that the theoretically expected size for the boundary layer would be $\sim 1.0 - 1.1$ R_g from the neutron star's surface. Although the size of this region could be increased by spin or viscosity, the boundary layer is not likely to extend out far enough to truncate the measured inner disk during the high flux interval. Another plausible scenario is that the disk could be truncated by the magnetosphere. We place a conservative upper limit on the strength of the magnetic field at the poles, assuming $a_* = 0$ and $M_{NS} = 1.4$ $M_\odot$, of $B \leq 0.75 - 2.70 \times 10^9$ G, though X-ray pulsations have not been detected from this source.

4.3 Introduction

XTE J1709-267 is a recurrent soft X-ray transient and Type 1 burst source that has a recurrence time of 2-3 years (Markwardt et al. 2004; Remillard et al. 2007; Negoro et al. 2010; Sanchez-Fernandez et al. 2012; Negoro et al. 2013). The source was first discovered to be in outburst in 1997 (Marshall et al., 1997) and is associated with the globular cluster NGC 6293 (Jonker et al., 2004b) that is located a distance of 8.5 kpc away (Lee & Carney, 2006). The typical 2-10 keV flux during outburst is $\sim 2 \times 10^{-9}$ ergs cm^{-2} s^{-1} (Marshall et al. 1997; Cocchi et al. 1998; Jonker et al. 2003, 2004a, 2004b; Markwardt et al. 2004; Remillard et al. 2007; Degenaar et al. 2013).

Broad iron line profiles have been seen in low-mass X-ray binaries (LMXBs) that contain a neutron star (NS) as the primary accreting compact object (e.g. Bhat-

tacharyya & Strohmayer 2007; Papitto et al. 2008; Cackett et al. 2008, 2009, 2010; Di Salvo et al. 2009; Egron et al. 2013; Miller et al. 2013). The effects of gravitational redshift and Doppler shift/boosting are imprinted on emission lines. These relativistic effects become stronger closer to the compact object (Fabian et al., 1989). Hence, the profile of the Fe K_α line gives a direct measure of the position of inner disk. Furthermore, since the disk must truncate at or before the surface of the star, the Fe K_α line can be used to set an upper limit for the radius of the NS (Cackett et al. 2008, 2010; Reis et al. 2009b; Miller et al. 2013; Degenaar et al. 2015).

Two likely scenarios for disk truncation above $\sim 1\%$ L_{Edd} are: (1) pressure balance between the accreting material and NS's magnetic field or (2) the boundary layer extending from the surface of the NS, impeding the disk. Thus, studies of disk reflection can also be used to set an upper limit on the magnetic field strength (Cackett et al. 2009; Papitto et al. 2009; Miller et al. 2011; Degenaar et al. 2014, 2016; King et al. 2016; Ludlam et al. 2016) or the extent of the boundary layer (Ibragimov & Poutanen 2009; King et al. 2016; Ludlam et al. 2016, Chiang et al. 2016b).

MAXI/GSC registered that XTE J1709-267 had renewed activity in 2016 May 31 (Nakahira et al., 2016). We obtained two $\sim$ 20 ks observations with *NuSTAR* (Harrison et al., 2013) during this outburst while the source was in the soft state. We detect a broad Fe K_α line that we model as relativistic reflection to determine the extent of the inner accretion disk and measure the inclination. There are no previous Fe K detections for this source, making this the first detailed reflection analysis.

4.4 Observations and Data Reduction

NuSTAR observations of XTE J1709-267 were taken on 2016 June 8 (Obsids 90201025002 and 90201025003). There are two detectors aboard *NuSTAR* that collect data: focal plane module A (FPMA) and focal plane module B (FPMB). Lightcurves and spectra were created using a $120''$ circular extraction region centered around the

source using the nuproducts tool from NUSTARDAS v1.5.1 with CALDB 20160421. A background was generated and subtracted using another region of the same dimension in a region away from the source. There were no Type 1 X-ray bursts present in the lightcurves, but there was an increase in count rate near the end of the second observation (see Figure 4.1). We create gti files in order to separate the observation by low and high count rate. Preliminary modeling of the spectra with a simple continuum multiplied by a cross normalization constant is performed to determine how well the detectors agree with one another. We fixed the constant to unity for the FPMA and allowed it to float for the FPMB. The floating constant was found to be within 0.95-1.05 in each case. We proceeded to combine the two source spectra, background spectra, and ancillary response matrices via ADDASCASPEC. We use ADDRMF to create a single redistribution matrix file. We then combined the two observations of the same count rate as per King et al. (2016) resulting in a total combined exposure time for the spectrum of $\sim$ 62 ks for the lower flux regime and $\sim$ 41 ks for the spectrum generated from the higher flux. We will refer to these spectrum as the low and high hereafter. The spectra were grouped using GRPPHA to have a minimum of 25 counts per bin.

4.5 Spectral Analysis and Results

We use XSPEC version 12.9.0 (Arnaud, 1996) in this work with all errors quoted at 90% confidence level. Errors were calculated from Monte Carlo Markov Chain (MCMC) of length 100,000. We perform fits over the 3.0-30.0 keV energy range. Above 30 keV, the spectra are background dominated. We account for the equivalent neutral hydrogen column density along the line of sight via TBNEWER[1]. We fix the absorption column to the Dickey & Lockman (1990) value of 0.237×10^{22} cm^{-2}

[1]Wilms, Juett, Schulz, Nowak, in prep, http://pulsar.sternwarte.uni-erlangen.de/wilms/research/tbabs/index.html

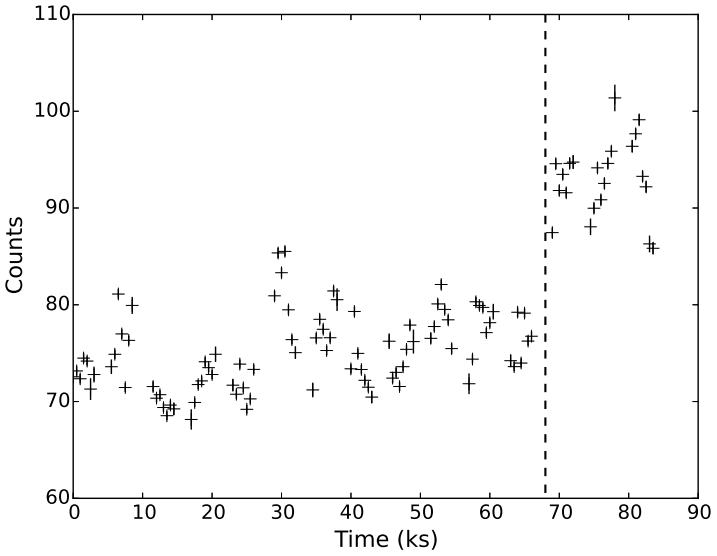

Figure 4.1 Lightcurve of the *NuSTAR* observation of J1709-267 using 500 s time bins. The vertical dashed line indicates the change in count rate in which we divided the observation.

(consistent with previous spectral studies of this source; e.g. Jonker et al. 2003, Degenaar et al. 2013), since *NuSTAR* lacks the lower energy bandpass to constrain this on its own.

Initial fits were performed with an absorbed single temperature blackbody component (BBODYRAD) to model the corona or boundary layer, and a multi-temperature blackbody (DISKBB) to account for the accretion disk emission. This combination of models gave a particularly poor fit in each case ($\chi^2_{\rm low}/dof$ = 1873.69/672 & $\chi^2_{\rm high}/dof$ = 1412.27/672), partly owing to the presence of strong disk reflection features in the spectrum. We added a power law component with the photon index bound at a hard limit of 4.0, which has been observed in astrophysical sources such as black hole X-ray novae (Sobczak et al. 2000; Park et al. 2004). The addition of power law component improved the overall fit for the low flux case by $\Delta\chi^2_{\rm low} = 350$ for 4 d.o.f. (11σ improvement) and is marginally significant (2σ improvement) in the high flux case. This continuum model is in agreement with the framework laid out in Lin et al. (2007) for NS transients in the soft state, though they use a broken

power law component instead. However, the reflection is still unaccounted for by this model. Figure 4.2 shows an asymmetric Fe K emission line, commonly associated with relativistic disk reflection. The red wing extends down to $\sim$ 5 keV while the blue wing drops around $\sim$ 7 keV.

The REFLIONX[2] (Ross & Fabian, 2005) model describes reflection from an ionized disk. We included a modified version that assumes the disk is illuminated by a blackbody, rather than a power law. To account for relativistic Doppler shifts and gravitational redshifts, we convolved REFLIONX with RELCONV (Dauser et al., 2010). The parameters of REFLIONX are as follows: ionization parameter (ξ), temperature of the incident blackbody in keV (kT), iron abundance (A_{Fe}), redshift (z), and normalization. The parameters of RELCONV are as follows: inner emissivity index (q_{in}), outer emissivity index (q_{out}), dimensionless spin parameter (a_*), inner disk radius in units of inner most stable circular orbit (ISCO; R_{in}), and outer disk radius in units of gravitational radii (R_{out}).

A few reasonable conditions were enforced when making fits with RELCONV and REFLIONX. First, we fixed the spin parameter, a_* (where $a_* = cJ/GM^2$), in the model RELCONV to 0 in the subsequent fits since NS in LMXBs have $a_* \leq 0.3$ (Miller et al. 2011; Galloway et al. 2008). Corrections for frame-dragging for $a_* < 0.3$ give errors $\ll 10\%$ (Miller et al., 1998) since the position of the ISCO is nearly constant for values of low spin. Therefore, this does not hinder our estimate of the inner disk radius. Further, the outer disk radius has been fixed to 400 R_g (where $R_g = GM/c^2$).

Last, we tied the outer emissivity index, q_{out} to the inner emissivity index, q_{in}, to create a constant emissivity index. We are unable to constrain the inner disk radius vs. inclination space when allowing the emissivity index to be a free parameter. We fix $q = 3$ as would be expected for a disk in flat, Euclidean geometry illuminated by a point source (see Wilkins & Fabian 2012 for review). Additionally, different plausible

[2]http://www-xray.ast.cam.ac.uk/$\sim$mlparker/reflionx_models/reflionx_bb.mod

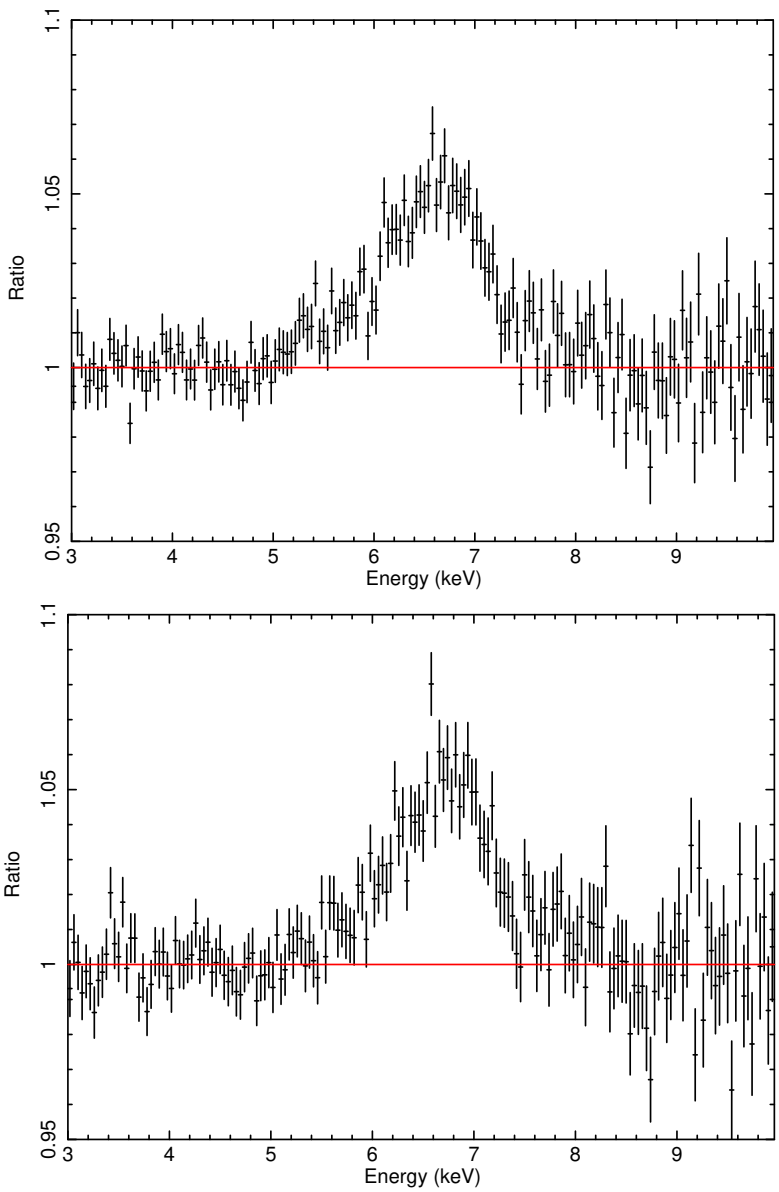

Figure 4.2 Ratio of the data to the continuum model for *NuSTAR* observation of XTE J1709-267 during the period of lower (top) and higher (bottom) flux. The iron line region from 5-8 keV was ignored to prevent the feature from skewing the fit. A simple disk blackbody, single temperature blackbody, and powerlaw were fit to model the continuum over the energies of 3.0-5.0 keV and 8.0-10.0 keV. Fitting up to 10 keV models both the continuum and some reflection continuum, but gives an unhindered view of the Fe K_α line.

geometries for illuminating the disk around neutron stars, such as boundary layers or hot spots, appear to produce the same r^{-3} emissivity profile (D. Wilkins, priv. comm.). A shallower profile like r^{-2} has been postulated based upon self-consistent MHD simulations for extended coronal emission surrounding a black hole (BH) and relies solely on mass, spin, and mass accretion rate (Kinch et al., 2016). However, the shallower profile may intimately depend on the specific set of parameters that were input into the simulation ($M_{BH} = 10\ M_{\odot}$, $a_* = 0$, and mass accretion rate at 1% of Eddington) and, thus, may not be directly translatable to NSs. Since the accretion disks surrounding NSs do not undergo extreme relativistic effects such as those around maximally spinning black holes, we do not expect steeper emissivity profiles.

The overall model we used for each spectrum was TBNEWER*(DISKBB+BBODY+POW +RELCONV*REFLIONX). This model provides a better fit with $\chi^2_{\rm low}/dof = 622.6/663$ and $\chi^2_{\rm high}/dof = 685.9/663$. This is a $>21\sigma$ improvement over the models that do not take into account disk reflection for each case. Parameters and values can be seen in Table 4.1. Figure 4.3 shows the best fit spectra.

For the low flux case, the DISKBB component has a temperature of $kT = 1.64^{+0.03}_{-0.04}$ keV and norm= 4.9 ± 0.4 km^2/100kpc^2. The BBODYRAD component has a temperature of $kT = 2.44^{+0.02}_{-0.03}$ keV and normalization of $0.36^{+0.07}_{-0.01}$ km^2/100kpc^2. The blackbody and disk blackbody normalizations are implausibly small but this is understood to be the result of spectral hardening in atmospheres above pure blackbody emission (London et al. 1986; Shimura & Takahara 1995; Merloni et al. 2000). The power law may or may not be physical but is still needed at the 8σ level. It has a steep photon index of $\Gamma = 3.99^{+0.01}_{-0.30}$ with a normalization of $0.32^{+0.05}_{-0.10}$. The inner disk radius is truncated at $R_{in} = 2.3^{+0.5}_{-0.3}$ ISCO and the inclination was found to be $25.2^{+2.6}_{-1.1}\ ^{\circ}$.

For the high flux case, the DISKBB component has a temperature of $kT = 1.67^{+0.03}_{-0.02}$

keV and norm= 10 ± 1 km^2/100kpc^2. The BBODYRAD component has a temperature of $kT = 2.40 \pm 0.02$ keV and normalization of $0.9^{+0.1}_{-0.2}$ km^2/100kpc^2. It has a steep photon index decreases to $\Gamma = 3.6 \pm 0.3$ with a normalization of $0.15^{+0.10}_{-0.08}$. The inner disk radius is truncated further out at $R_{in} = 4.0^{+1.8}_{-0.9}$ ISCO, though it is consistent with the value found in the low flux state at the 3σ level. The inclination is $26.4^{+3.5}_{-2.2}$ $^\circ$, which also agrees with what is found from the low flux spectrum.

We find the iron abundance to be $0.53 - 1.5$. The low abundance for this source is likely due to its association with a globular cluster which tends to host older populations of stars and therefore have a lower metallicity. Lee & Carney (2006) find the metallicity in NGC 6293 is $\sim 1/100$ of solar abundance. We were unable to explore a lower iron abundance due to the hard lower limit of the model ($A_{Fe} = 0.5$), however, anomalously high iron abundances have been seen in many reflection studies (e.g., Parker et al. 2015, 2016; Füerst et al. 2016; García et al. 2015; Walton et al. 2014, 2016). It is possible that this high A_{Fe} measurement correctly describes the atmosphere of the accretion disk and not the overall abundances within the accretion flow due to the ionization structure skewing the relative abundances there. Furthermore, the enhanced abundance may be the result of effects in especially dense gas, which would cause the abundance to increase to replicate the continuum for a lower density disk that is allowed by the atomic data set within current reflection models (García et al., 2016).

Figure 4.4 shows a contour plot for the inner disk radius versus the inclination for the fits in Table 4.1. The unabsorbed 0.5-50.0 keV flux changes from 2.0×10^{-9} ergs cm^{-2} s^{-1} to 2.7×10^{-9} ergs cm^{-2} s^{-1}. At a distance of 8.5 kpc, this gives a luminosity change of 1.7×10^{37} ergs s^{-1} to 2.3×10^{37} ergs s^{-1}. Or a change from 0.04 $L_{\rm Edd}$ to 0.06 $L_{\rm Edd}$ ($L_{\rm Edd} = 3.8 \times 10^{38}$ ergs s^{-1}; Kuulkers et al. 2003). We check that our results are not dependent on the our choice of $q = 3$ by fixing the index to $q = 2$ & $q = 2.5$ and find they are consistent with the inclination and R_{in} at the 3σ level in each case.

Table 4.1 J1709-267 Reflection Modeling

Component	Parameter	Low	High
TNEWER	$N_H(10^{22})^{\dagger}$	0.237	0.237
DISKBB	kT	$1.64^{+0.03}_{-0.04}$	$1.67^{+0.03}_{-0.02}$
	norm	4.9 ± 0.4	10 ± 1
BBODYRAD	kT	$2.44^{+0.02}_{-0.03}$	2.40 ± 0.02
	norm	$0.36^{+0.07}_{-0.01}$	$0.9^{+0.1}_{-0.2}$
POWER LAW	Γ	$3.99^{+0.01}_{-0.30}$	3.6 ± 0.3
	norm	$0.32^{+0.05}_{-0.10}$	$0.15^{+0.10}_{-0.08}$
RELCONV	$q^{\dagger}$	3.0	3.0
	$a_*^{\dagger}$	0	0
	$i(^{\circ})$	$25.2^{+2.6}_{-1.1}$	$26.4^{+3.5}_{-2.2}$
	$R_{in}(ISCO)$	$2.3^{+0.5}_{-0.3}$	$4.0^{+1.8}_{-0.9}$
	$R_{out}(R_g)^{\dagger}$	400	400
REFLIONX	ξ	200^{+80}_{-30}	130^{+20}_{-30}
	A_{Fe}	$0.57^{+0.22}_{-0.04}$	$0.9^{+0.6}_{-0.4}$
	$z^{\dagger}$	0	0
	norm	$0.19^{+0.02}_{-0.07}$	$0.59^{+0.26}_{-0.09}$
	$F_{\text{unabs, 0.5–50.0 } keV}$	$2.0^{+0.6}_{-1.0}$	$2.7^{+2.2}_{-1.6}$
	$L_{\text{unabs, 0.5–50.0 } keV}$	$1.7^{+0.5}_{-0.8}$	$2.3^{+1.9}_{-1.4}$
	χ^2(dof)	622.6 (663)	685.9 (663)

† = fixed

Note.— Errors are quoted at 90% confidence level. The absorption column density was fixed to the Dickey & Lockman (1990) value and given in units of cm^{-2}. The power law index was pegged at a hard limit of 4.0. The REFLIONX model used has been modified for a blackbody illuminating the accretion disk. The blackbody temperature was tied to the temperature of the blackbody used to model the continuum emission. The iron abundance, A_{Fe}, has a hard lower limit of 0.5. Flux is given in units of 10^{-9} ergs cm^{-2} s^{-1}. Luminosity is calculated at a distance of 8.5 kpc and given in units of 10^{37} ergs s^{-1}. For reference, 1 ISCO = 6 R_g for $a_* = 0$.

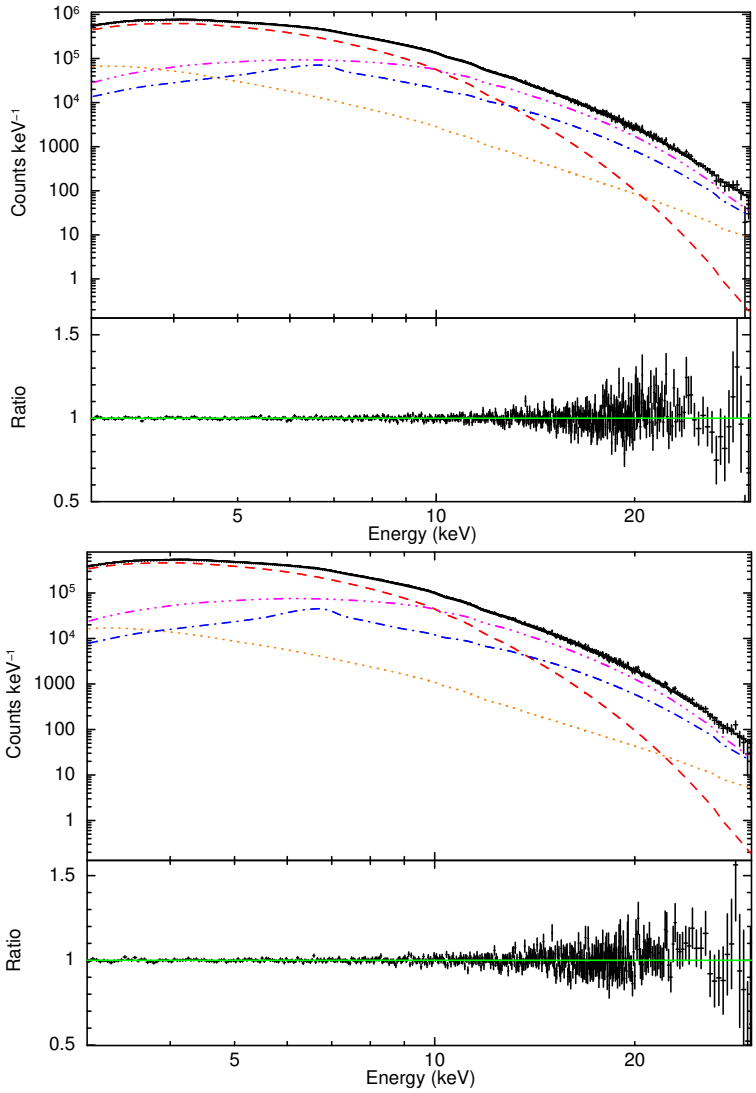

Figure 4.3 XTE J1709-267 low (top) and high (bottom) spectrum fit when from 3.0-30.0 keV with a DISKBB (red dash line), BLACKBODY (purple dot dot dot dash line), power law (orange dot line), and the modified version of REFLIONX (blue dot dash line) that assumes an input blackbody spectrum. The panel below shows the ratio of the data to the model. Table 4.1 lists parameter values. The data were rebinned for plotting purposes.

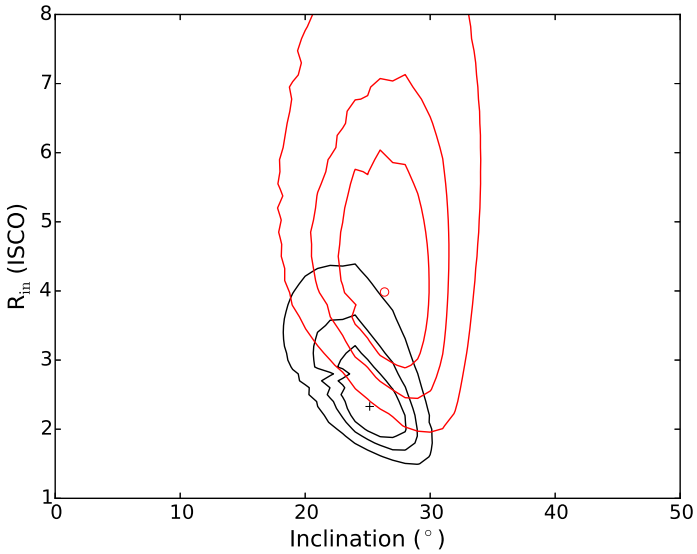

Figure 4.4 Contour plot for inner disk radius versus inclination at the 68%, 90%, and 99% confidence level for the low (black) and high (red) flux portion of the observations. The best fit values are denoted with a cross for the low flux and circle for the high flux.

4.6 Discussion

We have performed spectral analysis of the soft X-ray transient XTE J1709-267 during its 2016 outburst. This is the first report and analysis of a broad Fe-K$_\alpha$ line in this source. Our observations capture a change in flux emitted from the source which we separate into low and high flux spectra. We find the disk to be truncated between $2.3^{+0.5}_{-0.3}$ ISCO (90% confidence level) in the lower flux spectrum. This corresponds to $13.8^{+3.0}_{-1.8}$ R_g for $a_* = 0$. The disk appears to move outwards to $4.0^{+1.8}_{-0.9}$ ISCO ($24.0^{+10.8}_{-5.4}$ R_g) during the higher flux state, but is consistent with the low flux results at the 3σ level. The unabsorbed $0.5 - 50.0$ keV flux at the time of the observation started at 2.0×10^{-9} ergs cm^{-2} s^{-1} and increased to 2.7×10^{-9} ergs cm^{-2} s^{-1}, which is consistent with the typical flux observed during outburst (Marshall et al. 1997; Cocchi et al. 1998; Jonker et al. 2003, 2004a, 2004b; Markwardt et al. 2004; Remillard et al. 2007; Degenaar et al. 2013). Additionally, we find a low inclination of $24° - 30°$.

There are no previous estimates of the inclination for this system. The disk is likely truncated by a boundary layer surrounding the NS or the magnetosphere.

Popham & Sunyaev (2001) lay out the Newtonian framework for boundary layer behavior for different mass accretion rates. We estimate the mass accretion rate for XTE J1709-267 to be 1.5×10^{-9} $M_\odot$ yr^{-1} for the lower flux portion and 2.0×10^{-9} $M_\odot$ yr^{-1} for the higher flux from the 0.5-50.0 keV unabsorbed luminosity and using an efficiency of $\eta = 0.2$ (Sibgatullin & Sunyaev, 2000). Using Equation (25) in Popham & Sunyaev (2001), we estimate that the boundary layer extends from the surface of the NS out to $\sim 1.0 - 1.1$ R_g (assuming 1.4 $M_\odot$). Additional factors, such as spin and viscosity in the layer, can extend this region to be consistent with the inner edge of the accretion disk that we measured from our reflection analysis in the low flux, but would not be consistent with the larger inner disk radius from the high flux spectrum.

XTE J1709-267 was at a relatively low Eddington fraction ($\sim 0.04 - 0.06$) during the time of the observation. The truncation of the disk could be due to a pressure balance between the magnetic field and accretion in the disk. We can place an upper limit on the strength of the field using the upper limit of $R_{in} = 16.8$ R_g from the low flux spectrum. Assuming a mass of 1.4 $M_\odot$, taking the distance to be 8.5 kpc, and using the unabsorbed flux from 0.5-50.0 keV of 2.0×10^{-9} erg cm^{-2} s^{-1} as the bolometric flux, we can determine the magnetic dipole moment, μ, from Equation (1) taken from Cackett et al. (2009), which was adapted from Ibragimov & Poutanen (2009). If we assume an angular anisotropy, f_{ang}, and conversion factor, k_A, of unity, as well as an accretion efficiency of $\eta = 0.2$, then $\mu \simeq 3.7 \times 10^{26}$ G cm^3. This corresponds to a magnetic field strength of $B \simeq 7.5 \times 10^8$ G at the magnetic poles for a NS of 10 km. The magnetic field strength at the pole is twice as strong as at the equator. This is within the range for magnetic field strength for accreting millisecond pulsars ($10^7 - 10^9$ G; Mukherjee et al. 2015). The solution during the high flux gives a maximum magnetic field strength in excess of $B > 10^9$ G (2.7×10^9 G). However,

no X-ray pulsations have been detected from this source, so there are no indications that the magnetic field would be truncating the disk and channeling material to the magnetic poles.

Similar and recent analyses have been done for *NuSTAR* studies of the transient NS LMXBs 1RXS J180408.9-34205 (RXS J1804) and Aquila X-1 (Aql X-1). Ludlam et al. (2016) found that inner disk of RXS J1804 to be $R_{in} \leq 1.85$ ISCO in the hard state. They find that a magnetic field strength of $B \leq 0.3 - 1.0 \times 10^9$ G at the poles or a boundary layer that is roughly the stellar radius in size is needed to truncate the disk at 1.85 ISCO. Degenaar et al. (2016) found similar estimates of the magnetic field strength ($B \leq 2 \times 10^8$ G) and inner disk radius ($R_{in} \leq 1.5$ ISCO) while RXS J1804 was in the soft state. King et al. (2016) found a truncated disk at $R_{in} = 15 \pm 3$ $R_g = 2.88 \pm 0.58$ ISCO around Aql X-1. They estimate a boundary layer of $R_B = 7.8$ R_g (King et al., 2016) would be surrounding Aql X-1 given the efficiency and mass accretion rate. But if the disk was not truncated by a boundary layer and instead by the magnetosphere, they obtain an upper limit on the magnetic field of $B < 5 \pm 2 \times 10^8$ G (King et al., 2016). Both RXS J1804 and Aql X-1 had at least one Type 1 X-ray burst during their observation suggesting that material was still reaching the surface.

4.7 Summary

We perform the first reflection study for the soft X-ray transient XTE J1709-267 with observations from *NuSTAR* during its 2016 June outburst. Our observations catch the source during a change in luminosity from $0.04 - 0.06$ L_{Edd}. We find the disk is truncated prior to the NS surface at a distance of $2.3^{+0.5}_{-0.3}$ ISCO ($13.8^{+3.0}_{-1.8}$ R_g for $a_* = 0$) at 0.04 L_{Edd} and increases out to $4.0^{+1.8}_{-0.9}$ ISCO ($24.0^{+10.8}_{-5.4}$ R_g) at 0.06 L_{Edd}. The disk is likely truncated by a boundary layer surrounding the NS. We estimate that the boundary layer extends from the surface out to $\sim 1.0 - 1.1$ R_g for the mass

accretion rate and efficiency of the disk. However, though viscosity and spin effects can increase extent of the boundary layer, at low Eddington fraction the boundary layer is not likely to halt the accretion disk at a large radius (i.e., at the large radius implied by the high flux solution). An alternative explanation is that the disk is truncated by the magnetosphere. Conservative estimates place an upper limit on the magnetic field strength to be $B \leq 0.75 - 2.70 \times 10^9$ G at the magnetic poles, though XTE J1709-267 is not a known X-ray pulsar.

CHAPTER V

Truncation of the Accretion Disk at One-third of the Eddington Limit in the Neutron Star Low-mass X-Ray Binary Aquila X-1

5.1 Preface

This chapter appears in the Astrophysical Journal, Volume 847, page 135 (Ludlam et al., 2017c) and is co-authored by Jon M. Miller, Nathalie Degenaar, Andrea Sanna, Edward M. Cackett, Diego Altamirano, and Ashley L. King. The paper is reproduced here under the non-exclusive rights of republication granted by the American Astronomical Society to the authors of the paper.

5.2 Abstract

We perform a reflection study on a new observation of the neutron star low-mass X-ray binary Aquila X-1 taken with *NuSTAR* during the August 2016 outburst and compare with the July 2014 outburst. The source was captured at $\sim 32\%$ $L_{\rm Edd}$, which is over four times more luminous than the previous observation during the 2014 outburst. Both observations exhibit a broadened Fe line profile. Through reflection modeling, we determine that the inner disk is truncated $R_{in,\ 2016} = 11^{+2}_{-1}\ R_g$ (where

$R_g = GM/c^2$) and $R_{in,\ 2014} = 14 \pm 2\ R_g$ (errors quoted at the 90% confidence level). Fiducial neutron star parameters ($M_{NS} = 1.4\ M_\odot$, $R_{NS} = 10$ km) give a stellar radius of $R_{NS} = 4.85\ R_g$; our measurements rule out a disk extending to that radius at more than the 6σ level of confidence. We are able to place an upper limit on the magnetic field strength of $B \leq 3.0 - 4.5 \times 10^9$ G at the magnetic poles, assuming that the disk is truncated at the magnetospheric radius in each case. This is consistent with previous estimates of the magnetic field strength for Aquila X-1. However, if the magnetosphere is not responsible for truncating the disk prior to the neutron star surface, we estimate a boundary layer with a maximum extent of $R_{BL,\ 2016} \sim 10\ R_g$ and $R_{BL,\ 2014} \sim 6\ R_g$. Additionally, we compare the magnetic field strength inferred from the Fe line profile of Aquila X-1 and other neutron star low-mass X-ray binaries to known accreting millisecond X-ray pulsars.

5.3 Introduction

Aquila X-1 is a neutron star (NS) residing in a low-mass X-ray binary (LMXB) that has exhibited X-ray pulsations, if intermittently. A LMXB consists of an accreting compact object with a companion star of approximately solar mass. The companion star in Aquila X-1 is categorized as a K0 V spectral type (Thorstensen et al. 1978; Mata Sánchez et al. 2017). Coherent millisecond X-ray pulsations were detected for 150 s during persistent emission imply a spin frequency of 550 Hz (Casella et al., 2008). Type-I X-ray bursts place Aquila X-1 at a maximum distance of 5.9 kpc away, assuming the bursts are Eddington limited (Jonker et al., 2004b).

The inclination of the system is constrained to be $< 31°$ by infrared photometry measurements performed by Garcia et al. (1999). Intermittent dipping episodes may indicate an inclination as high as $72 - 79°$ (Galloway et al., 2016). However, intermittent dipping may not be indicative of a high inclination. Another low inclination system, 4U 1543-47, exhibited intermittent dipping that was suggestive of

an accretion instability (Park et al., 2004). Additionally, recent near-infrared spectroscopy rules out a high inclination and implies an inclination $23^\circ < i < 53^\circ$ when considering conservative constraints (Mata Sánchez et al., 2017). The magnetic field strength is estimated to be $0.4-31\times10^8$ G. This is inferred from pulsations signifying magnetically channeled accretion in *Rossi X-ray Timing Explorer* (*RXTE*) observations (Mukherjee et al., 2015). Additionally, the "propeller" phase, where material no longer accretes onto the NS but rather is thrown off from the disk at low luminosity, implies a similar magnetic field strength (Campana et al. 1998; Asai et al. 2013).

Broadened and skewed Fe line profiles have been detected from accretion disks in NS LMXBs for the last decade (e.g. Bhattacharyya & Strohmayer 2007; Papitto et al. 2008; Cackett et al. 2008, 2010; Di Salvo et al. 2009; Egron et al. 2013; Miller et al. 2013). These profiles are shaped from Doppler and relativistic effects (Fabian et al., 1989) and, as a consequence, the red wing can be used to determine the location of the inner edge of the disk.

The accretion disk must extend down to or truncate prior to the surface of the NS. Disk truncation can occur above $\sim 1\%$ L_{Edd} in one of two ways: either pressure balance between the accreting material and magnetosphere or a boundary layer of material extending from the surface. Below $\sim 1\%$ L_{Edd}, accretion in LMXBs can become inefficient and disk truncation can occur through other mechanisms, such as disk evaporation (Narayan & Yi 1995; Tomsick et al. 2009; Degenaar et al. 2017). By studying sources with truncated accretion disks at sufficiently high L_{Edd}, we can obtain estimates of magnetic field strengths (Ibragimov & Poutanen 2009; Cackett et al. 2009; Papitto et al. 2009; Miller et al. 2011; Degenaar et al. 2014, 2016; King et al. 2016; Ludlam et al. 2016) and/or extent of potential boundary layers (Popham & Sunyaev 2001; King et al. 2016; Ludlam et al. 2016, Chiang et al. 2016b).

It is not clear whether the magnetic field is dynamically important in Aquila X-1 and other non-pulsating NS LMXBs. Aquila X-1 is frequently active with outbursts

occurring about once a year (Campana et al. 2013; Waterhouse et al. 2016) making it a key target. King et al. (2016) obtained observations of Aquila X-1 in the soft state with *NuSTAR* and *Swift* during the July 2014 outburst. They found that the disk was truncated at $15 \pm 3\ R_g$ (where $R_g = GM/c^2$) at $\sim 7\%$ of the empirical Eddington luminosity ($L_{\rm Edd} = 3.8 \times 10^{38}$ ergs s^{-1}; Kuulkers et al. 2003). This placed a limit on the equatorial magnetic field strength of $B < 7 \times 10^8$ G that is consistent with previous estimates.

The *Swift*/BAT detected renewed activity on 2016 July 29 (Sanna et al., 2016a) that was confirmed to be a new outburst with a 500 s follow up *Swift*/XRT observation (Sanna et al., 2016b). Observations were taken with *NuSTAR* (Harrison et al., 2013) on 2016 August 7 when Aql X-1 was in the soft state at $\sim 0.32\ L_{\rm Edd}$ during the outburst. We perform a reflection study on the prominent Fe K_α feature for this observation and compare with the 2014 outburst.

5.4 Observations and Data Reduction

NuSTAR observations were taken of Aquila X-1 on 2014 July 17 and 18 (Obsids 80001034002 and 80001034003) and 2016 August 7 (Obsid 90202033002). Figure 5.1 shows the *Swift*/BAT and MAXI daily monitoring lightcurves with vertical dashed lines to indicate when the *NuSTAR* observations were taken. Lightcurves and spectra were created for the 2016 observations using a circular extraction region with a radius of 100″ centered around the source via the NUPRODUCTS tool from NUSTARDAS v1.5.1 with CALDB 20170503. A background was generated and subtracted using another region of the same dimension away from the source. There were no Type-I X-ray bursts present in the 2016 lightcurves. Initial modeling of the persistent emission spectra with a constant, fixed to 1 for the FPMA and allowed to float for the FPMB, found the floating constant to be within 0.95-1.05 in each case. We proceeded to combine the two source spectra, background spectra, and ancillary response matrices

via ADDASCASPEC. We use ADDRMF to create a single redistribution matrix file. Each of these have been weighted by exposure time. The 2014 observations were reduced using the most recent CALDB, 20170503, which has been updated since the reduction and analysis reported in King et al. (2016). The spectra were grouped using GRPPHA to have a minimum of 25 counts per bin (Cash, 1979). The net count rate for the combined spectra were 126.8 counts s^{-1} in 2014 and 424.3 counts s^{-1} in 2016.

We do not utilize the 2014 *Swift* observations as per King et al. (2016) due to major flux differences between the *NuSTAR* and *Swift* spectra. The *Swift* spectrum required a multiplicative constant of 3.75 to match the *NuSTAR* flux. This flux difference is likely due to the need to exclude the PSF core to avoid pile-up in the *Swift* data. Additionally, excluding the core of the PSF further limits the sensitivity of the *Swift* spectrum and, as a result, the reflection spectrum cannot be detected in the data. Furthermore, *Swift* only performed a short exposure observation (under 200 s) on the same day as the *NuSTAR* observation in 2016 that do not provide constraints. As a consequence, we opted to focus on the comparison of *NuSTAR* observations only in this study.

5.5 Spectral Analysis and Results

We utilize XSPEC version 12.9.1 (Arnaud, 1996) in this work with fits performed over the 3.0-30.0 keV energy range (the spectrum is dominated by background above 30 keV). All errors were calculated using a Monte Carlo Markov Chain (MCMC) of length 100,000 and are quoted at 90% confidence level. We use TBNEWER[1] to account for the absorption along the line of sight. Since *NuSTAR* lacks the lower energy bandpass to constrain the equivalent neutral hydrogen column density its own, we set it to the Dickey & Lockman (1990) value of 0.4×10^{22} cm^{-2}. Moreover,

[1]Wilms, Juett, Schulz, Nowak, in prep, http://pulsar.sternwarte.uni-erlangen.de/wilms/research/tbabs/index.html

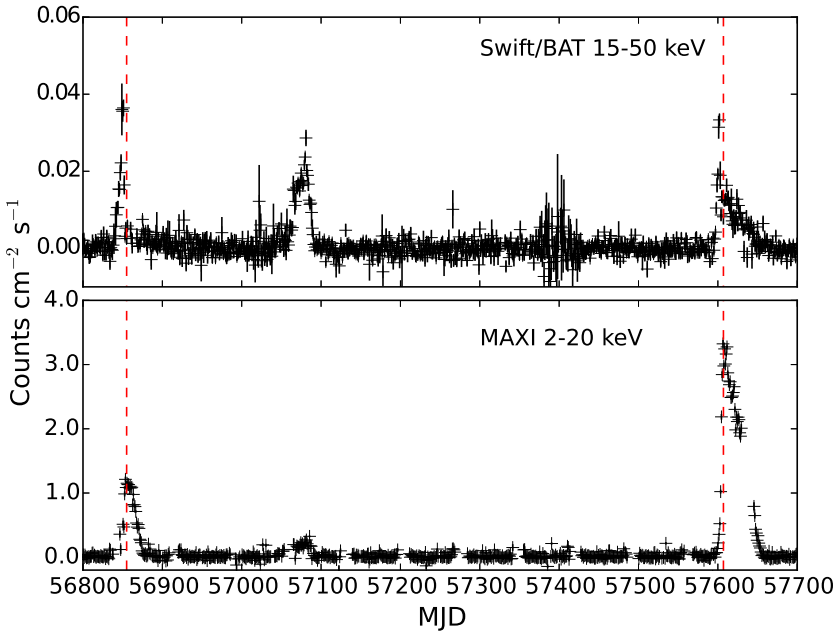

Figure 5.1 Swift/BAT $15-50$ keV and MAXI $2-20$ keV daily monitoring lightcurves. The dashed lines represent the *NuSTAR* observations taken in July 2014 and August 2016.

this value is very close to column densities found with low energy spectral fitting to *XMM-Newton* and *Chandra* data (Campana et al., 2014).

King et al. (2016) modeled the 2014 data using a Comptonized thermal continuum with a relativistically blurred emergent reflection emission. We chose to forego this combination of models in an effort to provide a self-consistent approach between components. The reflection model in King et al. (2016) assumes that a blackbody continuum is illuminating the disk, though the continuum is modeled with Comptonization. Further, the assumed blackbody in the reflection model that is providing the emergent reflection spectrum does not peak at the same energy as the Comptonized continuum. This means that the component assumed to illuminate the accretion disk is not consistent with the emergent reflection spectrum. We chose to adopt a continuum model akin to the framework laid out in Lin et al. (2007) for NS transients in the soft state. The continuum is described by two thermal components: a single

temperature blackbody component (BBODYRAD) to model the corona or boundary layer, and a multi-temperature blackbody (DISKBB) to account for the accretion disk emission. The addition of a power-law component may be needed in some cases and is suggestive of weak Comptonization.

Initial fits were performed with two thermal components. This combination of models gave a particularly poor fit in each case ($\chi^2_{2014}/d.o.f. = 4088.70/591$ and $\chi^2_{2016}/d.o.f. = 3946.47/585$), partly owing to the presence of strong disk reflection features in the spectrum. We added a power-law component with the photon index bound at a hard limit of 4.0, which have been observed in black hole X-ray binaries (Sobczak et al. 2000; Park et al. 2004). The addition of the power-law component improved the overall fit at more than the 9σ level of confidence, as determined via F-test, in each case. However, the reflection is still unaccounted for by this model. The broadened Fe K emission line can be seen in Figure 5.2 for each outburst.

We account for the emergent reflection from an ionized disk by convolving REFLIONX[2] (Ross & Fabian, 2005) with the relativistic blurring kernal RELCONV (Dauser et al., 2010). The REFLIONX model has been modified to assume the disk is illuminated by a blackbody, rather than a power-law. We tie the blackbody temperature of the reflection spectrum to the blackbody temperature of the illuminating continuum emission. We use a constant emissivity index, q, fixed at 3 as would be expected for a disk in flat, Euclidean geometry illuminated by a point source (see Wilkins & Fabian 2012 for review). Different plausible geometries for illuminating the disk around neutron stars, such as boundary layers or hot spots, appear to produce the same r^{-3} emissivity profile (D. Wilkins, priv. comm.). The iron abundance, A_{Fe}, is fixed at half solar abundance in agreement with the previous analysis on Aql X-1 (King et al., 2016). We fix the dimensionless spin parameter, a_* (where $a_* = cJ/GM^2$), to 0.259 which is implied from the pulsation spin frequency of 550 Hz (Braje et al. 2000;

[2]http://www-xray.ast.cam.ac.uk/∼mlparker/reflionx_models/reflionx_bb.mod

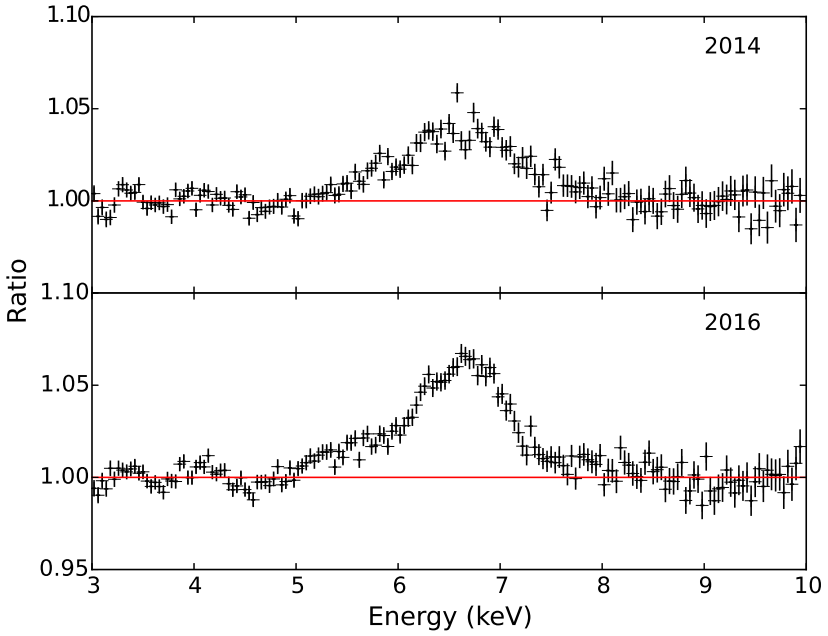

Figure 5.2 Comparison of Fe line profiles for Aql X-1 during the 2014 and 2016 outbursts created by taking the ratio of the data to the continuum model. The iron line region from 5-8 keV was ignored to prevent the feature from skewing the fit. A simple disk blackbody, single temperature blackbody, and power-law were fit to model the continuum over the energies of 3.0-5.0 keV and 8.0-10.0 keV. Fitting up to 10 keV models both the continuum and some reflection continuum, but gives an unhindered view of the Fe K_α line.

Casella et al. 2008; King et al. 2016). This assumes a NS mass of 1.4 $M_{\odot}$, radius of 10 km, and a moderately soft equation of state (Braje et al., 2000). The inner disk radius, R_{in}, is given in units of innermost stable circular orbit (ISCO). We convert this value to R_g given that 1 ISCO = 5.2 R_g for $a_* = 0.259$ (Bardeen et al., 1972).

The overall model we used for each spectrum was TBNEWER*(DISKBB+BBODYRAD +POW+RELCONV*REFLIONX). This provided an improvement in the overall fit at more than the 25σ level of confidence ($\chi^2_{2014}/d.o.f. = 620.29/583$ and $\chi^2_{2016}/d.o.f. = 603.08/579$) over the prior model that did not account for reflection within the spectra. Figure 5.3 shows the best fit spectra and model components. Model parameters and values are listed in Table 5.1. The power-law component may or may not be physical in origin but is statistically needed at more than the 15σ level of confidence for each spectrum.

For the data taken during the 2014 outburst, the DISKBB component has a temperature of $kT = 1.64 \pm 0.02$ keV and norm= $12.0^{+0.3}_{-0.5}$ km^2/100 kpc^2 cos(i). The BBODYRAD component has a temperature of $kT = 2.27 \pm 0.02$ keV and normalization of 1.2 ± 0.1 km^2/100 kpc^2. The power-law has a steep photon index of $\Gamma = 3.7 \pm 0.1$ with a normalization of 1.2 ± 0.1 photons keV^{-1} cm^{-2} s^{-1} at 1 keV. The inner disk radius is truncated at $R_{in} = 2.7 \pm 0.4$ ISCO (14 ± 2 R_g). The inclination was found to be 26^{+2}_{-3} °.

For the data taken during the 2016 outburst, the DISKBB component has a temperature of $kT = 1.69^{+0.01}_{-0.02}$ keV and norm= 62 ± 2 km^2/100 kpc^2 cos(i). The BBODYRAD component has a temperature of $kT = 2.33^{+0.01}_{-0.02}$ keV and normalization of $4.1^{+0.4}_{-0.2}$ km^2/100 kpc^2. It has a steep photon index of $\Gamma = 3.96^{+0.03}_{-0.21}$ with a normalization of $4.8^{+0.2}_{-0.9}$ photons keV^{-1} cm^{-2} s^{-1} at 1 keV. The inner disk radius is truncated at $R_{in} = 2.1^{+0.3}_{-0.2}$ ISCO (11^{+2}_{-1} R_g). The inclination is 26 ± 2 °, which also agrees with the previous observation.

The blackbody and disk blackbody normalizations in both fits are implausibly

Table 5.1 Aql X-1 Reflionx Modeling

Component	Parameter	2014	2016
TBNEWER	$N_H(10^{22})^{\dagger}$	0.4	0.4
DISKBB	kT	1.64 ± 0.02	$1.69^{+0.01}_{-0.02}$
	norm	$12.0^{+0.3}_{-0.5}$	62 ± 2
BBODYRAD	kT	2.27 ± 0.02	$2.33^{+0.01}_{-0.02}$
	norm	1.2 ± 0.1	$4.1^{+0.4}_{-0.2}$
POWERLAW	Γ	3.7 ± 0.1	$3.96^{+0.03}_{-0.21}$
	norm	1.2 ± 0.1	$4.8^{+0.2}_{-0.9}$
RELCONV	$q^{\dagger}$	3.0	3.0
	$a_*^{\dagger}$	0.259	0.259
	$i(^{\circ})$	26^{+2}_{-3}	26 ± 2
	$R_{in}(ISCO)$	2.7 ± 0.4	$2.1^{+0.3}_{-0.2}$
	$R_{in}(R_g)$	14 ± 2	11^{+2}_{-1}
	$R_{out}(R_g)^{\dagger}$	400	400
REFLIONX	ξ	400^{+60}_{-40}	200 ± 10
	$A_{Fe}^{\dagger}$	0.5	0.5
	$z^{\dagger}$	0	0
	norm	$0.25^{+0.02}_{-0.03}$	3.5 ± 0.2
	$F_{unabs,\ 0.5-50.0\ keV}$	6 ± 1	29^{+4}_{-6}
	$L_{0.5-50.0\ keV}$	2.5 ± 0.4	12^{+2}_{-3}
	$L_{0.5-50.0\ keV}/L_{\rm Edd}$	0.07 ± 0.01	$0.32^{+0.05}_{-0.08}$
	χ^2_{ν}(d.o.f.)	1.06 (583)	1.04 (579)

† = fixed

Note.— Errors are quoted at 90% confidence level. The absorption column density was fixed to the Dickey & Lockman (1990) value and given in units of cm^{-2}. The REFLIONX model used has been modified for a blackbody illuminating the accretion disk. The blackbody temperature was tied to the temperature of the blackbody used to model the continuum emission. The power-law index was pegged at a hard limit of 4.0. Flux is given in units of 10^{-9} ergs cm^{-2} s^{-1}. Luminosity is calculated at a maximum distance of 5.9 kpc and given in units of 10^{37} ergs s^{-1}. $L_{\rm Edd} = 3.8 \times 10^{38}$ ergs s^{-1} (Kuulkers et al., 2003). For reference, 1 ISCO = 5.2 R_g for $a_* = 0.259$.

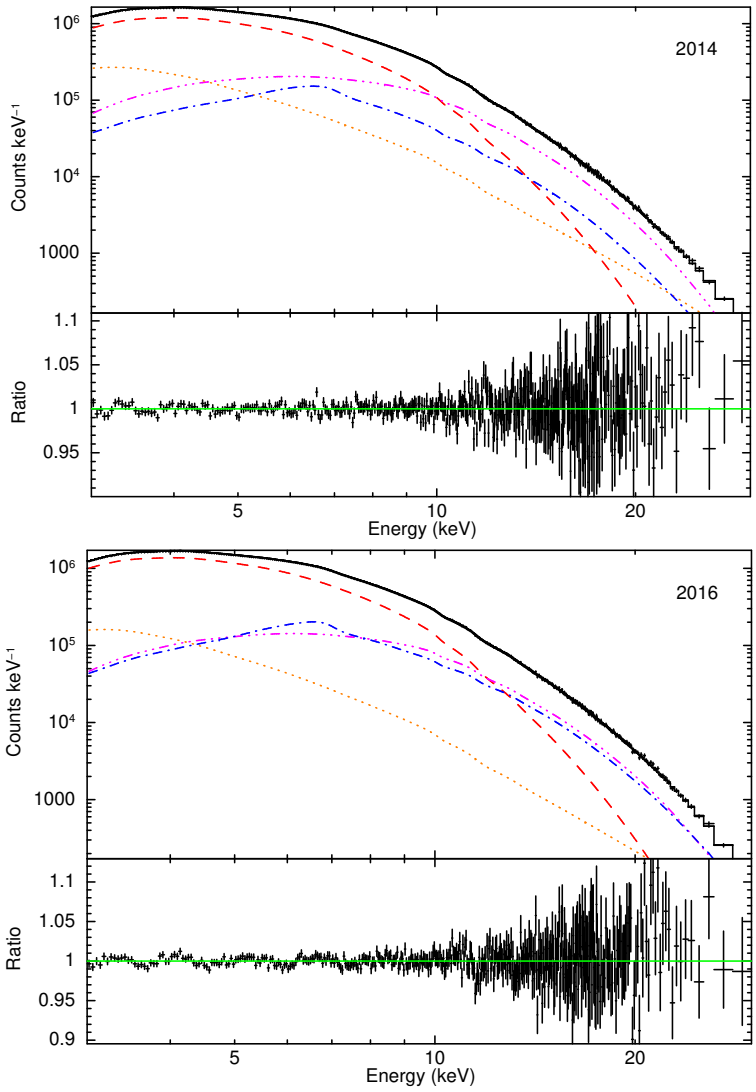

Figure 5.3 Aql X-1 spectrum fit from 3.0-30.0 keV with a DISKBB (red dash line), BLACKBODY (purple dot dot dot dash line), power-law (orange dot line), and REFLIONX (blue dot dash line). The panel below shows the ratio of the data to the model. Table 5.1 lists parameter values. The data were rebinned for plotting purposes.

small when used to infer a radial extent of the emitting region, but this is understood to be the result of spectral hardening in atmospheres above pure blackbody emission (London et al. 1986; Shimura & Takahara 1995; Merloni et al. 2000). The consistency in model parameter values with only the normalization changing between the two soft state observations likely indicates similar accretion geometries. We check that our results are not dependent upon the choice to fix $q = 3$ by allowing the emissivity to be a free parameter. The emissivity index tends towards a slightly higher value of $q = 3.1$ for the 2014 observation and $q = 2.5$, which is consistent with the disk extending down to a smaller radii in the most recent observation. All model parameters are consistent within the 3σ level of confidence with those reported in Table 5.1. Figure 5.4 shows how the goodness-of-fit changes with inner disk radius for each observation. We use the XSPEC "steppar" command to hold the inner disk radius constant over evenly placed steps while the other parameters were free to adjust. The ISCO is ruled out at more than the 6σ level of confidence in each case.

5.6 Discussion

We present a new observation of Aquila X-1 taken with *NuSTAR* during its August 2016 outburst and compare it to the July 2014 outburst. We perform reflection fits that indicate the disk is truncated prior to the surface of the neutron star. The location of the inner disk radius during the 2014 observation is $14 \pm 2\ R_g$. This is consistent with the previous results found in King et al. (2016), although we modeled the continuum in a different way. The location of the inner disk radius remains truncated ($11^{+2}_{-1}\ R_g$) during the 2016 observation even though the flux is over four times larger. Additionally, both spectra imply an inclination of $26 \pm 2^{\circ}$ which is consistent with infrared photometric and spectroscopic measurements (Garcia et al. 1999; Mata Sánchez et al. 2017).

We can place an upper limit on the strength of the magnetic field using the upper

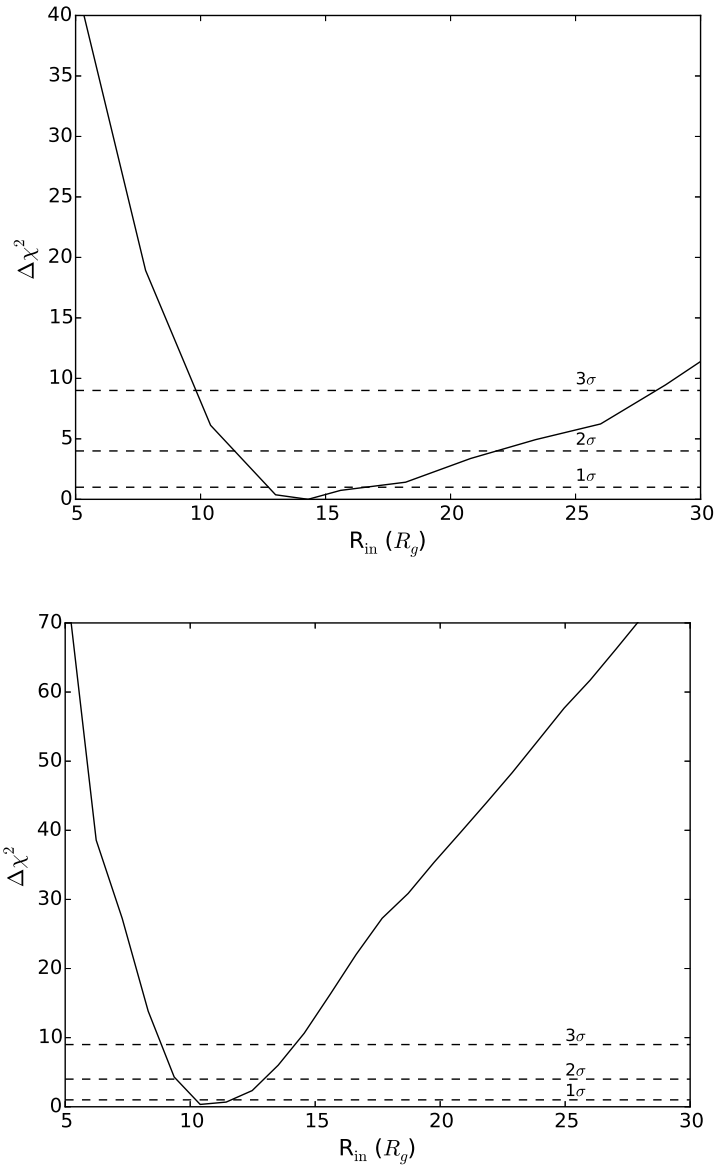

Figure 5.4 Change in goodness-of-fit with inner disk radius for the 2014 (top) and 2016 (bottom) outbursts taken over evenly spaced steps generated with XSPEC "steppar". The inner disk radius was held constant at each step while the other parameters were free to adjust. The dashed lines represent the 1σ, 2σ, and 3σ confidence intervals.

limit of $R_{in} = 13\ R_g$ from the 2016 spectrum. Assuming a mass of 1.4 $M_\odot$, taking the maximum distance to be 5.9 kpc, and using the maximum unabsorbed flux from $0.5 - 50.0$ keV of 33×10^{-9} erg cm^{-2} s^{-1} as the bolometric flux, we can determine the magnetic dipole moment, μ, from Equation (1) taken from Cackett et al. (2009), which was adapted from Ibragimov & Poutanen (2009).

$$\mu = 3.5 \times 10^{23}\ k_A^{-7/4}\ x^{7/4} \left(\frac{M}{1.4\ M_\odot}\right)^2 \times \left(\frac{f_{ang}}{\eta} \frac{F_{bol}}{10^{-9}\ \mathrm{erg\ cm^{-2}\ s^{-1}}}\right)^{1/2} \frac{D}{3.5\ \mathrm{kpc}}\ \mathrm{G\ cm^3} \tag{5.1}$$

with x being the number of gravitational radii. If we assume an angular anisotropy, f_{ang}, and conversion factor, k_A, of unity, as well as an accretion efficiency of $\eta = 0.2$, then $\mu \sim 6.7 \times 10^{26}$ G cm^3. This corresponds to a magnetic field strength of $B \leq 1.3 \times 10^9$ G at the magnetic poles for a NS of 10 km. Alternatively, if we assume a different conversion factor between disk and spherical accretion of $k_A = 0.5$ (Long et al., 2005), the strength of the magnetic field increases to $B \leq 4.5 \times 10^9$ G. For the 2014 outburst, we can place an upper limit on the magnetic field strength at $R_{in} = 16\ R_g$ and using the maximum unabsorbed flux from $0.5 - 50.0$ keV of 7×10^{-9} erg cm^{-2} s^{-1} to be $B \leq 0.9 \times 10^9$ G for $k_A = 1.0$ and $B \leq 3.0 \times 10^9$ for $k_A = 0.5$. Note that the magnetic field strength at the pole is twice as strong as at the equator. King et al. (2016) found a similar value for the maximum strength of the magnetic field for Aquila X-1 of $B \simeq 1.4 \times 10^9$ G at the magnetic poles. We report the upper limit on the magnetic field strength using the conversion factor of $k_A = 0.5$ hereafter since it encompasses the value for $k_A = 1.0$.

If, however, the magnetosphere was not responsible for truncating the disk, a boundary layer extending from the surface of the NS could plausibly halt the accretion flow. Equation 2, taken from Popham & Sunyaev (2001), provides a way to estimate the maximum radial extent of this region from the mass accretion rate.

$$\log\left(R_{max} - R_{NS}\right) \simeq 5.02 + 0.245 \left|\log\left(\frac{\dot{M}}{10^{-9.85}\ \mathrm{M_\odot\ yr^{-1}}}\right)\right|^{2.19} \tag{5.2}$$

We determine the mass accretion rate using the unabsorbed luminosity from $0.5 - 50.0$

keV and an accretion efficiency of $\eta = 0.2$ to be $1.1^{+0.1}_{-0.3} \times 10^{-8}$ $M_\odot$ yr^{-1} during the 2016 observation and $2.2 \pm 0.4 \times 10^{-9}$ $M_\odot$ yr^{-1} during the 2014 observation. This gives a maximum radial extent of ~ 10 R_g for the boundary layer during 2016 and ~ 6 R_g during 2014 (assuming canonical values of $M_{NS} = 1.4$ $M_\odot$ and $R_{NS} = 10$ km). This is consistent with the location of the inner disk radius during the 2016 outburst, but falls short of the inner disk radius in our 2014 fits. King et al. (2016) found a similar radial extent of the boundary layer of ~ 7.8 R_g, but this can be increased by rotation of the NS or a change in viscosity to be consistent with the truncation radius.

It is more likely that the magnetic field is responsible for disk truncation in this source. The equatorial magnetic field strength inferred from the Fe line profile ($B \leq 15.0 - 22.5 \times 10^8$ G) is consistent with other estimates of the magnetic field strength ($0.4 - 31 \times 10^8$ G: Campana et al. 1998; Asai et al. 2013; Mukherjee et al. 2015) and are well within the range to truncate an accretion disk (Mukherjee et al. 2015). Following Equation (1) and rearranging for inner disk radius in terms of flux, the inner disk radius should scale like $F_{bol}^{-2/7}$. Thus for magnetic truncation the inner disk radius should decrease as the flux increases, which is what we see for the different observations. Conversely, if the boundary layer were responsible for disk truncation in each case, we should see the inner disk radius increase. Additionally, the maximum extent of the boundary layer during the 2014 observation does not agree with the location of the inner disk radius, pointing to the magnetic field being a more probable explanation for disk truncation. Moreover, although the extent of the boundary layer is consistent with the inner disk radius in the 2016 fits, the behavior of decreasing inner disk radius with increasing flux is indicative of magnetic truncation.

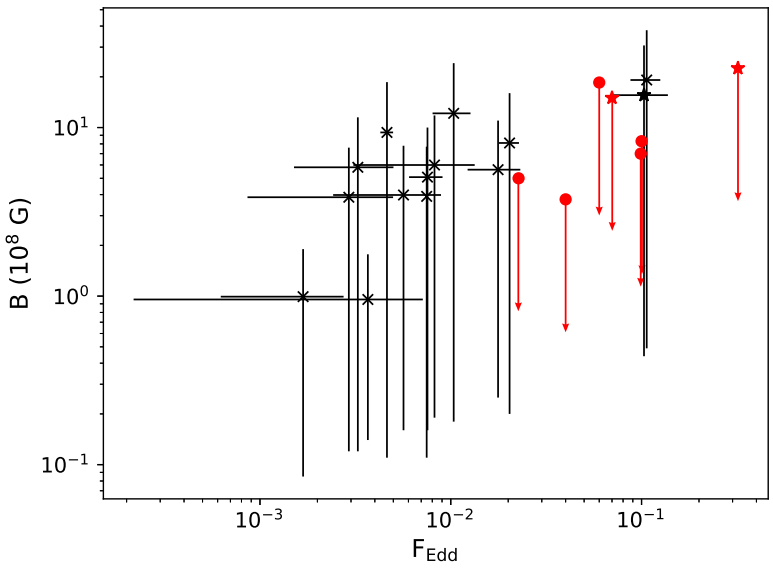

Figure 5.5 Comparison of equatorial magnetic field strengths of NSs in LMXBs (red) inferred from Fe line profiles to known AMXPs (black) reported in Mukherjee et al. (2015) versus Eddington fraction. The stars represent estimates for Aquila X-1. See Table 5.2 for magnetic field strengths and Eddington fraction values.

5.6.1 Comparison of Magnetic Field Strengths

NuSTAR has observed a number of NS LMXBs with Fe lines that imply truncated disks. This has provided a means of placing an upper limit on the strength of their magnetic fields, assuming the disk is truncated at the Alfvén radius (where the ram pressure of the accreting material is balanced by the magnetic pressure outwards). The implied magnetic field strengths reside between $10^8 - 10^9$ G and are similar to accreting millisecond X-ray pulsars (AMXPs). Mukherjee et al. (2015) systematically estimated the upper and lower limits to the equatorial magnetic field strengths of 14 known AMXPs using *Rossi X-ray Timing Explorer* (*RXTE*). They used the highest flux that the source exhibited pulsations and the radius of the NS to determine B_{min} and the lowest flux that exhibited pulsations and corotation radius with the disk to determine B_{max} in each case.

Figure 5.5 presents a comparison of magnetic field strengths of known AMXPs to NS LMXBs observed with *NuSTAR* versus Eddington fraction, $F_{\rm Edd}$. As can be

Table 5.2 Magnetic Field Strengths Versus Eddington Fraction

Source	B (10^8 G)	F_{Edd}	ref.
Swift J1756.9-2508	$0.18 - 24.1$	$0.008 - 0.013$	1
XTE J0929-314	$0.12 - 11.5$	$0.002 - 0.005$	1
XTE J1807.4-294	$0.11 - 18.6$	$0.004 - 0.005$	1
NGC 6440 X-2	$0.12 - 7.6$	$0.001 - 0.005$	1
IGR J17511-3057	$0.19 - 11.8$	$0.003 - 0.013$	1
XTE J1814-338	$0.16 - 7.8$	$0.002 - 0.009$	1
HETE J1900.1-2455	$0.16 - 10.0$	$0.006 - 0.009$	1
SAX J1808.4-3658	$0.14 - 1.77$	$0.0002 - 0.0071$	1
IGR J17498-2921	$0.20 - 16.0$	$0.018 - 0.023$	1
XTE J1751-305	$0.25 - 11.0$	$0.012 - 0.023$	1
SAX J1748.9-2021	$0.49 - 37.8$	$0.09 - 0.12$	1
Swift J1749.4-2807	$0.11 - 7.7$	$0.0074 - 0.0075$	1
IGR J00291+5934	$0.085 - 1.9$	$0.001 - 0.003$	1
Aquila X-1	$0.44 - 30.7$	$0.07 - 0.13$	1
	≤ 15.0	0.07	
	≤ 22.5	0.32	
1RXS J180408.9-3	≤ 5.0	0.02	2
	≤ 8.3	0.10	3
4U 1705-44	≤ 7.0	0.10	4
XTE J1709-267	$\leq 3.8 - 18.5$	$0.04 - 0.06$	5

Note.— (1) Mukherjee et al. 2015; (2) Ludlam et al. 2016; (3) Degenaar et al. 2016; (4) Ludlam et al. 2017a; (5) Ludlam et al. 2017b. All Eddington fraction values are a lower limit since we used the maximum Eddington luminosity value of $L_{\rm Edd} = 3.8 \times 10^{38}$ ergs s^{-1} (Kuulkers et al., 2003).

seen, the NS LMXBs populate higher values of Eddington fraction. Each point from Mukherjee et al. (2015) represents a range in magnetic field strength and $F_{\rm Edd}$ that the AMXP lies and does not embody an actual measurement. Values can be found in Table 5.2. The advantage of magnetic field strengths inferred from the Fe line profiles using *NuSTAR* is that they do not suffer from pile-up or instrumental effects until a source reaches $\sim 10^5$ counts s^{-1}. We use the maximum Eddington luminosity of 3.8×10^{38} ergs s^{-1} from Kuulkers et al. (2003) when calculating the Eddington fraction for each source. If the Eddington luminosity is smaller, all points would be shifted to higher values of Eddington fraction. Therefore, these are all lower limits.

Another caveat of this comparison is that pulsations have not been detected yet for the sources observed with *NuSTAR*. For Aquila X-1 in particular the 2014 observation is within the same $F_{\rm Edd}$ range as the observation taken by *RXTE* when pulsations were detected. Additionally, our upper limit on the strength of the magnetic field agrees with the estimate when pulsations were detected. It is clear that the strengths implied from Fe line profiles are valuable and consistent with those seen for AMXPs. Therefore, Fe lines can be used to estimate magnetic field strengths to first order.

5.7 Summary

We present a reflection study of Aquila X-1 observed with *NuSTAR* during the July 2014 and August 2016 outbursts. We find the disk to be truncated prior to the surface of the NS at $14 \pm 2\ R_g$ during 2014 observation when the source was at 7% of Eddington and $11^{+2}_{-1}\ R_g$ during the 2016 observation when the source was at 32% of Eddington. This implies an upper limit on the strength of the magnetic field at the poles of $3.0 - 4.5 \times 10^9$ G, if the magnetosphere is responsible for truncating the disk in each case. If a boundary layer is responsible for halting the accretion flow instead, we estimate the maximal radial extent to be $\sim 6\ R_g$ for the 2014 observation and $\sim 10\ R_g$ during 2016. These values can be increased through viscous and spin effects,

but the behavior of decreasing inner disk radius with increasing flux favors magnetic truncation. Finally, when comparing the strength of magnetic fields in NS LMXBs to those of known AMXPs we find that they are consistent while probing a higher value of Eddington fraction.

CHAPTER VI

NuSTAR Observations of the Accreting Atolls GX 3+1, 4U 1702−429, 4U 0614+091, and 4U 1746−371

6.1 Preface

The following work is published in the Astrophysical Journal, Volume 873, page 99 (Ludlam et al., 2019) and is co-authored by Jon M. Miller, Didier Barret, Edward M. Cackett, Benjamin M. Coughenour, Thomas Dauser, Nathalie Degenaar, Javier A. García, Fiona A. Harrison, and Frits Paerels. The paper is reproduced here under the non-exclusive rights of republication granted by the American Astronomical Society to the authors of the paper.

6.2 Abstract

Atoll sources are accreting neutron star (NS) low-mass X-ray binaries. We present a spectral analysis of four persistent atoll sources (GX 3+1, 4U 1702−429, 4U 0614 +091, and 4U 1746−371) observed for ~ 20 ks each with *NuSTAR* to determine the extent of the inner accretion disk. These sources range from an apparent luminosity of $0.006 - 0.11$ of the Eddington limit (assuming the empirical limit of 3.8×10^{38}

ergs s^{-1}). Broad Fe emission features shaped by Doppler and relativistic effects close to the NS were firmly detected in three of these sources. The position of the disk appears to be close to the innermost stable circular orbit (ISCO) in each case. For GX 3+1, we determine $R_{in} = 1.8^{+0.2}_{-0.6}\ R_{\rm ISCO}$ (90% confidence level) and an inclination of $27^\circ - 31^\circ$. For 4U 1702−429, we find a $R_{in} = 1.5^{+1.6}_{-0.4}\ R_{\rm ISCO}$ and inclination of $53^\circ - 64^\circ$. For 4U 0614+091, the disk has a position of $R_{in} = 1.3^{+5.4}_{-0.2}\ R_{\rm ISCO}$ and inclination of $50^\circ - 62^\circ$. If the disk does not extend to the innermost stable circular orbit, we can place conservative limits on the magnetic field strength in these systems in the event that the disk is truncated at the Alfvén radius. This provides the limit at the poles of $B \leq 6.7 \times 10^8$ G, 3.3×10^8 G, and 14.5×10^8 G for GX 3+1, 4U 1702−429, and 4U 0614+091, respectively. For 4U 1746−371, we argue that the most plausible explanation for the lack of reflection features is a combination of source geometry and strong Comptonization. We place these sources among the larger sample of NSs that have been observed with *NuSTAR*.

6.3 Introduction

Accretion onto compact objects in low-mass X-ray binaries (LMXBs) occurs via a disk that formed through Roche-lobe overflow from the envelope of the roughly stellar mass companion star. Persistently accreting neutron star (NS) LMXBs are separated into two categories: "Z" and "atoll". These classifications derive their name from the shape they trace out in color-color and hardness-intensity diagrams (Hasinger & van der Klis, 1989). Z sources are very luminous as they likely accrete at near Eddington luminosities ($0.5 - 1.0\ L_{\rm Edd}$: van der Klis 2006), whereas atoll sources are typically less luminous ($\sim 0.001 - 0.5\ L_{\rm Edd}$). Transient systems that alternate between periods of active accretion and quiescence often exhibit atoll-like or Z-like behavior during outburst. Some sources are even able to transition between the two classes (e.g., XTE J1701−462, Homan et al. 2010) suggesting a trend with average mass accretion rate.

Atoll sources generally have two spectral states analogous to black hole (BH) LMXBs: 1) a hard state characterized by power-law emission with little thermal emission, and 2) a soft state dominated by thermal emission. Additionally, they show intermediate behavior as the sources transition between these states (see Wijnands et al. 2017 for a recent discussion on the detailed morphology).

Lin et al. (2007) analyzed the spectrum of two atoll type transients (Aquila X-1 and 4U 1608−52) to devise a "hybrid" model for the hard and soft spectral states. The hard state can be described by a single-temperature blackbody to account for boundary layer emission (where material from the disk reaches the surface of the NS) and a power-law component to account for Comptonization. The soft state can be described by a double thermal model comprised of a multi-temperature blackbody for disk emission and a single-temperature blackbody with the addition of a power-law component. This provided a coherent picture of the spectral evolution (e.g., the thermal components follow $L_{\rm X} \propto T^4$) and timing behavior of these sources that is analogous to BHs, which has been utilized for a number of other NS LMXBs (e.g., Cackett et al. 2008, 2009, 2010; Lin et al 2010; Miller et al. 2013; Chiang et al. 2016a).

The hard X-ray photons that originate from the boundary layer or coronal region can illuminate the disk and be reprocessed by the material therein before being re-emitted. This reprocessed emission is known as the "reflection" spectrum. Doppler and relativistic effects are imprinted on features in the reflection spectrum, such as Fe K_α, yielding information about accretion flow (Fabian et al., 1989). The strength of these effects increase with proximity to the compact object, thus allowing the position of the inner accretion disk to be determined from the shape of the Fe line profile. The accretion disk around a NS has to truncate at or prior to the surface, hence reflection studies in NS LMXBs can provide upper limits on the radial extent of these objects (Cackett et al. 2008; Miller et al. 2013; Ludlam et al. 2017a) or indicate the presence of a boundary layer or strong magnetic field (Cackett et al. 2009; Papitto et al. 2009;

King et al. 2016; Ludlam et al. 2017b, 2017c; van den Eijnden et al. 2017).

The location of the inner edge of the accretion disk around compact objects is thought to be dependent on the mass accretion rate, $\dot{m}$, of the system (González Martínez-País et al. 2014 for a review). Indeed, the overall spectral evolution of atolls does change with $\dot{m}$ (Gladstone et al., 2007), but there does not appear to be a clear one-to-one correlation with the inner disk position (Cackett et al. 2010; Chiang et al. 2016a; Ludlam et al. 2017a). When looking at a sample of NS LMXBs from which the inner disk radius could be determined via reflection, some atoll sources were consistent with the innermost stable circular orbit (ISCO) at as low as 1% L_{Edd}, whereas others were truncated at higher accretion rates near 10% L_{Edd} (Ludlam et al., 2017a). This suggests a more complex behavior for the position on the inner accretion disk that relies on more than just $\dot{m}$ (e.g., the importance of the magnetosphere or boundary layer).

We present a sample of four persistently accreting atoll sources that were approved an initial ~ 20 ks observation each with *NuSTAR* (Harrison et al., 2013) during GO Cycle 3: GX 3+1, 4U 1702−429, 4U 0614+091, and 4U 1746−371. We search for the presence of reflection features and place constraints on the position of the inner disk. *NuSTAR* has been an exceptional tool for reflection studies due to its large energy bandpass from $3-79$ keV, as well as its high effective collecting area that is free from instrumental effects such as pile-up. Our sample spans the range of 0.006 to 0.11 L_{Edd}, assuming the empirical Eddington limit of 3.8×10^{38} ergs s^{-1}(Kuulkers et al., 2003). The paper is structured in the following format: the subsequent subsections provide background on each source (§6.3.1, 6.3.2, 6.3.3, 6.3.4), §6.4 presents the observations and data reduction, §6.5 discusses the spectral analysis and results, §6.6 provides a discussion of the results, §6.7 summarizes the discussion.

6.3.1 GX 3+1

GX 3+1 is known to exhibit both Type-I X-ray bursts (Makishima et al. 1983; Kuulkers & van der Klis 2000; Chenevez et al. 2006) and longer duration superbursts from carbon burning (Kuulkers et al., 2002). Imposing the assumption that the Type-I X-ray bursts are Eddington limited provides a maximum distance to the source of 6.5 kpc (Galloway et al., 2008). A broad Fe line was first detected in this source with *Beppo*SAX (Oosterbroek et al., 2001). *XMM-Newton* observations of the source confirmed the presence of a relativistically shaped Fe line and revealed potential lower-energy features due to Ar XVIII and Ca XIX (Piraino et al., 2012). The Fe line profile suggested that the inner disk was located at a distance of $\sim 25\ R_g$ (where $R_g = GM/c^2$) with an inclination of $35^\circ - 44^\circ$ when fit with a simple DISKLINE model (Fabian et al., 1989). Pintore et al. (2015) analyzed *XMM-Newton* and *INTEGRAL* observations from 2010 which suggested that the disk was closer to the NS at $\sim 10\ R_g$ with an inclination of $\sim 35^\circ$ when accounting for the entire reflection spectrum.

6.3.2 4U 1702−429

4U 1702−429 is a burster (Swank et al., 1976) located at a maximum distance of 5.65 kpc (Galloway et al., 2008), assuming that the Type-I X-ray bursts are Eddington limited. Burst oscillations were detected at a frequency of 330 Hz with the *Rossi X-ray Timing Explorer* (*RXTE*) (Markwardt et al., 1999), which is indicative of the spin frequency of the NS. This spin frequency corresponds to a dimensionless spin parameter ($a = cJ/GM^2$) of 0.155 (Braje et al., 2000), assuming a NS mass of 1.4 $M_\odot$, a 10 km radius, and softish equation of state of the 'FPS' model (Cook, Shapiro, & Teukolsky, 1994). Iaria et al. (2016) provided the first investigation of the broadband spectrum using observations from both *XMM-Newton* and *INTEGRAL*. This revealed a broad Fe line component that originated from a significantly truncated disk with an inner disk radius of $31^{+25}_{-12}\ R_g$ and implied an inclination of $44^{+33\circ}_{-6}$.

6.3.3 4U 0614+091

4U 0614+091 is an ultracompact X-ray binary (UCXB) with an orbital period of ~ 50 minutes (Shahbaz et al., 2008) located at a distance of 3.2 kpc (Kuulkers et al., 2010). Type-I X-ray bursts have been detected in this system (Swank et al. 1978; Brandt et al. 1992) confirming that the compact object is a NS. A spin frequency of 415 Hz (Strohmayer et al., 2008) was determined from burst oscillations, which translates to $a = 0.2$ using the formalism from Braje et al. (2000). The companion star is either a CO or ONe white dwarf due to carbon and oxygen emission lines present in the optical spectrum (Nelemans et al., 2004). Madej et al. (2010) detected relativistically broadened O VIII Ly_α emission in the *XMM-Newton* Reflection Grating Spectrometer detectors. When modeling the O VIII Ly_α emission with a relativistic line profile, this emission appeared to originate from the innermost region ($\sim 6\ R_g$) of a highly inclined disk ($i \approx 54°$). A follow up study using the *XMM-Newton*/EPIC-pn data additionally revealed the presence of an Fe line feature (Madej et al., 2014). Spectral modeling of both features via a specially tailored reflection spectrum model for an overabundance of C and O, $\mathrm{XILLVER_{CO}}$, supported the previous results of a disk close to the ISCO with a moderate inclination.

6.3.4 4U 1746−371

4U 1746−371 is associated with the globular cluster NGC 6441. Variable stars in the cluster establish the distance to NGC 6441 to between $10.4 - 11.9$ kpc (Pritzl et al., 2001). The source is known to experience Type-I X-ray bursts (Sztajno et al. 1987) and is a dipping source (Parmar et al., 1989), which indicates that the system is highly inclined. The periodicity of the dipping observed with *Ginga* suggested an orbital period of ~ 5.7 hours (Sansom et al., 1993), but follow-up studies with *RXTE* found a smaller period of 5.16 ± 0.01 hours (Bałucińska-Church et al., 2004). *Hubble Space Telescope* imaging of the globular cluster identified five possible optical coun-

terparts, but the field was too dense to isolate a single counterpart as the companion to 4U 1746−371 (Deutsch et al., 1998). Asai et al. (2000) found evidence of a potential narrow Fe line in *ASCA* data, whereas a later investigation by Díaz Trigo et al. (2006) with *XMM-Newton* suggested a broad Fe emission component (modeled with a Gaussian at 6.4 keV that provided a 3.5σ improvement) with a potential narrow Fe XXVI absorption line.

6.4 Observations and Data Reduction

Table 6.1 provides the ObsIDs, date, exposure time, and net count rate of each *NuSTAR* observation. We followed the standard data reduction procedures using NUSTARDAS v1.8.0 with CALDB 20180126 for each observation. GX 3+1 and 4U 0614 +091 required additional parameters to be called when utilizing the NUPIPELINE tool. GX 3+1 is considered a formally bright source for *NuSTAR* (> 100 counts s^{-1}), so we applied STATUSEXPR="STATUS==b0000xxx00xxxx000" to correct for high count rates. The observation of 4U 0614+091 occurred during high intervals of background near the South Atlantic Anomaly (SAA), therefore we imposed SAACALC = 3, SAAMODE=strict, and TENTACLE=yes to reduce these periods. Using the NUPRODUCTS tool we created lightcurves and spectra for each observation using a circular extraction region with a radius of 100″ centered around the source to produce a source spectrum for both the Focal Plane Modules (FPMA and FPMB). We use another 100″ radial region away from the source for the purpose of background subtraction. No Type-I X-ray bursts were present in the lightcurves. Although it is not generally recommended to combine data from the FPMA/B since the introduced systematics may be larger than the statistical errors in high signal-to-noise observations, most of the sources in our sample have a low signal-to-noise. Therefore, we combine the FPMA/B using ADDASCASPEC to improve the signal-to-noise and provide a uniform analysis among sources in this sample. The data were binned by a

Table 6.1 *NuSTAR* Observation Information

Source	Mission	Obs ID	Date (yyyy-mm-dd)	Exp (ks)	Net Rate (cts s^{-1})
GX 3+1	*NuSTAR*	30363001002	2017-10-17	13.7	147.9
4U 1702−429	*NuSTAR*	30363005002	2017-08-29	21.7	97.1
4U 0614+091	*NuSTAR*	30363002002	2017-12-01	15.1	28.3
4U 1746−371	*NuSTAR*	30363004002	2018-02-10	19.8	10.7

factor of 3 using GRPPHA (Choudhury et al., 2017).

6.5 Spectral Analysis and Results

We use XSPEC version 12.9.1m (Arnaud, 1996) to perform our spectral analysis. Errors are generated from Monte Carlo Markov Chains of length 500,000 in order to simultaneously probe the entire χ^2 parameter space and quoted at the 90% confidence level. We use TBABS (Wilms et al., 2000) to account for absorption along the line of sight to each source with the abundance set to WILM (Wilms et al., 2000) and VERN cross-sections (Verner et al., 1996). The upper limit on the energy range in which each source is modeled is background limited.

Since the *NuSTAR* low-energy bandpass cuts off at 3 keV, we are unable to constrain the absorption column along the line of sight. We utilize archival *XMM-Newton*/RGS data to fit absorption edges with TBNEW[1] to determine N_H for each source. Note that these observations are not simultaneous with our *NuSTAR* observations. The RGS data were fit in the $0.45 - 2.1$ keV energy range. We find $N_H = 2.42 \pm 0.02 \times 10^{22}$ cm^{-2} for GX 3+1, $N_H = 2.32 \pm 0.06 \times 10^{22}$ cm^{-2} for 4U 1702−429, $N_H = 3.46 \pm 0.01 \times 10^{21}$ cm^{-2} for 4U 0614+091, and $N_H = 3.76 \pm 0.01 \times 10^{21}$ cm^{-2} for 4U 1746−371. We compare these values to those reported in previous studies on these sources and find good agreement (e.g., GX 3+1: Pintore et al. 2015, 4U 1702−429: Mazzola et al. 2018, 4U 0614+091: Madej et al. 2010, 2014, 4U 1746−371: Díaz Trigo et al. 2006). We therefore fix N_H in the following *NuSTAR* fits since column density is dominated by the interstellar medium and does not vary with spectral state (Miller et al., 2009). This is certainly true for low inclination source, but there can be deviations for high inclination sources due to obscuration within the system itself during dips or eclipses. However, note that the higher inclination sources in this sample do not show dips during our observations.

[1] http://pulsar.sternwarte.uni-erlangen.de/wilms/research/tbabs/

The continuum is modeled based upon the prescription in Lin et al. (2007) for atoll sources. This is largely motivated by the existence of self-consistent reflection models based upon these components. We check, when appropriate, that our choice of continuum does not bias our results. Only GX 3+1 showed a very soft spectrum consistent with the soft state. The spectrum was modeled with a multi-temperature blackbody (DISKBB; Mitsuda et al. 1984), single-temperature blackbody (BBODY), and power-law component (POWERLAW). The other sources exhibited spectra consistent with hard state and are therefore modeled with a power-law component (CUTOFFPL) and single-temperature blackbody (BBODY) when needed.

When reflection features are present in the spectra, we utilize the self-consistent reflection model RELXILL (García et al., 2014) or the preliminarily flavor of this model tailored to thermal emission from a NS RELXILLNS (Dauser, García, & Ludlam *in prep.*). The major difference between these models is the illuminating continuum that provides the hard X-rays that shape the resulting reflection spectrum. RELXILL uses a cutoff power-law input spectrum whereas RELXILLNS assumes a blackbody is irradiating the disk. The model components of RELXILL are as follows: q_1 is the inner emissivity index, q_2 is the outer emissivity index, R_{break} is the break radius between the two emissivity indices, a is the dimensionless spin parameter, i is the inclination in degrees, R_{in} is the inner disk radius in units of the innermost stable circular orbit ($R_{\rm ISCO}$), R_{out} is the outer disk radius in units of gravitational radius ($R_g = GM/c^2$), Γ is the photon index of the input cutoff power-law, $\log \xi$ is the log of the ionization parameter, A_{Fe} is the iron abundance of the system normalized to the Sun, $\rm E_{cut}$ is the cutoff energy, $f_{\rm refl}$ is the reflection fraction, z is the redshift to the object, and norm represents the normalization of the model. RELXILLNS has similar parameters with the addition of $\log n$ ($\rm cm^{-3}$) to vary the density of the accretion disk and kT_{bb} (keV) for the input blackbody spectrum instead of Γ and $\rm E_{cut}$.

When using the reflection models we impose the following: a single emissivity

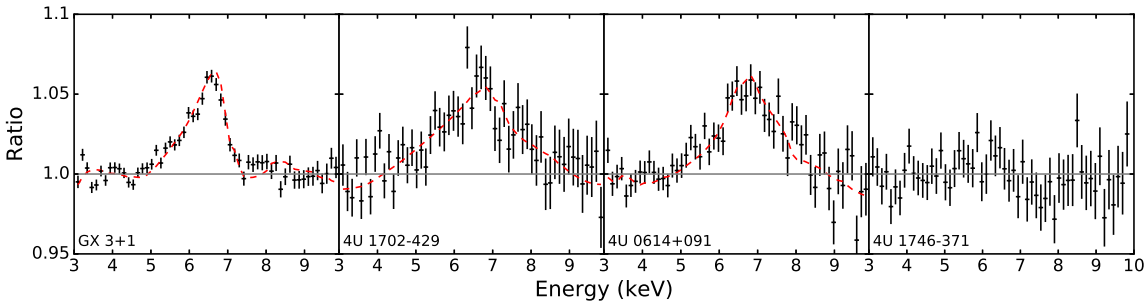

Figure 6.1 Ratio of the data to the continuum model for the atoll sources. The $5.0-8.0$ keV energy band was ignored to prevent the Fe line region from skewing the fit. The dashed red line indicates the Fe line profile from the reflection continuum.

index $q = q_1 = q_2$, a redshift of $z = 0$ since these are Galactic sources, a spin of $a = 0$ since most NS in LMXBs have $a \leq 0.3$ (Galloway et al. 2008; Miller et al. 2011) and the ISCO is a slowly varying function in this regime, and a large outer disk radius of $R_{out} = 990\ R_g$. For reference, $1\ R_{\rm ISCO} = 6\ R_g$ for $a = 0$ (Bardeen et al., 1972). In the case of 4U 1702−429 and 4U 0614+091 where burst oscillations imply $a = 0.155$ and $a = 0.199$, the assumption of $a = 0$ is a marginal difference of $< 0.7\ R_g$ for the position of the ISCO.

6.5.1 GX 3+1

The *NuSTAR* data were modeled in the $3.0 - 20.0$ keV range. The continuum model includes a multi-temperature blackbody, single-temperature blackbody, and power-law component. This provides a poor fit ($\chi^2/dof = 1491.4/135$) to the *NuSTAR* data due to the presence of reflection features that are not accounted for by this model. The Fe line profile from the data can be seen in Figure 6.1. We utilize the self-consistent thermal reflection model of RELXILLNS to properly describe these features. This improves the fit significantly to $\chi^2/dof = 199.0/128$ (15σ improvement via F-test), though this is still a poor statistical fit overall since the high S/N for this source places the data in the systematic and calibration limited regime. The

power-law component is still statistically needed at the 9.5σ level of confidence. The disk blackbody normalization implies an incredibly small radius ($\sim$ 2.5 km), even after applying color corrections. This is likely to be a result of spectral hardening of pure blackbody emission by an atmosphere (London et al. 1986; Shimura & Takahara 1995; Merloni et al. 2000). We replace the DISKBB & POWER-LAW components with NTHCOMP, setting the photon seed input to a disk blackbody. This improves the overall fit further ($\Delta\chi^2 = 34.1$) implying a high optical depth of $\tau \sim 7$, but does not change the results for important parameters, i.e., R_{in} and inclination. The values for reflection model fitting are provided in Table 6.2. Note that RELXILLNS still contains a single-temperature blackbody continuum component in Model 2. The spectral components and ratio of the data to the overall model can be seen in panel (a) and (b) of Figure 6.2.

There is a flavor of RELXILL, known as RELXILLCP, that allows for reflection from a Comptonized disk component. This model has a hard-coded seed photon temperature of 0.05 keV. This is not appropriate for most NS spectral states, but it was recently employed successfully to model the accreting millisecond pulsar SAX J1808.4-3658 by Di Salvo et al. (2019). Since we find a low seed photon temperature of $\sim$ 0.09 keV in our continuum fit with NTHCOMP, we attempt to use RELXILLCP instead of RELXILLNS. The overall model used in XSPEC is TBABS*(BBODY+RELXILLCP). This provides a significantly worse fit ($\chi^2/dof = 344.6/130$ or $> 9\sigma$ worse). We show these results in Table 6.8 and Figure 6.4 of the appendix, but do not report on it further.

6.5.2 4U 1702−429

The *NuSTAR* data were modeled in the $3.0 - 50.0$ keV energy band. The continuum is well described by a cutoff power-law alone ($\chi^2/dof = 1162.4/388$), but there is a broad Fe line feature present in the ratio of the data to the continuum (Figure 6.1). In order to accommodate this feature, we apply the standard version of

Table 6.2 Reflection Modeling of GX 3+1

Model	Parameter	Model 1	Model 2
TBABS	N_H (10^{22} cm^{-2})	$2.42^{\dagger}$	$2.42^{\dagger}$
DISKBB	kT (keV)	$1.84^{+0.11}_{-0.01}$	...
	norm	$15.3^{+0.4}_{-2.7}$	...
POWERLAW	Γ	3.5 ± 0.1	...
	norm	$1.04^{+0.09}_{-0.02}$	...
NTHCOMP	Γ	...	$1.83^{+0.04}_{-0.01}$
	kT_e (keV)	...	2.45 ± 0.04
	kT_{bb} (keV)	...	$0.09^{+0.15}_{-0.08}$
	norm	...	0.86 ± 0.02
RELXILLNS	q	$3.2^{+0.1}_{-0.6}$	2.8 ± 0.5
	i ($^\circ$)	28^{+3}_{-1}	25 ± 1
	R_{in} ($R_{\rm ISCO}$)	$1.8^{+0.2}_{-0.6}$	2.2 ± 0.2
	R_{in} (R_g)	$10.8^{+1.2}_{-3.6}$	13.2 ± 1.2
	kT_{bb} (keV)	$2.60^{+0.04}_{-0.02}$	1.6 ± 0.1
	$\log \xi$	$2.75^{+0.05}_{-0.10}$	$3.2^{+0.1}_{-0.2}$
	A_{Fe}	$0.62^{+0.17}_{-0.03}$	3 ± 2
	$\log n$ (cm^{-3})	$16.6^{+0.2}_{-0.3}$	$16.1^{+0.2}_{-0.1}$
	$f_{\rm refl}$	$0.93^{+0.04}_{-0.01}$	0.39 ± 0.07
	norm (10^{-3})	$0.72^{+0.05}_{-0.12}$	1.2 ± 0.2
	$F_{\rm unabs}$	8^{+1}_{-2}	6.5 ± 1.1
	L (10^{37} ergs s^{-1})	$4.1^{+0.5}_{-1.0}$	3.3 ± 0.6
	$L/L_{\rm Edd}$	0.11	0.10
	χ^2 (dof)	199.0 (128)	164.9 (128)

† = fixed

Note.— Errors are reported at the 90% confidence level and calculated from Markov chain Monte Carlo (MCMC) of chain length 500,000. Data were fit in the $3.0 - 20.0$ keV band. The outer disk radius was fixed at 990 R_g, the dimensionless spin parameter and redshift were set to zero for the RELXILLNS model. $f_{\rm refl}$ denotes the reflection fraction. The unabsorbed flux is taken in the $0.5 - 50.0$ keV band and given in units of 10^{-9} ergs cm^{-2} s^{-1}. Luminosity is calculated based upon a distance of $D_{\rm max} = 6.5$ kpc (Galloway et al., 2008).

the self-consistent reflection model RELXILL. We initially fix the iron abundance at twice solar since the fit tended towards the maximum value of $A_{Fe} = 10$. Applying the reflection model with $A_{Fe} = 2$ provides a $\sim 17\sigma$ improvement in the overall fit ($\chi^2/dof = 526.6/383$) in comparison the continuum only model. Last, we explore the dependence on the iron abundance by allowing it to be a free parameter. The value is greater than 4.6 times the solar value, but the position of the inner disk is consistent with the fit that had a fixed A_{Fe}. Both fits are reported in Table 6.3. This overabundance could be indicative of a higher density disk than the hard coded value of 10^{15} cm^{-3} in RELXILL. We note that the model flavor RELXILLD provides the option of variable density in the disk. However, the current version of this model has a fixed cutoff energy of 300 keV, which is much higher than the value required to fit these data. Panel (c) of Figure 6.2 shows the model components and ratio of the *NuSTAR* fit with A_{Fe} left free to vary. Additionally, we also try fitting the spectrum with RELXILLCP, but do not find an improvement in the overall fit ($\Delta\chi^2$ increases by 4.7 for the same number of degrees of freedom). We present this in Table 6.8 and Figure 6.4 in the appendix.

6.5.3 4U 0614+091

The *NuSTAR* data were modeled in the $3.0 - 30.0$ keV energy band. The column density was fixed at the value inferred from fitting the *XMM-Newton*/RGS of $N_H = 3.46 \times 10^{21}$ cm^{-2}. The continuum is consistent with the hard state, which is well described by a single-temperature blackbody and cutoff power-law ($\chi^2/dof = 457.3/220$). There is a broad emission feature in the Fe K band that can be seen in Figure 6.1. We employ RELXILL to account for the reflected emission. This provides a $\sim 10\sigma$ improvement in the overall fit. Parameter values are given in Table 6.4. The spectrum and spectral components can be seen in panel (d) of Figure 6.2.

Table 6.3 Reflection Modeling of 4U 1702-429

Model	Parameter	Fixed A_{Fe}	Free A_{Fe}
TBABS	N_H (10^{22} cm^{-2})	$2.32^{\dagger}$	$2.32^{\dagger}$
RELXILL	q	$2.5^{+1.2}_{-0.3}$	$2.5^{+1.4}_{-0.1}$
	i ($^\circ$)	59^{+5}_{-6}	61^{+2}_{-14}
	R_{in} ($R_{\rm ISCO}$)	$1.5^{+1.6}_{-0.4}$	$1.6^{+2.9}_{-0.1}$
	R_{in} (R_g)	$9.0^{+9.6}_{-2.4}$	$9.6^{+17.4}_{-0.6}$
	Γ	$1.97^{+0.02}_{-0.04}$	$1.97^{+0.02}_{-0.03}$
	$\log \xi$	$3.74^{+0.25}_{-0.03}$	$4.02^{+0.33}_{-0.03}$
	A_{Fe}	$2.0^{\dagger}$	$4.9^{+4.6}_{-0.3}$
	$E_{\rm cut}$	53^{+11}_{-2}	57^{+9}_{-4}
	$f_{\rm refl}$	$0.57^{+0.92}_{-0.01}$	$0.5^{+0.1}_{-0.2}$
	norm (10^{-3})	$0.70^{+0.04}_{-0.30}$	$0.75^{+0.09}_{-0.05}$
	$F_{\rm unabs}$	$0.58^{+0.03}_{-0.25}$	$0.57^{+0.07}_{-0.04}$
	L (10^{36} ergs s^{-1})	$2.2^{+0.1}_{-0.9}$	$2.2^{+0.3}_{-0.1}$
	$L/L_{\rm Edd}$	0.006	0.006
	χ^2 (d.o.f.)	526.6 (383)	480.2 (382)

† = fixed

Note.— Errors are reported at the 90% confidence level and calculated from Markov chain Monte Carlo (MCMC) of chain length 500,000. *NuSTAR* data were fit in the $3.0 - 50.0$ keV band. The outer disk radius was fixed at 990 R_g, the dimensionless spin parameter and redshift were set to zero for the RELXILL model. $f_{\rm refl}$ denotes the reflection fraction. The unabsorbed flux is taken in the $0.5 - 50.0$ keV band and given in units of 10^{-9} ergs cm^{-2} s^{-1}. Luminosity is calculated based upon a distance of $D_{\rm max} = 5.65$ kpc (Galloway et al., 2008).

Table 6.4 Reflection Modeling of 4U 0614+091

Model	Parameter	*NuSTAR*
TBABS	N_H (10^{21} cm^{-2})	$3.46^{\dagger}$
BBODY	kT (keV)	$1.51^{+0.03}_{-0.01}$
	norm (10^{-3})	$3.55^{+0.04}_{-0.42}$
RELXILL	q	$2.07^{+0.50}_{-0.04}$
	i ($^{\circ}$)	52^{+10}_{-2}
	R_{in} ($R_{\rm ISCO}$)	$1.3^{+5.4}_{-0.2}$
	R_{in} (R_g)	$7.8^{+32.4}_{-1.2}$
	Γ	$2.57^{+0.03}_{-0.24}$
	$\log \xi$	$3.35^{+0.12}_{-0.06}$
	A_{Fe}	$0.58^{+0.86}_{-0.06}$
	$E_{\rm cut}$	16^{+1}_{-4}
	$f_{\rm refl}$	$1.0^{+0.3}_{-0.4}$
	norm (10^{-3})	$4.1^{+0.6}_{-1.1}$
	$F_{\rm unabs}$	$2.2^{+0.3}_{-0.6}$
	L (10^{36} ergs s^{-1})	$2.7^{+0.4}_{-0.7}$
	$L/L_{\rm Edd}$	0.007
	χ^2 (d.o.f.)	249.8 (213)

† = fixed

Note.— Errors are reported at the 90% confidence level and calculated from Markov chain Monte Carlo (MCMC) of chain length 500,000. The data were fit in the $3.0 - 30.0$ keV band. The outer disk radius was fixed at 990 R_g, the dimensionless spin parameter and redshift were set to zero for the RELXILL model. $f_{\rm refl}$ denotes the reflection fraction. The unabsorbed flux is taken in the $0.5 - 50.0$ keV band and given in units of 10^{-9} ergs cm^{-2} s^{-1}. Luminosity is calculated based upon a distance of $D_{\rm max} = 3.2$ kpc (Kuulkers et al., 2010).

6.5.4 4U 1746−371

The *NuSTAR* data were modeled in the $3.0-25.0$ keV band. The column density along the line of sight is fixed at $N_H = 3.76 \times 10^{21}$ cm^{-2}. The spectrum can be entirely described by a cutoff power-law and single temperature blackbody component ($\chi^2/dof = 224.3/177$). There is not a strong detection of an Fe line component (see Figure 6.1). Applying a Gaussian component at 6.4 keV provides a marginal improvement of $\chi^2/dof = 211.3/175$ (or 2.8σ) with an equivalent width of ~ 30 eV. Allowing the spectrum to be described by reflection with RELXILL provides an improvement in the fit ($\Delta\chi^2$ decreases by 17.7 for 2 dof). This is a 3.4σ improvement in comparison to the continuum only modeling. We fixed the following parameter values in the reflection model to those typical of other sources: $q = 3.2$ (Wilkins, 2018), $R_{in} = 1\ R_{\rm ISCO}$, $A_{Fe} = 1$, $\log(\xi) = 3.0$, and an inclination of $i = 75°$ (because it is a "dipping" source). We can then place an upper limit on the presence of reflection to be 13% from the reflection fraction. Allowing the fixed parameters within RELXILL to be free does not provide any meaningful constraints. For example, the inner disk radius is completely unconstrained (i.e., consistent with both hard-coded limits of $1\ R_{\rm ISCO}$ and $100\ R_{\rm ISCO}$). This was also the case for the ionization parameter which was consistent with $\log \xi = 0$ and $\log \xi = 4.7$. We therefore are unable to learn more information about the reflected component.

The source is likely highly Comptonized. Switching out the continuum for Comptonization alone (NTHCOMP: Zdziarski et al. 1996; Zycki et al. 1999) provides a comparatively good fit ($\chi^2/dof = 226.4/178$) and implies a high optical depth of $\tau \sim 6$. Both continuum model fits are reported in Table 6.5. The spectrum and spectral components for each fit can be seen in panels (e) and (f) of Figure 6.2. We try to apply RELXILLCP to again check the presence of reflection in this observation. We fix the same parameters as the fit performed with RELXILL while allowing the continuum parameters, reflection fraction, and normalization to vary. This provides

Table 6.5 Continuum Modeling of 4U 1746-371

Model	Parameter	Power-law	Comptonization
TBABS	N_H (10^{21} cm^{-2})	$3.76^{\dagger}$	$3.76^{\dagger}$
BBODY	kT (keV)	2.4 ± 0.2	...
	norm (10^{-4})	5.4 ± 0.9	...
CUTOFFPL	Γ	1.3 ± 0.2	...
	E_{cut}	5.5 ± 0.7	...
	norm (10^{-2})	6.6 ± 0.7	...
NTHCOMP	Γ	...	1.91 ± 0.02
	kT_e (keV)	...	2.91 ± 0.04
	kT_{bb} (keV)	...	$0.50^{+0.04}_{-0.05}$
	norm (10^{-2})	...	$2.4^{+0.4}_{-0.3}$
	F_{unabs}	0.45 ± 0.09	$0.34^{+0.06}_{-0.04}$
	L (10^{36} ergs s^{-1})	8 ± 2	$5.8^{+1.0}_{-0.7}$
	L/L_{Edd}	0.02	0.015
	χ^2 (d.o.f.)	224.3 (177)	226.4 (178)

† = fixed

Note.— Errors are reported at the 90% confidence level and calculated from Markov chain Monte Carlo (MCMC) of chain length 500,000. *NuSTAR* was fit in the $3.0 - 25.0$ keV band. The unabsorbed flux is taken in the $0.5 - 50.0$ keV band and given in units of 10^{-9} ergs cm^{-2} s^{-1}. Luminosity is calculated based upon a distance of $D_{max} = 11.9$ kpc (Pritzl et al., 2001).

an improvement over the spectral modeling with NTHCOMP alone ($\Delta\chi^2$=11 for the same number of dof). We obtain a higher upper limit on the presence of reflection ($\sim$ 56%), but we are still unable to constrain reflection parameter values when they are allowed to vary. The combination of high inclination and strong Comptonization could be responsible for scattering any potential reflection features in this system out of the line of sight (see Figure 5 of Petrucci et al. 2001) and suggests we are observing through the Comptonizing corona that is on top of the accretion disk.

6.6 Discussion

We perform a time-averaged spectral analysis with a focus on detecting reflection features in a sample of accreting atoll sources that were granted $\sim$ 20 ks observa-

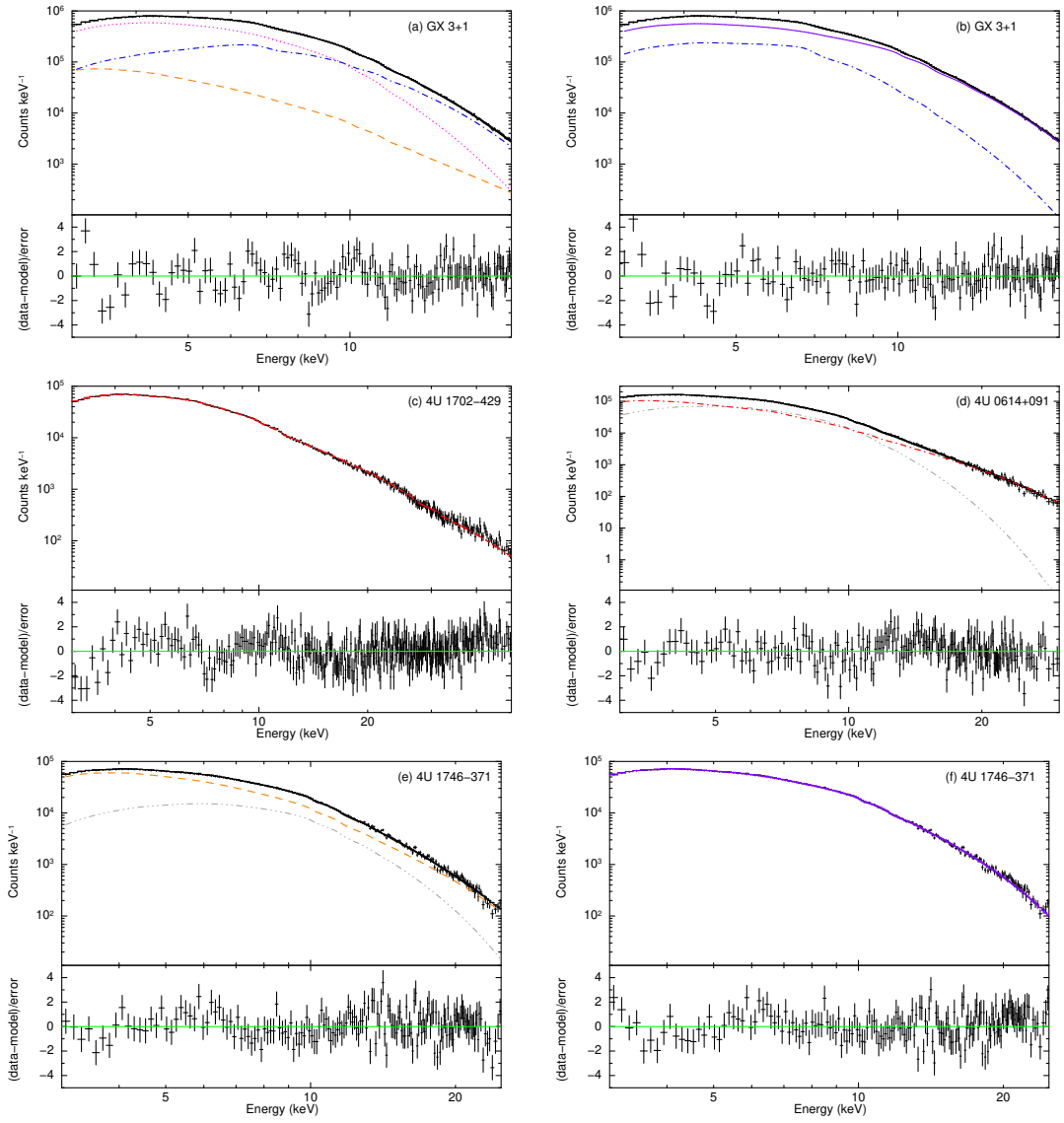

Figure 6.2 *NuSTAR* spectral modeling and residuals divided by errors for the sample of atoll sources. Dot-dashed lines indicate the reflection model (blue: RELXILLNS, red: RELXILL). The magenta dotted line is a multi-temperature blackbody to account for disk emission. The grey dot-dot-dot dashed line is a single-temperature blackbody to account for boundary layer emission. The orange dashed line indicates the power-law component. The purple solid line is the Comptonization model. See Tables 6.2-6.5 for component parameters.

tions per source with *NuSTAR* to determine the position of the inner disk. The sources span a range in Eddington fraction from $0.006 - 0.11$ (assuming the empirical limit of 3.8×10^{38} ergs s^{-1}). Broad Fe lines were detected in three out of four of the sources: GX 3+1, 4U 1702−429, and 4U 0614+091. We account for reflection by using different flavors of RELXILL based on the illuminating continuum in these systems. There are other families of reflection models, such as REFLIONX (Ross & Fabian, 2005) or BBREFL (Ballantyne, 2004), but Ludlam et al. (2017a) demonstrated that reflection fitting with these models provide similar results as RELXILL. The final source, 4U 1746−371, does not require reflection in order to describe the spectrum. However, we can place an upper limit on its presence through the reflection fraction to be $13\% - 56\%$ depending on the choice of the illuminating continuum. The ionization parameters of the three sources with reflection are consistent with $\log \xi = 2.3 - 4.0$ seen in other NS LMXBs (Cackett et al. 2010; Ludlam et al. 2017a).

GX 3+1 displayed a particularly soft spectrum that was well described by a double thermal model with a power-law component. The reflection model determined the accretion disk was truncated prior to the ISCO at $1.8^{+0.2}_{-0.6}$ $R_{\rm ISCO}$ ($10.8^{+1.2}_{-3.6}$ R_g) and inclination of $27^\circ - 31^\circ$. The inner disk position agrees with the $\sim$ 10 R_g limit found by Pintore et al. (2015), but the inclination is slightly lower than previous investigations with *XMM-Newton* by Piraino et al. (2012) and Pintore et al. (2015). A potential source of the discrepancy between the measured inclinations could be due to the difference in N_H used when performing spectral fits. The choice of absorption model used (e.g., WABS, PHABS, TBABS, etc.), as well as abundances and cross-sections adopted can result in changes in the measured N_H by up to 30% (Gatuzz & García, in prep.). This can alter the edge at 7 keV in the Fe line region, which can impact the blue wing predicted by the reflection model when fitting, and therefore lead to changes in the inferred inclination. Additionally, we obtain similar values for R_{in} and inclination when using a Comptonized disk blackbody component for the continuum.

The position of the inner disk was close to the ISCO for 4U 1702−429, though the large error bars are also compatible with disk truncation. This is in agreement with the values reported in Mazzola et al. (2018) from archival *XMM-Newton*, *INTEGRAL*, and *BeppoSAX* observations. The iron abundance had to be fixed during the reflection fits. Allowing the iron abundance vary required $> 5\times$ the solar abundance. This improved the fit, but the disk was highly ionized ($\log \xi \simeq 4$). The super-solar abundance likely indicates that the disk has a higher density than accounted for by the RELXILL model (10^{15} cm^{-3}). This behavior was also seen for the BH HMXB Cyg X-1 (Tomsick et al., 2018) which had a super-solar Fe abundance when modeled with a disk density of 10^{15} cm^{-3}. When the disk density was allowed to increase, the Fe abundance in the reflection model decreased. See García et al. (2018) for a recent discussion on the relationship between disk density and inferred Fe abundance. The inclination is between $53^\circ - 64^\circ$ depending on the value of A_{Fe}, in agreement with the results from Iaria et al. (2016) from *XMM-Newton* and *INTEGRAL* data. Additionally, the upper limits on the inner disk position when $A_{Fe} = 2.0$ are consistent with the values reported in Iaria et al. (2016).

4U 0614−091 was also truncated slightly outside of the ISCO. The sub-solar Fe abundance agrees with previous studies and the nature of the donor in this system (Madej et al. 2010; 2014), although the abundance is consistent with solar at the 90% confidence level. The inclination of the system from RELXILL is $50^\circ - 62^\circ$, which again agrees with the results from the *XMM-Newton* RGS and EPIC-pn studies performed by Madej et al. (2010, 2014). This supports the idea that relativistically blurred Fe and O lines can originate from very similar regions in the disk providing additional diagnostics for the inner accretion flow in these systems (Ludlam et al., 2016). Future studies conducted with observatories such as *NICER* (Gendreau et al., 2012) that are sensitive to Fe lines and lower energy emission features simultaneously can confirm if these locations are the same or mutually exclusive.

Further observations of 4U 1702−429 and 4U 0614−091 would yield tighter constraints on the position of the inner disk radius to determine if the accretion flow is truncated or close to the NS, particularly if 4U 1702−429 is targeted in a state with higher intensity. Additionally, the development of a cutoff power-law reflection model with variable disk density and cutoff energy will shed light on the peculiar super-solar iron abundances implied in the reflection fitting of 4U 1702−429. The current version of RELXILLD that allows for variable disk density has a fixed cutoff energy of 300 keV.

4U 1746−371 did not show a clear signature of reflection in its spectrum. The low cutoff energy is consistent with cutoff energies seen in other NS LMXBs in intermediate states (4U 1636−536, 4U 1705−44, 4U 1728−34, 4U 1734−44, and 4U 1820−30: Church et al. 2014) and an *INTEGRAL* study of this source by Balman (2009). Although, we find a hotter blackbody component and harder spectral index in comparison to Balman (2009). The spectral index is closer to the value of $\Gamma = 1.20 \pm 0.27$ found in Church et al. (2001). Additionally, we model the continuum emission with a Comptonized accretion disk component. The optically thick Comptonized component ($\tau \sim 6$) and low electron temperature (~ 3 keV) of 4U 1746−371 is akin to GX 13+1 (Iaria et al. 2014; D'Aì et al. 2014), which is another highly-inclined "soft" atoll. In contrast to 4U 1746−371, GX 13+1 continuously shows a broad Fe line component and narrow Fe absorption features indicative of winds (Díaz Trigo et al., 2012). This could be due to the fact that Fe line flux is correlated with continuum flux (Lin et al, 2010) and GX 13+1 is more than six times as luminous (D'Aì et al., 2014). A simple Gaussian at 6.4 keV to account for a potential Fe line component in 4U 1746−371 gave an equivalent width of ~ 30 eV, which is about $1/6^{\rm th}$ of the value reported in Díaz Trigo et al. (2006). However, the observation reported in Díaz Trigo et al. (2006) occurred when the source was a factor of four times more luminous. The discrepancy in the equivalent width of the Fe line component is likely the result of a change in ionization state, though we were unable to place any meaningful constraints on the

ionization parameter with RELXILL or RELXILLCP.

Another source was recently found to not have reflection features present in its persistent spectrum: the Z source GX 5−1 (Homan et al., 2018). The likeliest explanation for the absence of reflection features was a highly ionized disk given the sources high luminosity ($L_{1-100\ keV} = 2.97 \times 10^{38} - 4.27 \times 10^{38}$ ergs s^{-1}). A highly ionized accretion disk could explain the lack of reflection in 4U 1746−371, but the source is not nearly as luminous as GX 5−1. 4U 1746−371 was at 0.02 L_{Edd} at the time of the *NuSTAR* observation, whereas GX 5−1 spanned the range of $\sim 0.76 - 1.14$ L_{Edd}. Since 4U 1746−371 is a known dipping source, it is more likely that the combination of source geometry and Comptonization in the accretion disk corona scatters reflected photons out of the line of sight vastly reducing the number of line contributing photons (Petrucci et al., 2001). This is further supported by the high optical depth ($\tau \sim 6$) from the Comptonization fit in addition to the dipping nature of the source. Note that this is not the case for GX 3+1 since the source is at a lower inclination and we are not looking through the Comptonizing corona on top of the accretion disk. However, this could also explain the lack of a reflection spectrum in the "soft" state for GS 1826−24, which presents evidence of being highly inclined and Comptonized as well (Chenevez et al., 2016).

For the three sources in which reflection was detected, the brightest of the sources is truncated prior to the ISCO whereas the lower Eddington luminosities have inner disk radii nearly consistent with the ISCO, within errors. We are able to place these three sources into the larger sample sof NSs (with $B < 10^{10}$ G) that have been observed with *NuSTAR* wherein reflection allows limits to be placed on the location of the disk. Table 6.6 and Figure 6.3 are updated from Ludlam et al. (2017a) to incorporate recent analyses and further division into NS sub-classes (persistent atoll and Z sources, transients, and a very faint X-ray binary). The Eddington fraction, which is a proxy for $\dot{m}$, is calculated from the 0.5-50 keV luminosity of each source

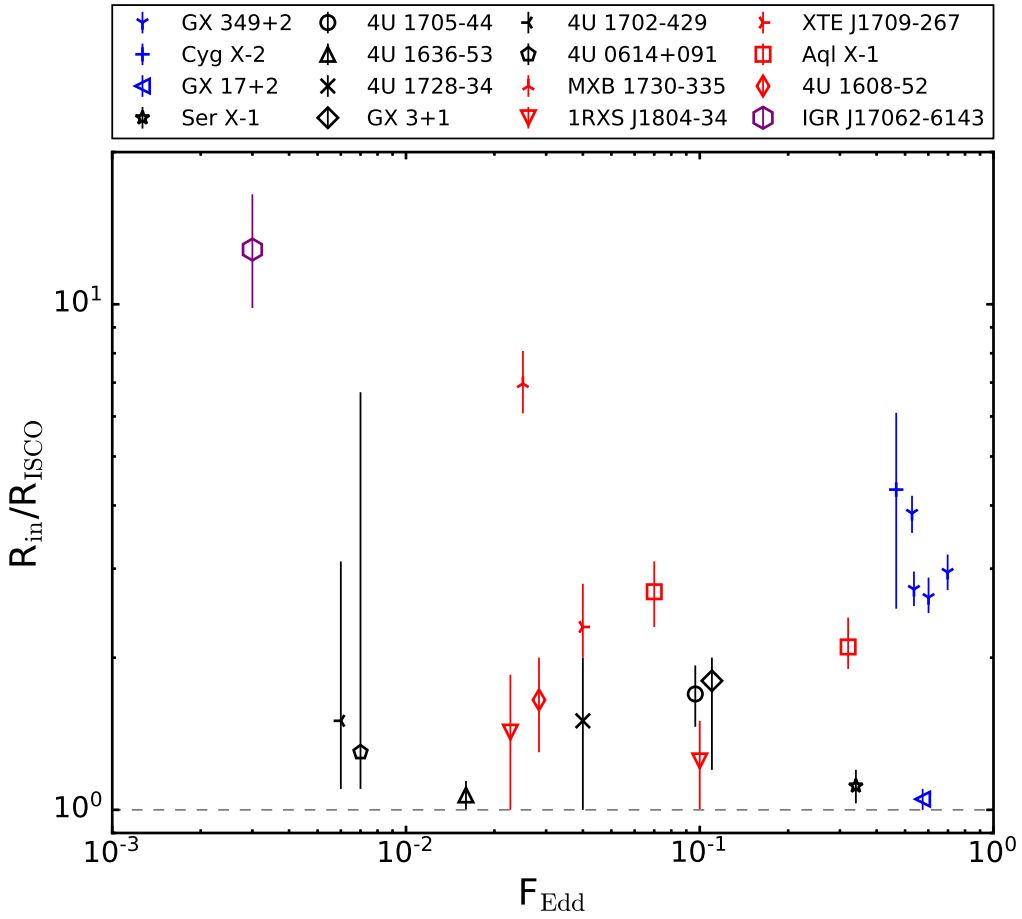

Figure 6.3 Comparison of Eddington fraction and measured inner disk radii for NSs observed with *NuSTAR*. Black points indicate persistent atoll sources, blue points indicate persistent Z sources, red points are transient systems, and the purple point indicates a very faint X-ray binary (VFXB). The dashed grey line denoted the innermost stable circular orbit. See Table 6.6 for inner disk radii and Eddington fractions.

Table 6.6 NS Inner Disk Radii & Eddington Fraction Observed with *NuSTAR*

Source	R_{in} (ISCO)	F_{Edd}	ref.
Atolls			
Ser X-1	$1.03 - 1.20$	0.34	1
	$1.76 - 2.70$	0.34	2
4U 1705−44	$1.46 - 1.93$	0.10	3
4U 1636−53	$1.00 - 1.14$	0.01	3
4U 1728−34	$1.0 - 2.0$	0.04	4
GX 3+1	$1.2 - 2.0$	0.11	...
4U 1702−429	$1.1 - 3.1$	0.006	...
4U 0614+091	$1.1 - 5.7$	0.007	...
Z			
GX 17+2	$1.00 - 1.30$	0.57	3
Cyg X-2	$2.5 - 6.1$	0.47	5
GX 349+2	$2.71 - 2.96$	0.54	6
	$3.53 - 4.18$	0.53	6
	$2.45 - 2.88$	0.60	6
	$2.72 - 3.2$	0.70	6
Transients			
4U 1608−52	$1.3 - 2.0$	0.03	7
1RXS J180408.9-34	$1.00 - 1.85$	0.02	8
	$1.0 - 1.5$	0.10	9
Aquila X-1	$2.3 - 3.1$	0.07	10
	$1.9 - 2.4$	0.23	10
XTE J1709−267	$2.0 - 2.8$	0.04	11
MXB 1730−335	$6.08 - 8.08$	0.025	12
VFXB			
IGR J17062−6143	$9.8 - 16.5$	~ 0.003	13

Note.— (1) Miller et al. 2013; (2) Matranga et al. 2017; (3) Ludlam et al. 2017a; (4) Sleator et al. 2016; (5) Mondal et al. 2018; (6) Coughenour et al. 2018; (7) Degenaar et al. 2015; (8) Ludlam et al. 2016; (9) Degenaar et al. 2016; (10) Ludlam et al. 2017c; (11) Ludlam et al. 2016; (12) van den Eijnden et al. 2017; (13) van den Eijnden et al. 2018.

Table 6.7 Maximum Boundary Layer Extent and Magnetic Field Strength

Source	$R_{\rm BL,\ max}$ (R_g)	$B_{\rm max}$ (10^8 G)
GX 3+1	~ 6.67	≤ 6.7
4U 1702−429	~ 5.35	≤ 3.3
4U 0614+091	~ 5.36	≤ 14.5

Note.— The maximum radial extent of the boundary layer region is calculated based up the maximum luminosity reported in Table 6.2 − 6.4. We assume a canonical NS ($M_{NS} = 1.4\ M_{\odot}$, $R_{NS} = 10$ km). For the estimate of the upper limit on the magnetic field strength at the poles, we use the maximum unabsorbed $0.5 - 50$ keV flux and inner disk radius from the *NuSTAR* fits. Additionally, we assume an angular anisotropy and conversion factor of unity (Cackett et al., 2009). The efficiency of accretion in both calculations is assumed to be 0.2 (Sibgatullin & Sunyaev, 2000).

divided by the empirical Eddington limit of 3.8×10^{38} ergs s^{-1}. The observations of 4U 1702−429 and 4U 0614+091 in this work provide the lowest luminosity disk position measurements for persistent atoll sources observed with *NuSTAR*. In the case of the very faint X-ray binary, IGR J17062−6143 is able to constantly accrete at very low $\dot{m}$ where the disk may enter the radiatively inefficient accretion flow (RIAF) regime (Narayan & Yi 1994; Blandford & Begelman 1999), but truncation by the magnetosphere is not ruled out (van den Eijnden et al., 2018).

It should be noted that the R_{in} estimates for Serpens X-1 by Miller et al. (2013) and Matranga et al. (2017) used the same *NuSTAR* data set, however Matranga et al. (2017) also used *XMM-Newton* observations to construct a broad-band X-ray spectrum. This emphasizes the importance of the lower-energy bandpass in deriving reflection parameters. Hence values in Table 6.6 and Figure 6.3 may be biased since *NuSTAR* only has the high energy coverage. Regardless, the lack of a clear trend between $F_{\rm Edd}$ and R_{in} reaffirms the previously report complex behavior of the disk over various mass accretion rates (Cackett et al. 2010; D'Aì et al. 2010; Ludlam et al. 2017a) and suggests the presence of a boundary layer or the magnetic field of the NS likely plays a role.

In Table 6.7 we provide estimates for the extent of a boundary layer using Equation (25) from Popham & Sunyaev (2001) and upper limits on the magnetic field strength using Equation (1) from Cackett et al. (2009) for these systems. The large upper limit on the magnetic field strength for 4U 0614+091 is driven by the large uncertainty on the inner disk radius. Although we do not detect pulsations during these observations, the sources could still be magnetically accreting. The hot spot could be nearly aligned with the spin axis, in which case pulsations would be undetectable, or the modulated emission could be scattered by the circumstellar gas (Lamb et al., 1985). A comprehensive explanation regarding all the ways pulsations are suppressed or hidden from view in NS LMXBs can be found in Lamb et al. (2009). The extent of the boundary layer regions are too small to account for the disk position, but these values may be underestimated as they do not account for spin and viscous effects in this layer. An additional plausible explanation for disk truncation could be that the innermost region of the accretion disk has given way to a compact Comptonizing coronal region as expected in lower luminosity regimes (Narayan & Yi 1994; Done et al. 2007; Veledina, Poutanen, & Vurm 2013). We are unable to determine the exact truncation mechanism from a single observation. This is because the position of the disk as a function of $\dot{m}$ changes in opposing manners for truncation by the magnetosphere (Ibragimov & Poutanen, 2009) or a boundary layer extending from the NS surface (Popham & Sunyaev, 2001). Multiple observations over significant changes in mass accretion rate within individual sources are needed to determine the definitive truncation mechanism for a system.

6.7 Summary

We present a spectral analysis of four persistent atoll sources observed with *NuSTAR* to investigate the location of the inner disk measured via reflection fitting techniques within these relatively low luminosity systems. We detect the presence of

reflection firmly in three out of four of these sources (GX 3+1, 4U 1702−429, and 4U 0614+091). Reflection features were not detected in 4U 1746−371 likely due to a combination of source geometry and strong Comptonization. These sources span a range in Eddington fraction of $0.006 - 0.11$, providing the lowest F_{Edd} disk position measurement for an atoll source observed with *NuSTAR*, and increase the number of sources with detected reflection features by $\sim 20\%$ for the *NuSTAR* sample. Adding these sources to the existing sample of NSs with inner radius measurements reaffirms the lack of a clear one-to-one trend between the position of the inner disk and mass accretion rate as observed with other X-ray missions such as *XMM-Newton* and *Suzaku* (e.g., Cackett et al. 2010; D'Aì et al. 2010; Chiang et al. 2016b). This emphasizes the need to shift focus to investigate the truncation mechanisms in individual sources to determine the dynamical role of the boundary layer or magnetosphere. In order to disentangle these different scenarios of disk truncation, multiple observations of a source over a large range in mass accretion rate are necessary.

6.8 Appendix

Spectral fitting with relxillcp

Here we provide the reader with the results from using the model RELXILLCP on GX 3+1 and 4U 1702−429. This model produces reflection from the reprocessing of photons from a Comptonized disk component with a hard-coded seed photon temperature of 0.05 keV. Table 6.8 provides the parameter values that can be compared to the resulting fits in Tables 6.2 and 6.3 for GX 3+1 and 4U 1702−429, respectively. Figure 6.4 is given to provide a direct comparison to the fits presented in Figure 6.2. These fits do not provide an improvement in the overall fit of the spectra from the results presented in §6.5.1 and §6.5.2. In the case of 4U 1702−429, the comparable fit with high A_{Fe} and ionization still supports the need for higher disk density models.

Table 6.8 Reflection Modeling with RELXILLCP

Model	Parameter	GX 3+1	4U 1702−429
TBABS	N_H (10^{22} cm^{-2})	$2.42^{\dagger}$	$2.32^{\dagger}$
BBODY	kT (keV)	1.40 ± 0.02	...
	norm (10^{-3})	6.8 ± 0.3	...
RELXILLCP	q	3.1 ± 0.3	2.3 ± 0.2
	i (°)	24 ± 1	64 ± 1
	R_{in} ($R_{\rm ISCO}$)	$1.85^{+0.35}_{-0.27}$	$1.00^{+0.4}_{*}$
	R_{in} (R_g)	$10.8^{+2.1}_{-1.6}$	$6.0^{+2.4}_{*}$
	Γ	$1.72^{+0.03}_{-0.01}$	2.00 ± 0.01
	$\log \xi$	$3.30^{+0.01}_{-0.05}$	$4.7^{*}_{-0.1}$
	A_{Fe}	$10^{*}_{-0.2}$	$8.7^{+0.7}_{-0.9}$
	kT (keV)	2.24 ± 0.01	20^{+2}_{-1}
	$f_{\rm refl}$	$0.66^{+0.03}_{-0.07}$	$2.6^{+0.4}_{-0.5}$
	norm (10^{-3})	7.2 ± 0.1	$0.30^{+0.02}_{-0.07}$
	χ^2 (dof)	344.6 (130)	484.9 (382)

† = fixed

Note.— Errors are reported at the 90% confidence level. An asterisk indicates that the parameter is at the hard-coded limit of the model. The outer disk radius was fixed at 990 R_g, the dimensionless spin parameter and redshift were set to zero for the RELXILLCP model. $f_{\rm refl}$ denotes the reflection fraction.

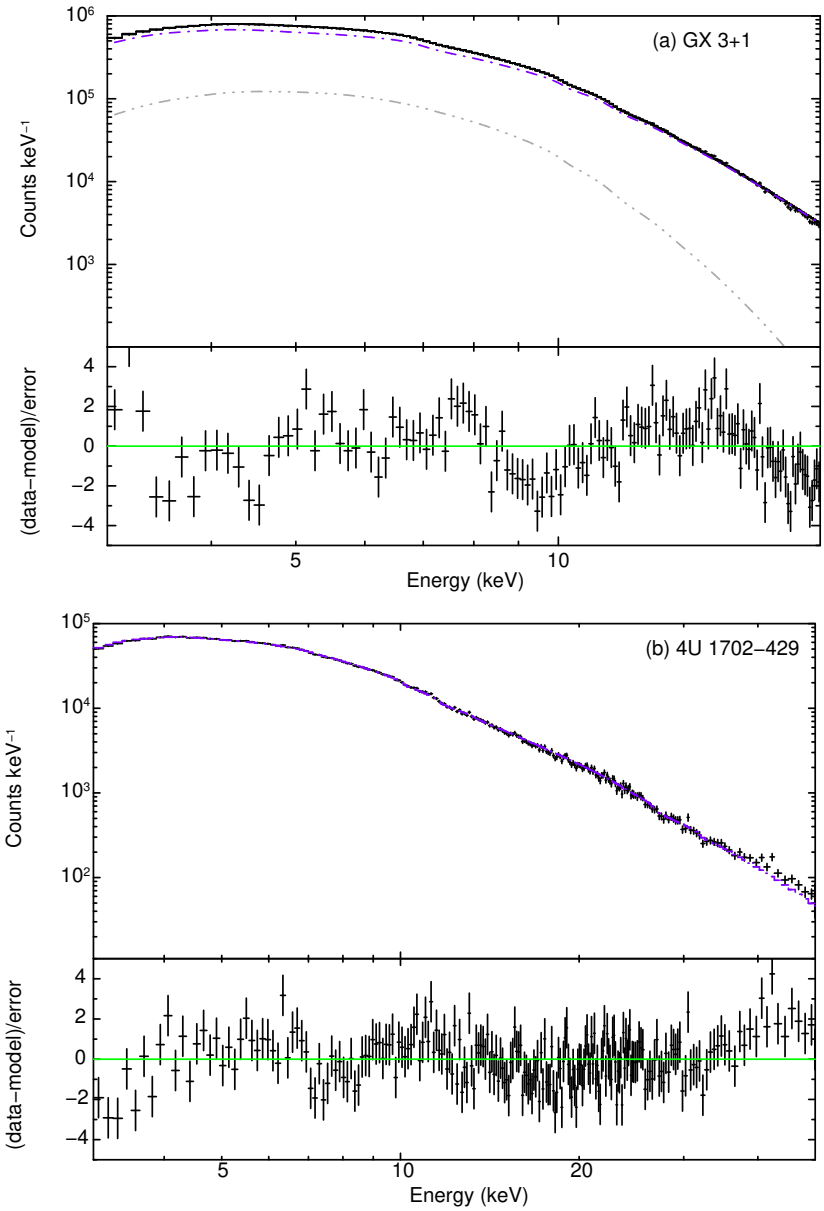

Figure 6.4 *NuSTAR* spectral modeling and residuals divided by errors for (a) GX 3+1 and (b) 4U 1702−429 when fit with RELXILLCP. The purple dot-dashed lines indicates RELXILLCP, which contains both the Comptonized disk component of the continuum and reflection. The grey dot-dot-dot dashed line is a single-temperature blackbody to account for boundary layer emission.

CHAPTER VII

Detection of Reflection Features in the Neutron Star Low-mass X-ray Binary Serpens X-1 with *NICER*

7.1 Preface

This chapter appears in the Astrophysical Journal Letters, Volume 858, Letter 5 (Ludlam et al., 2018) and is co-authored by Jon M. Miller, Zaven Arzoumanian, Peter M. Bult, Edward M. Cackett, Deepto Chakrabarty, Thomas Dauser, Teru Enoto, Andy C. Fabian, Javier A. García, Keith C. Gendreau, Sebastien Guillot, Jeroen Homan, Gaurava K. Jaisawal, Laurens Keek, Beverly La Marr, Christian Malacaria, Craig B. Markwardt, Jack F. Steiner, and Tod E. Strohmayer. The paper is reproduced here under the non-exclusive rights of republication granted by the American Astronomical Society to the authors of the paper.

7.2 Abstract

We present *Neutron Star Interior Composition Explorer* (*NICER*) observations of the neutron star low-mass X-ray binary Serpens X-1 during the early mission phase in 2017. With the high spectral sensitivity and low-energy X-ray passband of *NICER*, we

are able to detect the Fe L line complex in addition to the signature broad, asymmetric Fe K line. We confirm the presence of these lines by comparing the *NICER* data to archival observations with *XMM-Newton*/RGS and *NuSTAR*. Both features originate close to the innermost stable circular orbit (ISCO). When modeling the lines with the relativistic line model RELLINE, we find the Fe L blend requires an inner disk radius of $1.4^{+0.2}_{-0.1}$ $R_{\rm ISCO}$ and Fe K is at $1.03^{+0.13}_{-0.03}$ $R_{\rm ISCO}$ (errors quoted at 90%). This corresponds to a position of $17.3^{+2.5}_{-1.2}$ km and $12.7^{+1.6}_{-0.4}$ km for a canonical neutron star mass ($M_{\rm NS} = 1.4\ M_{\odot}$) and dimensionless spin value of $a = 0$. Additionally, we employ a new version of the RELXILL model tailored for neutron stars and determine that these features arise from a dense disk and supersolar Fe abundance.

7.3 Introduction

In low-mass X-ray binary (LMXB) systems, where the companion star has mass $\leq$ 1 $M_{\odot}$, accretion onto the compact object generally occurs through an accretion disk formed via Roche-lobe overflow. In many instances, these disks are illuminated by hard X-rays coming either from a hot electron corona (Sunyaev et al., 1991) or the surface of the neutron star or boundary layer (where the material from the disk reaches the neutron star; Popham & Sunyaev 2001). The exact location and geometry of the corona is not known, but is considered to be compact and close to the compact object (see Degenaar et al. 2018 for a review and references therein). Regardless of the source of the hard X-rays, the disk reprocesses the illuminating photons and re-emits them in a continuum with a series of atomic features and Compton backscattering hump superimposed, known as the "reflection" spectrum. The most prominent feature that arises as a result of reflection is the Fe K emission line between 6.4–6.97 keV. The entire Fe line profile is shaped by strong Doppler and relativistic effects due to the disk's rotational velocity and proximity to the compact object (Fabian et al., 1989). The extent of the red wing thereby enables important physical insights to be

derived from these systems. Moreover, the blue-shifted emission of the Fe line profile provides an indication of the inclination of the disk due to Doppler effects becoming more prominent with increasing inclination (Dauser et al., 2010). This feature has been reported in both black hole (BH: e.g., Miller 2002) and neutron star (NS: e.g., Bhattacharyya & Strohmayer 2007; Cackett et al. 2008) LMXBs, suggesting similar accretion geometries despite the mass difference of the compact accretor and the presence of a surface.

An additional prominent reflection feature that can arise from the illuminated accretion disk is the lower-energy Fe L line near 1 keV. This feature was first reported in Fabian et al. (2009) for the active galactic nucleus (AGN) 1H0707−495 with the same asymmetric broadening seen in Fe K. Moreover, the ratio of Fe K to Fe L emission was consistent with predictions from atomic physics. This feature was soon discovered in other AGN, such as IRAS 13224−3809 (Ponti et al. 2010), cementing the importance of reflection features in these accreting systems.

The BHs in LMXBs are scaled-down versions of the much more massive accretors in AGN (Miller, 2007). Since accretion in BH and NS LMXBs is similar, we expect to find an Fe L feature in a NS LMXB if the conditions are right. There have been a number of reports of line complexes near ~ 1 keV in NS LMXBs during persistent emission that have been attributed to the Fe L transition, but also K-shell transitions of medium-Z elements (Vrtilek et al. 1988; Kuulkers et al. 1997; Schulz 1999; Sidoli et al. 2001; Cackett et al. 2010). These lines appear to be broadened by the same mechanism as the Fe K component (Ng et al., 2010) and can be modeled as smeared relativistic lines (Iaria et al., 2009).

Serpens X-1 (Ser X-1) is an "atoll" NS LMXB located at a distance of 7.7 ± 0.9 kpc (Galloway et al., 2008). Optical spectroscopy and some X-ray reflection studies indicate that the system has a low binary inclination ($i \leq 10°$, Cornelisse et al. 2013; Miller et al. 2013), though higher inclinations have been reported from other X-ray

reflection studies ($25^\circ < i < 50^\circ$, Cackett et al. 2008, 2010; Chiang et al. 2016a; Matranga et al. 2017). The low amount of absorbing material in the direction of Ser X-1, as demonstrated by the low neutral hydrogen column density ($N_H = 4 \times 10^{21}$ cm^{-2}, Dickey & Lockman 1990), provides an opportunity to detect multiple reflection features.

With the recent launch of the *Neutron Star Interior Composition Explorer* (*NICER*; Gendreau et al. 2012), we now have the opportunity to test reflection predictions and probe the innermost region of the accretion disk in Ser X-1. *NICER* was installed on the International Space Station in 2017 June. The payload comprises 56 "concentrator" optics that each focus X-rays in the 0.2–12 keV range onto a paired silicon drift detector. Prelaunch testing left 52 functioning detectors providing a total collecting area of 1900 cm^2 at 1.5 keV with which to search for low-energy reflection features.

7.4 Observations and Data Reduction

The following subsections detail the reduction of Ser X-1 observations obtained with *NICER*, *NuSTAR*, and *XMM-Newton*. The *NuSTAR* and *XMM-Newton* data were not acquired contemporaneously with our *NICER* observations, but are used as a baseline for determining which features are astrophysical in the *NICER* data, since Ser X-1 has remained roughly steady in its persistent emission (0.2–0.3 Crab) in the *Swift*/BAT and MAXI wide-field monitors for the past decade.

7.4.1 NICER

NICER observed Ser X-1 thirteen times between 2017 July and 2017 November (ObsIDs 1050320101–1050320113) for a cumulative exposure of 39.9 ks on target. The data were reduced using NICERDAS version 2018-02-22_V002d. Good time intervals (GTIs) were created using NIMAKETIME selecting COR_SAX$\geq$4, to remove high particle radiation intervals associated with the Earth's auroral zones, and separating

orbit day (SUNSHINE==1) from orbit night (SUNSHINE==0) in addition to the standard *NICER* filtering criteria. Moreover, we only selected events that occurred when the angle between the Sun and target of observation were $\geq 90^{\circ}$. These GTIs were applied to the data via NIEXTRACT-EVENTS selecting events with PI channel between 25 and 1200 (0.25–12.0 keV) that triggered the detector readout system's slow and, optionally, fast signal chains. Background spectra were created from data acquired from one of seven "blank sky" targets based on RXTE background fields (Jahoda et al., 2006). We reduced all observations of the background fields as described above. Ser X-1 is much brighter (1597 counts s^{-1}) in comparison to the background fields ($\sim 0.7 - 2.3$ counts s^{-1}). We proceeded with using RXTE background field 5 throughout the remaining analysis since the results are not dependent upon this choice.

The resulting event files were read into XSELECT and combined to create light-curves and time-averaged spectra for orbit day and orbit night. There were no Type-I X-ray bursts present in the light-curves during the GTIs so no additional filtering was needed. The spectra suffered from instrumental residuals given the preliminary calibration at this stage. In order to mitigate these residuals we normalized the data to *NICER* observations of the Crab Nebula, which has a featureless absorbed power-law spectrum in the energy range of interest (see, e.g., Weisskopf et al. 2010).

We use ObsIDs 1011010101, 1011010201, and 1013010101-1013010123 for the Crab, and the same data reduction procedure as above. The resulting exposure time for the Crab is ~ 1.1 ks for orbit day and ~ 21.2 ks for orbit night. The time-averaged Crab spectrum was fit with an absorbed power-law model from 0.25–10 keV to determine the absorption column along the line of sight. The absorption column was consistent with the Dickey & Lockman (1990) value at $N_H \sim 3.8 \times 10^{21}$ cm^{-2}. We then froze the absorption column and fit the 3–10 keV subset of the spectrum to prevent instrumental features at low energies from skewing the fit. This returned a

photon index of $\Gamma \sim 2.0$[1]. We extrapolated the fit back down to 0.25 keV and created a fake spectrum using the 'fakeit' command within the XSPEC software package (Arnaud, 1996) for the same exposure time as the actual Crab data. We used the FTOOL MATHPHA to divide the Crab spectrum by the simulated Crab data. This yielded a spectrum with just the instrumental residuals. We then used MATHPHA to divide the Ser X-1 count rate spectrum by the instrumental residual spectrum. The normalized spectra after applying all of our filtering criteria for orbit night and day have exposures of ~ 4.5 ks and ~ 4.7 ks, respectively. However, since the exposure time for the Crab during orbit day was much smaller in comparison to orbit night, it introduced noise into the Ser X-1 spectrum when normalizing. We therefore only focused on the data that was accumulated during orbit night. See Figure 7.1 for a comparison of the Ser X-1 data before and after normalizing to the Crab. The source spectrum was grouped via GRPPHA to have a minimum of 25 counts per bin.

7.4.2 NuSTAR

Two observations of Ser X-1 were taken with *NuSTAR* on 2013 July 12 and 13 (ObsIDs 30001013002 and 30001013004) for ~ 30.5 ks. These observations have been previously reported by Miller et al. (2013) and Matranga et al. (2017). There were no Type-I X-ray bursts that occurred during the 2013 observations. Using the NUPRODUCTS tool from NUSTARDAS v1.8.0 with CALDB 20180126, we created light-curves and spectra for the 2013 observations with STATUSEXPR="STATUS==b0000xxx00xxxx000" to correct for high count rates. We used a circular extraction region with a radius of 100″ centered around the source to produce a source spectrum for both the FPMA and FPMB. We used another 100″ radial region away from the source for the purpose of background subtraction. Following Miller et al. (2013), we respectively combined the two source spectra, background spectra, ancillary response matrices and redis-

[1]We verified that the choice of background did not change the photon index by performing fits with each field. The photon index changes by no more than $\Delta\Gamma = 0.005$.

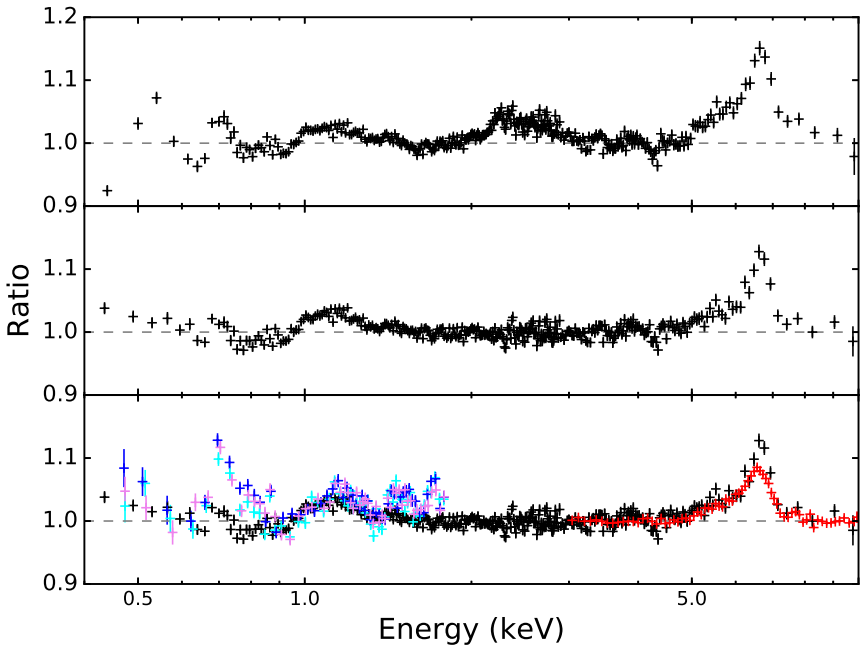

Figure 7.1 *Top:* Ratio of *NICER* data to continuum before normalizing to the Crab. Instrumental residuals can be seen at ~ 0.5 keV, ~ 1.8 keV, and ~ 2.2 keV due to O, Si, and Au, respectively. The feature at ~ 0.7 keV has instrumental origin as well, likely due to gain offsets as the response changes rapidly in this area. *Middle:* Ratio of *NICER* data to continuum after normalizing to the Crab to mitigate instrumental residuals. Emission features are still present near 1.1 keV and 6.7 keV. *Bottom:* Ratio of the data to continuum model for *NICER* (black), *NuSTAR* (red), and *XMM-Newton*/RGS (blue, cyan, purple) observations. The data were fit with the combination of an absorbed single-temperature blackbody, multi-temperature blackbody, and power-law. The $0.9-1.3$ keV and $5.0-8.0$ keV energy bands were ignored while fitting to prevent the lines from skewing the continuum. Continuum parameters were tied between *NICER* and *NuSTAR* while normalization components were allowed to vary. The *XMM-Newton* data were left free with a constant allowed to float between observations. Data were rebinned for clarity.

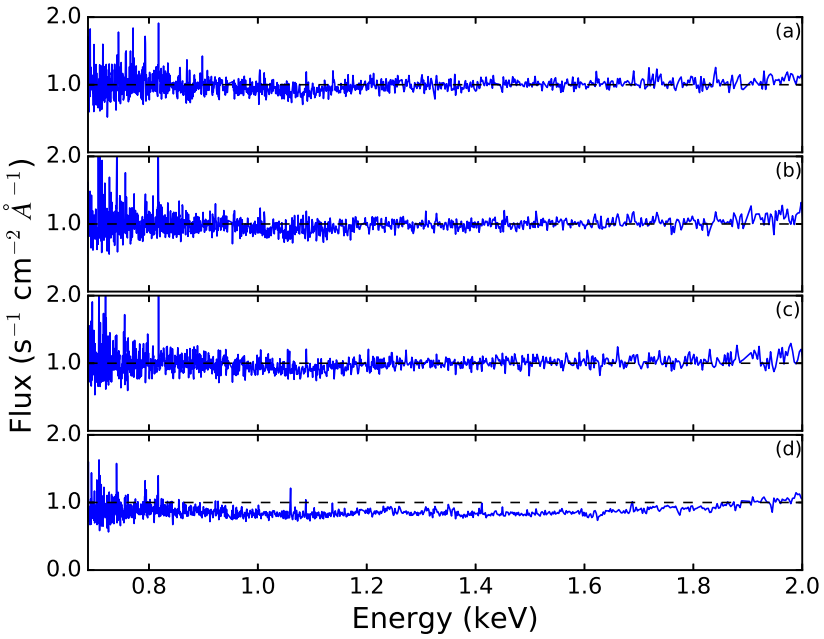

Figure 7.2 Ratio of RGS first to second order fluxed spectra for the three *XMM-Newton* observations: (a) 0084020401, (b) 0084020501, and (c) 0084020601. The bottom panel denoted (d) shows an observation of GRO J1655-40 that is piled-up. The ratio is roughly consistent with unity in panels (a)-(c) indicating that pile-up in the RGS band is not an issue for Serpens X-1.

tribution matrix files via ADDASCASPEC and ADDRMF, weighting by exposure time. The combined spectra were grouped to have a minimum of 100 counts per bin using GRPPHA.

7.4.3 XMM-Newton

There are three observations of Ser X-1 with *XMM-Newton* (ObsIDs 0084020401, 0084020501, and 0084020601) performed in 2004 March for a total exposure of $\sim$ 65.7 ks. These observations were reported in Bhattacharyya & Strohmayer (2007), Cackett et al. (2010), and Matranga et al. (2017). We focus on the Reflection Grating Spectrometer (RGS) data because we are interested in the high-resolution, low-energy spectral features. The data were reduced using the command RGSPROC in SAS v16.1.

We checked that the data do not suffer from pile-up by inspecting the ratio of the first and second order fluxed spectra[2] (see Figure 7.2). Each ratio for Ser X-1 is consistent with unity across nearly all of the RGS energy band indicating that pile-up is not an issue. For comparison, we plot the ratio of the fluxed spectra for the stellar mass black hole X-ray binary GRO J1655-40, which suffered from pile-up in the RGS instrument, in the bottom panel. Since the observations of Ser X-1 were not piled-up, the first order RGS1 and RGS2 data were combined via RGSCOMBINE for each respective observation. The resulting spectra were then grouped using GRPPHA to have a minimum of 25 counts per bin.

7.5 Spectral Analysis and Results

We use XSPEC version 12.9.1m and report uncertainties at the 90% confidence level. Since the *XMM-Newton* and *NuSTAR* data have been previously analyzed and published elsewhere, we choose to mainly focus on the *NICER* results. We model the *NICER* data in the $0.4 - 10.0$ keV energy band, outside of which the effective area drops sharply. We model the absorption along the line of sight using TBNEW[3] with VERN cross sections (Verner et al., 1996) and WILM abundances (Wilms et al., 2000). We allow the neutral hydrogen absorption, as well as the oxygen and iron absorption abundances, to be free parameters to ensure that edges in the region of interest are properly modeled. Allowing the oxygen and iron absorption to deviate from solar abundance provides a statistical improvement in the following fits at more than 9σ confidence level in each case, although these could be instrumental in origin as the O K edge lines up with changes in the effective area of the detector and may not reflect actual ISM abundance measurements. We find a neutral absorption column of $N_H \sim 7 \times 10^{21}$ cm^{-2}, which is higher than the Dickey & Lockman (1990) value

[2]XMM-Newton Users Handbook §3.4.4.8.3

[3]http://pulsar.sternwarte.uni-erlangen.de/wilms/research/tbabs/

of 4×10^{21} cm^{-2}, but consistent with other values reported when fitting low-energy X-ray data from *Chandra* and *XMM-Newton* (Chiang et al. 2016a; Matranga et al. 2017).

We apply the double thermal-continuum model for atoll sources in the soft state to the *NICER* data. This model consists of a multi-temperature blackbody component (DISKBB) to model the disk emission and a single temperature blackbody component (BBODY) to model emission originating from the surface of the neutron star or boundary layer. This provides a poor fit, with $\chi^2/d.o.f. = 1891.91/952$. We proceed with adding a power-law component, which is sometimes needed in the soft state (Lin et al., 2007) and has previously been reported for Ser X-1 (Miller et al. 2013; Chiang et al. 2016a). The power-law component produced a photon index of $\Gamma = 2.88 \pm 0.25$ and normalization of 0.69 ± 0.08 photons keV^{-1} cm^{-2} s^{-1} at 1 keV. The overall fit improves by 10σ ($\chi^2/d.o.f. = 1671.33/950$) although it is still poor due to the presence of emission features. The disk component yielded a temperature of 1.07 ± 0.03 keV and normalization of 154 ± 17 km^2/ (D/10 kpc)^2 cos(i). The single-temperature blackbody emerged with a temperature of 1.75 ± 0.03 keV and normalization $K = 5.5 \pm 0.02 \times 10^{-2}$. Replacing the single temperature blackbody component for thermal Comptonization (NTHCOMP) did not improve the fit ($\chi^2/d.o.f. = 1862.39/949$).

There are two strong emission features near 1.1 and 6.7 keV that can be attributed to a blend of Fe L and Fe K shell emission (see Figure 7.1). As a consistency check, we overplot the *NuSTAR* and *XMM-Newton* ratio-to-continuum spectra in the lower panel of Figure 7.1. The presence of these features in other detectors verifies that they are not due to the *NICER* instrumentation. We initially apply Gaussian profiles to each feature, which improves the fit by $\Delta\chi^2 = 290$ for six degrees of freedom. The low-energy emission feature has a line centroid energy of 1.12 ± 0.01 keV with width $\sigma = 0.10^{+0.02}_{-0.01}$ keV and normalization of $9.8 \pm 0.2 \times 10^{-3}$ photons cm^{-2} s^{-1}, which

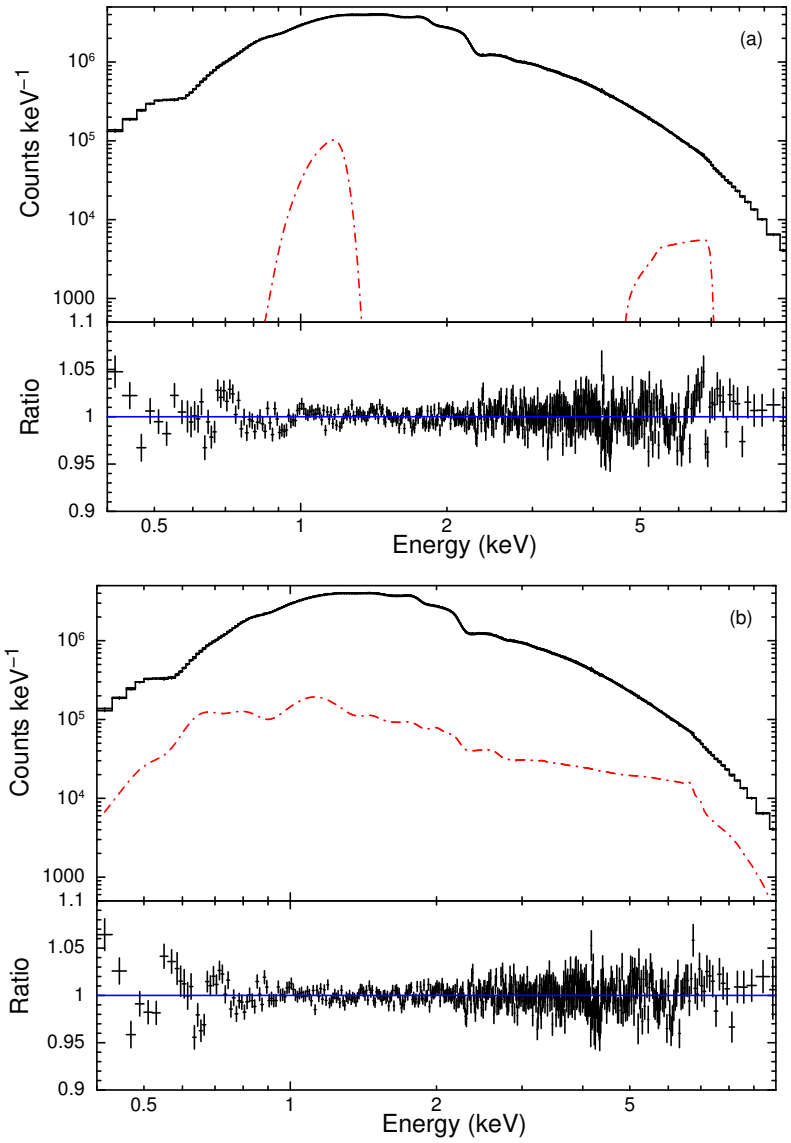

Figure 7.3 Spectra of Serpens X-1 with reflection modeled using RELLINE (a) to account for the Fe L and K lines individually and RELXILLNS (b) to account for entire reflection spectrum indicated by the red dot-dashed lines. The lower panels indicate the ratio of the *NICER* data to overall model. The continuum is modeled with an absorbed disk blackbody, single temperature blackbody, and power-law component. For plotting purposes, the data were rebinned

is similar to the values reported in Cackett et al. (2010) for the *XMM-Newton*/PN data. We again checked that the low-energy feature is not an instrumental artifact by fixing the width of the line to 0, which is a delta function in XSPEC and indicates the resolution of the detector. We find that a line width of zero is ruled out at 9σ, corroborating that the line is not native to the instrumentation. The Fe K emission feature has a line centroid energy of 6.59 ± 0.04 keV with width $\sigma = 0.26^{+0.06}_{-0.05}$ keV and normalization of $3.8 \pm 0.1 \times 10^{-3}$ photons cm^{-2} s^{-1}. The equivalent widths of the Fe K and Fe L lines are 0.064 ± 0.002 keV and 0.0090 ± 0.0001 keV, respectively. The equivalent width of the Fe K line is comparable to values reported in Cackett et al. (2010) for *XMM-Newton* and *Suzaku* observations of other NS LMXBs, whereas the Fe L blend agrees with Vrtilek et al. (1988).

As a further refinement, we replace the Gaussian line components with the relativistic reflection line model RELLINE (Dauser et al., 2010). We fixed the spin parameter, $a = cJ/GM^2$, to $a = 0$ since most NS in LMXBs have $a \leq 0.3$ (Galloway et al. 2008; Miller et al. 2011). The choice of spin does not have a strong impact on our results; the difference in position of the $R_{\rm ISCO}$ between $a = 0.0$ and $a = 0.3$ is less than 1 R_g (where $R_g = GM/c^2$). We allowed the inner disk radii to be independent for each line component but tied the inclination and emissivity index between the lines. The outer disk radius was fixed to 990 R_g in each case. The double relativistic reflection provides a 10σ improvement in the overall fit, although a Gaussian line cannot be statistically ruled out for the Fe L complex. We find R_{in} of $1.4^{+0.2}_{-0.1}$ $R_{\rm ISCO}$ for Fe L and $1.03^{+0.13}_{-0.03}$ $R_{\rm ISCO}$ for Fe K. Additionally, the inclination of $10.1^{+4.9}_{-0.2}$ degrees from these lines agrees with the early *NuSTAR* results (Miller et al., 2013) and optical spectroscopy (Cornelisse et al., 2013). Table 7.1 reports the values of all free parameters. Figure 7.3(a) shows the ratio of the data to the overall fit as well as the RELLINE model components. The increase in line energy for the Fe L feature is due to the RELLINE model interpreting the feature as a single line rather than a

Table 7.1 Reflection Modeling of Ser X-1

Model	Parameter	RELLINE	RELXILLNS
TBNEW	N_H (10^{21} cm^{-2})	6.9 ± 0.1	6.38 ± 0.02
	A_O	1.10 ± 0.01	$1.25^{+0.02}_{-0.05}$
	A_{Fe}	$1.12^{+0.09}_{-0.02}$	$0.88^{+0.09}_{-0.04}$
DISKBB	kT (keV)	$1.13^{+0.03}_{-0.02}$	$1.15^{+0.05}_{-0.02}$
	norm	130^{+10}_{-20}	120^{+3}_{-10}
BBODY	kT (keV)	1.80 ± 0.02	$1.85^{+0.11}_{-0.03}$
	K (10^{-2})	4.9 ± 0.2	$3.1^{+0.6}_{-0.4}$
POWERLAW	Γ	2.5 ± 0.1	$1.8^{+0.5}_{-0.1}$
	norm (10^{-1})	$5.0^{+0.7}_{-0.4}$	3.50 ± 0.04
RELLINE_1	LineE (keV)	$6.96^{+0.01}_{-0.07}$	...
	q	$3.00^{+0.08}_{-0.16}$	...
	i (°)	$10.1^{+4.9}_{-0.2}$	...
	R_{in} ($R_{\rm ISCO}$)	$1.03^{+0.13}_{-0.03}$	...
	R_{in} (R_g)	$6.2^{+0.8}_{-0.2}$	...
	R_{in} (km)	$12.7^{+1.6}_{-0.4}$	...
	norm (10^{-3})	$7.1^{+0.9}_{-1.0}$	...
RELLINE_2	LineE (keV)	$1.22^{+0.01}_{-0.02}$	...
	R_{in} ($R_{\rm ISCO}$)	$1.4^{+0.2}_{-0.1}$	...
	R_{in} (R_g)	$8.4^{+1.2}_{-0.6}$	...
	R_{in} (km)	$17.3^{+2.5}_{-1.2}$	...
	norm (10^{-3})	$6.8^{+1.2}_{-0.7}$	...
RELXILLNS	q	...	$2.51^{+0.04}_{-0.17}$
	i (°)	...	$4.43^{+0.01}_{-0.30}$
	R_{in} ($R_{\rm ISCO}$)	...	$1.18^{+0.10}_{-0.02}$
	R_{in} (R_g)	...	$7.08^{+0.60}_{-0.12}$
	R_{in} (km)	...	$14.6^{+1.2}_{-0.3}$
	$\log \xi$	...	3.2 ± 0.1
	A_{Fe}	...	$4.8^{+0.8}_{-0.3}$
	$\log N$ (cm^{-3})	...	18.83 ± 0.04
	$f_{\rm refl}$ (10^{-1})	...	$5.4^{+0.3}_{-0.7}$
	norm (10^{-3})	...	1.4 ± 0.3
	$F_{\rm unabs}$	10 ± 3	9 ± 3
	χ^2 (d.o.f.)	1232.9 (942)	1180.4 (942)

Note.— Errors are reported at the 90% confidence level and calculated from Markov chain Monte Carlo (MCMC) of chain length 500,000. The emissivity index q and inclination i were tied between RELLINE components, and the line emission is assumed to be isotropic. The outer disk radius was fixed at 990 R_g, the dimensionless spin parameter and redshift were set to zero for both the RELLINE and RELXILLNS models. The temperature of the blackbody in the RELXILLNS model was linked to the single temperature blackbody of the continuum. The RELXILLNS model was set to reflection only and $f_{\rm refl}$ denotes the reflection fraction. The unabsorbed flux is taken in the $0.4 - 10.0$ keV band and given in units of 10^{-9} ergs cm^{-2} s^{-1}. For reference, for $a = 0$ and canonical NS mass $M_{\rm NS} = 1.4\ M_\odot$, 1 $R_{\rm ISCO} = 6\ R_g = 12.4$ km.

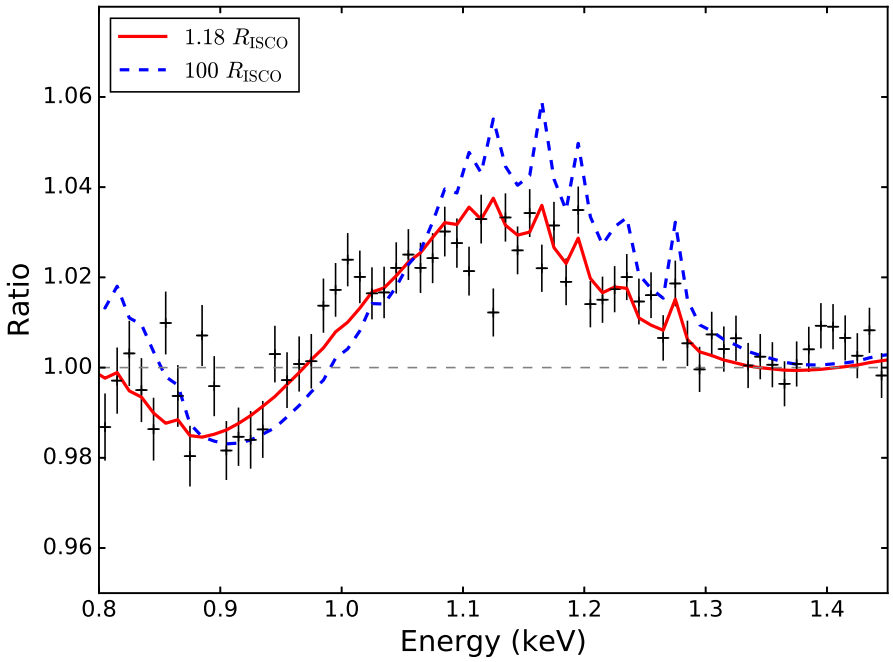

Figure 7.4 Best-fit reflection model reported in Table 7.1 at 1.18 $R_{\rm ISCO}$ (red) and contrasting 100 $R_{\rm ISCO}$ (blue) overlaid on the *NICER* data to highlight the broad Fe L shell blend between 0.9 and 1.3 keV. The larger inner disk radius relaxes the relativistic effects to show the narrow emission lines in that region, likely due to Mg III-VII. The data were rebinned for clarity.

complex of lines between 0.9 to 1.3 keV. There are still residuals in the $6-7$ keV energy band suggesting that RELLINE is unable to fully account for the Fe K line, hence we proceed with applying a self-consistent reflection model.

To obtain a more physical description of these features, we employ a preliminary version of the fully self-consistent reflection model, RELXILLNS, which computes illumination of the disk by a blackbody spectrum (rather than the power-law input of the original RELXILL model, García et al. 2014). The model allows for the input blackbody temperature kT_{bb}, log of the ionization parameter $\log \xi$, iron abundance A_{Fe}, and log of the density of the disk $\log(N\ [\mathrm{cm}^{-3}])$. All other elements are hard-coded to solar abundance. In order for the model to pick up both the Fe L blend and Fe K line, the disk requires a high density and ~ 5 times solar iron abundance

(see García et al. 2016 and Ludlam et al. 2017a for discussion of disk density and iron abundance). This fit is reported in Table 7.1. Figure 7.3(b) shows the ratio of the data to the model as well as the reflection component. In Figure 7.4 we plot the reflection model in the region of the low-energy feature to demonstrate the blending of the Fe L shell transitions. In order to illustrate the local-frame emission spectrum, which better shows the line complex features, we set R_{in} to 100 $R_{\rm ISCO}$, a value so large as to effectively remove relativistic distortions. The narrow emission lines in the same region as the broad Fe L shell are likely due to a lower-Z element such as Mg III–VII.

The single inner disk radius inferred from the RELXILLNS fit falls between the radii obtained from the Fe K line and Fe L blend in the RELLINE fit. This could be due to the model applying the same physical conditions to each line when they could be arising from different locations and/or ionizations within the disk. We currently lack the data quality needed for a double RELXILLNS fit to explore multiple ionization zones.

7.6 Discussion

Through the sensitivity and passband of *NICER* we detected a broad Fe L blend and Fe K in the persistent emission of Ser X-1. We confirm that these lines are not native to *NICER* instrumentation by comparing the spectra to observations made by *NuSTAR* and *XMM-Newton*/RGS. *NICER* captures $\sim 1.34 \times 10^6$ photons in the Fe L band and $\sim 2.75 \times 10^5$ photons in the Fe K band in just 4.5 ks. These lower-energy Fe L lines have the potential to improve the statistical power of disk reflection and, ultimately, can be a very important tool for placing constraining upper limits on the radii of neutron stars if the lines indeed arise from the innermost regions of accretion disks. The position of the inner disk radius inferred from the Fe L blend ($1.4^{+0.2}_{-0.1}$ $R_{\rm ISCO}$) is consistent with the value inferred from the Fe K line ($1.03^{+0.13}_{-0.03}$ $R_{\rm ISCO}$)

within the joint 3σ uncertainties. This is similar to the inner disk radius implied by the DISKBB normalization of the best fit model ($\sim 21 - 28$ km) for an inclination of 10°, distance of 7.7 ± 0.9 kpc (Galloway et al., 2008), and color correction factor of 1.7 (Kubota et al., 1998). Our results for the position of the inner disk agree with previous spectral studies that utilize data from different observatories, such as *Suzaku*, *Chandra*, *XMM-Newton*, and *NuSTAR* (Bhattacharyya & Strohmayer 2007; Cackett et al. 2008, 2010; Chiang et al. 2016a; Miller et al. 2013).

Furthermore, we demonstrate that both the low-energy blend and Fe K line can be modeled with self-consistent reflection, but we are at the limits of the current data set. As the mission progresses and calibration is improved, we will gain a larger sample of data from which we can explore a double RELXILLNS model to determine the locations of these features individually and potentially explore the ionization structure of the disk (Ludlam et al., 2016). In a forthcoming paper, a final version of RELXILLNS will be described and applied to a larger set of *NICER* data, with the goal of further enhancing our understanding of the innermost disk around neutron stars.

CHAPTER VIII

Concluding Remarks and Future Work

This collection of work demonstrates the importance of reflection studies to further our understanding of NSs and accretion. Through targeting NS LMXBs with low-magnetic field strength ($B < 10^{10}$ G), I explored the interplay between the accretion disk and the surface of the NS. With this goal in mind, I investigated reflection features in both persistently accreting and transient NS systems in order to determine the behavior of the accretion disk over a large range of $\dot{m}$. *NuSTAR* provides the advantage of a broad, continuous bandpass ($3-79$ keV) that enables better characterization of the direct continuum and spectroscopy that is not complicated by photon pile-up. With the addition of *NICER*, the bandpass below 3 keV is accessible to detect lower energy features that are also free from pile-up effects. By cross-checking these features with the *XMM-Newton*/RGS, which is sensitive in a limited energy band from $0.45 - 2.1$ keV, I am able to corroborate that lines detected by *NICER* are astrophysical and not instrumental. Thus, the combined bandpass and sensitivity of both *NuSTAR* and *NICER* opens a new opportunity to capture multiple emission features arising from bright sources to map out different observables within the disk and disentangle truncation mechanisms in NS LMXBs.

8.1 Inner Disk Radius as a Function of Mass Accretion Rate

As mentioned in Chapters 3 and 6, it is expected that R_{in} is set, at least partly, by the $\dot{m}$ through the disk. There are several mechanisms that might truncate the inner accretion disk around a NS (e.g., magnetosphere or boundary layer), but these truncation mechanisms generally become more effective at lower $\dot{m}$. In order to determine how R_{in} depends on $\dot{m}$, I compared the NS LMXBs that have been reported to exhibit reflection features with *NuSTAR* within the available literature. For consistency, I carefully replicated the models considered in prior work within the X-ray spectral fitting package XSPEC and extrapolated the models to a common energy range ($0.5-50$ keV). I then used the maximum distance to each source to convert unabsorbed fluxes to luminosities, and divided by the empirical Eddington limit of 3.8×10^{38} erg s^{-1} as per Kuulkers et al. (2003) to obtain the Eddington fraction ($F_{\rm Edd}$: a proxy for $\dot{m}$).

Figure 6.3 plots the inner disk radius (normalized to the innermost stable circular orbit, $R_{\rm ISCO}$) versus $F_{\rm Edd}$ for a set of *sixteen* NSs observed with *NuSTAR* across more than two orders of magnitude in $F_{\rm Edd}$, implying an equivalent range in mass accretion rate (if the efficiency is independent). The inner disk appears to be able to remain very close to $R_{\rm ISCO}$ over this large range in $\dot{m}$ (Spearman rank correlation of $C \sim 0.2$). This work confirmed and extended previous results from that looked at the dependence of R_{in} on $\dot{m}$ with *XMM-Newton* and *Suzaku* (Cackett et al. 2010; Chiang et al. 2016b).

Moving forward, the focus needs to shift towards the behavior of R_{in} over $\dot{m}$ within individual systems in order to determine truncation mechanisms. The behavior of R_{in} with $\dot{m}$ can be used to determine the truncation mechanism in a system when the disk does not extend to $R_{\rm ISCO}$. Observations show that the disk recedes at an Eddington fraction of $\rm F_{Edd} \leq 10^{-3}$ due to the disk entering the ADAF regime (Tomsick et al., 2009). This leaves the magnetosphere of the NS or the boundary layer as the most likely explanations for disk truncation above this threshold. If R_{in} is set by the

magnetosphere, then the inner disk radius will decrease with increasing $\dot{m}$ (Eqn 5.1). On the other hand, if it is set by the boundary layer, then R_{in} is expected to get larger with increasing $\dot{m}$ since the boundary layer is expected to increase in size with $\dot{m}$ (Eqn 5.2). As an example, for an increase in F_{Edd} from 10^{-2} to 10^{-1}, R_{in} would decrease by a factor of 0.5 for magnetospheric truncation, whereas R_{in} would increase by a factor of 2 if the boundary layer were responsible for setting the radial extent of the disk. By observing the source at different points throughout the outburst, it may be possible to determine how the inner disk and the star interact.

8.2 Magnetic Field Strength Estimates

In Chapter 5, I investigated the use of reflection diagnostics to determine the magnetic field strength in NS LMXBs. By assuming that the location of the inner disk radius inferred from the Fe K line corresponds to the Alfvén radius (where the energy density of the accreting material is equal to the magnetic field energy density), I placed conservative estimates on the strength of the magnetic field in these systems. Figure 5.5 shows a comparison of magnetic field strengths of known accreting millisecond X-ray pulsars (AMXPs) to NS LMXBs observed with *NuSTAR* over a range of F_{Edd}. The NS LMXBs populate a higher value of Eddington fraction than the AMXPs.

Pulsations were not detected in the *NuSTAR* observations for these sources. It is uncertain if the geometry was such that the pulsations were not observable (e.g., shielding of the pole by the accretion column) or if the source was not magnetically accreting at the time. For Aquila X-1 (denoted as a star in Figure 5.5) in particular, the 2014 observation is within the same F_{Edd} range as the observation taken by *RXTE* when pulsations were detected (Casella et al. 2008; Mukherjee et al. 2015). It is clear that the magnetic strengths implied from Fe line profiles are valuable and consistent with those seen for AMXPs. Therefore, this work demonstrated that Fe lines can be

used to estimate magnetic field strength.

8.3 Detection of Multiple Emission Features

In Chapter 2 and Chapter 7, I reported on the detection of low energy emission features. For the NS transient 1RXS J180408.9-34205 in Chapter 2, we observed the source in a hard X-ray state with little thermal contribution from the accretion disk. We were able to detect N VII, O VII, and O VIII lines with the *XMM-Newton*/RGS and Fe K lines with *NuSTAR*. These low-energy reflection features are significant because they occur at different ionization levels within the disk than the highly ionized Fe K lines. As a consequence, the emission likely emerges from different radii. We attempted to model the multiple reflection features allowing for this physical scenario. The Fe line region was consistent with the innermost stable circular orbit ($R_{in} \leq 1.85\ R_{ISCO}$) while the prominent oxygen features allowed for a larger radius ($R_{in} \leq 4.5\ R_{ISCO}$). Prior to these observations, multiple reflection features at low energy arising from different ionization zones had not been observed concurrently with a broad Fe line component.

In Chapter 7, I analyzed early *NICER* observations of Serpens X-1. Reflection models had predicted a prominent Fe L emission feature at ~ 1 keV when extrapolated down to 0.2 keV from *NuSTAR* observations of Serpens X-1 (Miller et al., 2013). *NICER* was able to detect the Fe L blend in this system for the first time due to its combination of large collecting area near 1.5 keV, < 100 eV energy resolution, and new reflection models that account for thermal emission irradiating the disk. This feature had previously been seen around accreting supermassive black holes and attributed to reflection, but this was the first confirmation in a NS LMXB. The Fe L blend has other lower-Z atomic species emitting in this region, therefore it is crucial to use a full reflection spectrum when modeling these features.

8.4 Constraints on NS Radii

The reflection spectrum can be used to place limits on the radial extent of the NS. In Chapter 3, I led a pioneering effort into constraining the M−R plane for NSs using reflection modeling. Two NSs, 4U 1636−53 and GX 17+2, were found to harbor accretion disks that are close to $R_{\rm ISCO}$. Therefore, I was able to examine the implications of the results for the EOS of ultradense matter. The radius of the ISCO around a compact object in units of gravitational radii is dependent upon the dimensionless spin parameter, $a = cJ/GM^2$, of the compact object (Bardeen et al., 1972); a range in spin therefore enables a translation to gravitational radii and then into kilometers. Figure 3.4 showed the regions that can be traced out on the mass-radius plane from accretion disks that extend to $R_{\rm ISCO}$. Rather than assuming specific values for a, I determined the likely range of a given the measured spin frequencies for these sources.

In order to estimate a, I need to determine the total angular momentum, J, of the NS. The total angular momentum can be obtained from the spin frequency, ν_{spin}, assuming a reasonable range of mass and radius for an NS ($J = Iw$, where $w = 2\pi\nu_{spin}$ and I is the moment of inertia). Here I provide updated estimates on the total angular momentum using EoS insensitive approximations for I rather than assuming a solidly rotating sphere. Approximations for the moment of inertia were calculated in Lattimer & Prakash (2001) based upon solutions of Einstein's equations for different mass-energy density distributions; the result is a simple relation that is insensitive to the EoS. Using the approximation that best agrees with most proposed EoSs (T VII: a quadratic variation of the mass-energy density within the NS), I obtain: $J = 4(1 - 1.1\beta - 0.6\beta^2)^{-1} MR^2\pi\nu_{spin}/7$, where $\beta = GM/Rc^2$ is the compactness parameter. I use the current measured mass range for NSs in LMXBs of $M = 1.24-2.12\ M_\odot$ reported in (Özel et al., 2016a). The allowed radius range is then bound by causality and break-up of the NS ($a = 0.7$), where the rotation of the star

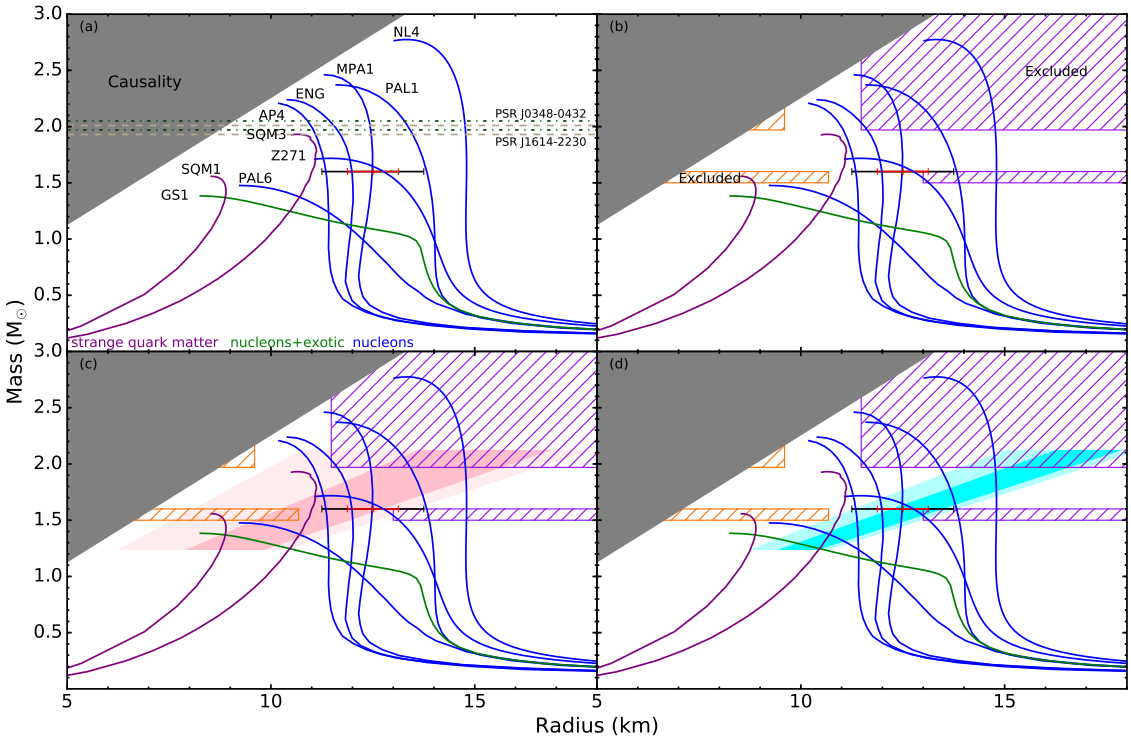

Figure 8.1 **Panel (a):** The mass−radius plane for NSs with different theoretical EoS with colors corresponding to internal composition from Figure 1.3. The black and red horizontal bar region indicates the 10% and 5% error on radius for a theoretical NS of $M = 1.6\ M_\odot$ and $R = 12.5$ km. **Panel (b):** Regions of exclusion based on the delayed collapse of the GW170817 (orange hatched region) from Bauswein et al. (2017). The violet hatched regions indicate exclusion based on a theoretical direct collapse NS-NS merger that may be detected in the future. **Panels (c) and (d):** Constraints on the cold, ultradense matter equation of state from reflection modeling to determine the inner disk radius adapted from Ludlam et al. (2017a) for two NS LMXBs: (c) 4U 1636-53 and (d) GX 17+2. The lighter area of the same color represents the uncertainty. As *NICER* delivers on its projected radius measurements to the 5% level, it will produce regions with widths on the order of the red horizontal line.

causes the star to no longer be gravitationally bound. For 4U 1636-53, $\nu_{spin} = 581$ Hz (Galloway et al., 2008) then implies $0.19 \pm 0.09 < a < 0.47 \pm 0.22$, and $\nu_{spin} = 293.2$ Hz (Wijnands et al., 1997) for GX 17+2 then implies $0.09 \pm 0.05 < a < 0.24 \pm 0.11$.

To reiterate, the ranges of spin given above enable a translation from $R_{\rm ISCO}$ to

gravitational radii, and hence provides an allowed region on the M−R plane. Figure 8.1 plots these ranges in the mass versus radius plane used to characterize the EOS and compares to gravitational wave constraints from the double NS merger. Disk reflection is able to provide comparable radius constraints to other methods though it is not yet able to rule out plausible EOSs; however, deeper X-ray spectra with multiple reflection components and complementary mass measurements in these systems can greatly reduce the allowed regions in this M−R plane.

8.5 The Future of Reflection Studies in NS LMXB

The combined observing power of *NICER* and *NuSTAR* can shed light on accretion disks in NS LMXBs and NS properties, including their radii. With these advanced X-ray observatories, we are now able to reveal the entire reflection spectrum in these systems, a result that was previously complicated by instrumental effects and lack of bandpass coverage. Through the simultaneous modeling of these reflection features from low-energy emission lines to the Compton hump at higher energies, improved statistical constraints can be obtained on the position of the inner disk. Figure 8.2 demonstrates the combined observing power of *NICER* and *NuSTAR*. There are nearly an order of magnitude more photons collected in the low-energy band (e.g., where Fe L or O VIII emits) than the Fe K band. These low-energy features can therefore improve the statistical power of disk reflection in providing constraints on the inner disk radius and, ultimately, upper limits on the NS radius.

Looking towards the future, 2030 will bring the launch of the European Space Agency's Advanced Telescope for High-energy Astrophysics (*Athena*) X-ray observatory (Nandra et al., 2013). *Athena* will have two interchangeable instruments onboard: the X-ray Integral Field Unit (X-IFU) and the Wide Field Imager (WFI). The X-IFU will have a collecting area of $\sim 10^4$ cm^2 at 1.5 keV with an energy resolution of 2.5 eV up to 7 keV (Barret et al., 2018). For comparison, the collecting area is 5

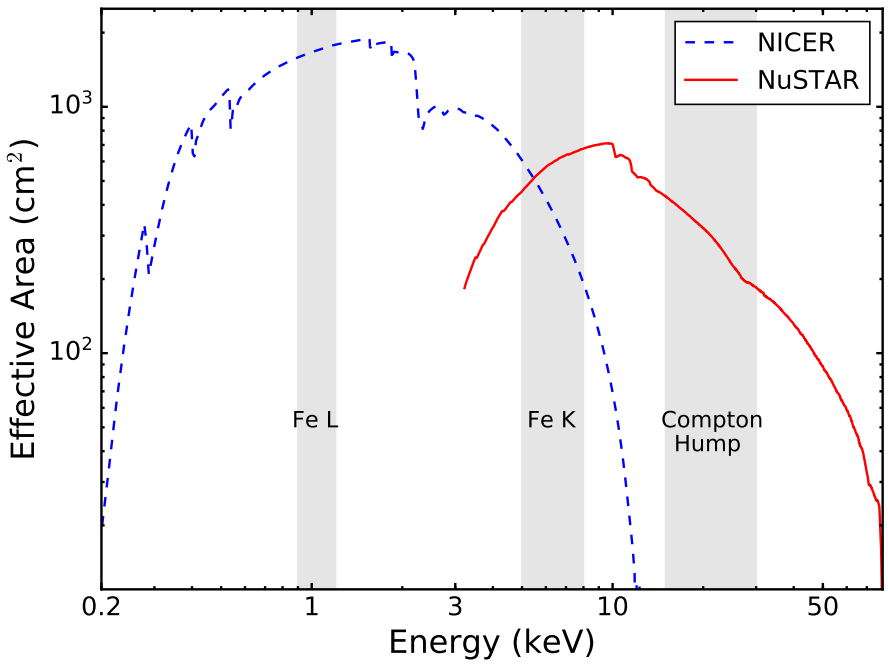

Figure 8.2 The collecting of *NICER* and *NuSTAR*. Combined observations from these telescopes allows for the entire reflection spectrum to be revealed from low energy emission features like Fe L ($0.9-1.2$ keV), to the broad Fe K line between $5-8$ keV, and the Compton hump near $15-30$ keV. These key regions are shaded in gray.

times larger and the energy resolution is 34 times better than *NICER*. In order to observe bright sources that are on the order of the Crab Nebula ($F_{2-10\ \mathrm{keV}} \simeq 2.4 \times 10^{-8}$ ergs cm^{-2} s^{-1}), a Be filter is used to block X-rays in the lower-E bandpass and the mirror is tilted to spread the PSF over more pixels. However, this still provides incredible energy resolution and throughput ($> 50\%$) in the Fe K band that can be used to reveal structure within this region and as a diagnostic of the disk density. The WFI aboard *Athena* will have comparable spectral resolution to *NICER* with an order of magnitude more collecting area (Meidinger et al. 2015; 2016). The WFI will likely be able to observe these bright sources without the use of the Be filter, which will reveal these lower-energy features and Fe K line concurrently with ≤ 170 eV resolution.

A natural complement to *Athena* is the High Energy X-ray Probe (*HEX-P*: Harri-

son et al. 2011). If selected as the next probe-class mission, *HEX-P* will have a large energy bandpass from $2 - 200$ keV with a 7 times improvement in collecting area and an energy resolution that is 2.7 times better at 6 keV (150 eV) than *NuSTAR*. This will be achieved with three focal plane modules and a 20 m deployable mast. If launched contemporaneously with *Athena*, the combined observing power of these facilities will allow for broad band spectral modeling from $0.2 - 200$ keV. Another proposed probe-class mission that *HEX-P* is competing with is the Spectroscopic Time-Resolving Observatory for Broadband Energy X-rays (*STROBE-X*: Ray et al. 2018). This mission is the intended successor of *NICER* with 80 X-ray concentrators (XRCs) that provide same energy coverage from $0.2 - 12$ keV, but larger collecting area ($\sim 2 \times 10^4$ cm^2) and better timing resolution of 100 ns ($\sim 100\times$ better than *Athena*). This factor of 10 improvement in collecting area over *NICER* will allow *STROBE-X* to measure the radius to 5% for ~ 20 NSs via light-curve modeling of pulse profiles. The large area detectors (LADs) are sensitive in the $2-30$ keV band to extend the coverage to the hard X-rays with 200-300 eV energy resolution. *STROBE-X* will also have a wide-field sky monitor (WFM) that is sensitive in the $2 - 50$ keV band to survey variability within the X-ray sky.

The larger collecting area and superior energy resolution of future missions will excel at enhancing our understanding of accretion in low-luminosity systems. We do not know the exact $\dot{m}$ at which the disk is no longer able to extend down to $R_{\rm ISCO}$ in LMXBs that host weak magnetic field NSs. Current attempts to observe sources at $F_{\rm Edd} < 10^{-2}$ require observations on the order of 100 ks. The large collecting area and energy resolution affords higher signal-to-noise observations in a shorter amount of time than previous X-ray observatories. Additionally, we can increase our understanding of ultra-compact X-ray binary (UCXBs) systems. UCXBs are a type of LMXB with a short orbital period of < 80 minutes and typically contain a degenerate stellar companion. The accretion disks in these systems differ from the typical LMXB

in the sense that they are almost devoid of hydrogen while overabundant in oxygen, carbon, and/or neon (Nelemans et al., 2004). In these systems the O VIII line (~ 0.65 keV) becomes dominant over Fe K. Targeting UCXBs and low $F_{\rm Edd}$ systems with these future missions can capture multiple reflection features with superior energy resolution and increase our understanding of the accretion geometry.

BIBLIOGRAPHY

Abbott, B. P., Abbott, R., Abbott, T. D., Acernese, F., Ackley, K., et al. 2017, Phys. Rev. L, 119, 161101

Akmal, A., Pandharipande, V. R., & Ravenhall, D. G. 1998, Phys. Rev. C, 58, 1804

Alcock, C., & Olinto, A. 1988, Ann. Rev. Nucl. Part. Sci., 38, 161

Antoniadis, J., Freire, P. C. C., Wex, N., Tauris, T. M., Lynch, R. S., et al. 2013, *Science*, 340, 448

Arnaud, K. A. 1996, in Astronomical Society of the Pacific Conference Series, Vol. 101, Astronomical Data Analysis Software and Systems V, ed. G. H. Jacoby & J. Barnes, 17

Arnaud, K., Smith, R., & Siemiginowska, A. 2011, Handbook of X-ray Astronomy, 1st edn., Cambridge Univ. Press, Cambridge

Arnaud, K., Gordon, C., & Dorman, B. 2018, XSPEC User's Guide for version 12.10.1, http://heasarc.gsfc.nasa.gov/docs/xanadu/xspec/manual/

Asai, K., Dotani, T., Nagase, F., & Mitsuda, K. 2000, ApJS, 131, 571

Asai, K., Matsuoka, M., Mihara, T., et al. 2013, ApJ, 773, 117

Baade, W, & Zwicky, F., 1934, Phys. Rev., 45, 138

Ballantyne, D. R. 2004, MNRAS, 351, 57

Balman, Ş. 2009, ApJ, 138, 50

Bałucińska-Church, M., Church, M. J., & Smale, A. P. 2004, MNRAS, 347, 334

Bardeen, J. M., Press, W. H., & Teukolsky, S. A. 1972, ApJ, 178, 347

Barret, D., & Olive, J.-F. 2002, ApJ, 576, 391

Barret, D., Olive, J.-F., & Miller, M. C. 2006, MNRAS, 370, 1140

Barret, D., Lam Trong, T., den Herder, J.-W., et al. 2018, Proc. of SPIE, 10699, 1

Bauswein, A., Just, O., Janka, H.-T., & Stergioulas, N. 2017, ApJ, 850, L34

Bhattacharyya, S., & Strohmayer, T. E. 2007, ApJ, 664, L103

Blandford, R. D., & Begelman, M. C. 1999, MNRAS, 303, L1

Bogdanov, S., Grindlay, J. E., & Rybicki, G. B. 2008, ApJ, 689, 407

Bowen, I. S. 1934, PASP, 46, 146

Braje, T. M., Romani, R. W., & Rauch, K. P. 2000, ApJ, 531, 447

Brandt S., Castro-Tirado A. J., Lund N., et al. 1992, A&A, 262, L15

Brenneman, L. W., & Reynolds, C. S. 2006, ApJ, 652, 1028

Brown, E. F., & Cumming, A. 2009, ApJ, 698, 1020

Cackett, E. M., Miller, J. M., Bhattacharyya, S., Grindlay, J. E., Homan, J., van der Klis, M., Miller, M. C., Strohmayer, T. E., & Wijnands, R. 2008, ApJ, 674, 415

Cackett, E. M., Altamirano, D., Patruno, A., et al. 2009, ApJ, 694, L21

Cackett, E. M., Miller, J. M., Ballantyne, D. R., et al. 2010, ApJ, 720, 205

Cackett, E. M., Miller, J. M., Reis, R. C., Fabian, A. C., & Barret, D. 2012, ApJ, 755, 27

Callanan, P. J., Curran, P., Filippenko, A. V., et al. 2002, ApJ, 574, L143

Campana, S., Stella, L., Mereghetti, S., et al. 1998, ApJ, 499, 65

Campana, S., Coti Zelati, F., & D'Avanzo, P. 2013, MNRAS, 432, 1695

Campana, S., Brivio, F., Degenaar, N., et al. 2014, MNRAS, 441, 1984

Caplan, M. E., & Horowitz, C. J. 2017, Rev. Mod. Phys. 89, 041002

Carroll B. W., & Ostlie D. A. 2007, An Introduction to Modern Astrophysics, 2nd edn., Pearson, San Francisco

Casares, J., Cornelisse, R., Steeghs, D., et al. 2006, MNRAS, 373, 1235

Casella, P., Altamirano, D., Patruno, A., Wijnands, R., & van der Klis, M. 2008, ApJ, 674, 41

Cash, W. 1979, ApJ, 228, 939

Chandrasekhar, S. 1931, ApJ, 74, 81

Chenevez, J., Falanga, M., Brandt, S., et al. 2006, A&A, 449, L5

Chenevez, J., Galloway, D. K., in't Zand, J. J. M., et al. 2016, ApJ, 818, 135

Chiang, C.-Y., Cackett, E. M., Miller, J. M., et al. 2016, ApJ, 821, 105

Chiang, C.-Y., Morgan, R. A., Cackett, E. M., et al. 2016, ApJ, 831, 45

Choudhury, K., García, J. A., Steiner, J. F., & Bambi, C. 2017, ApJ, 851, 57

Church, M. J., & Bałucińska-Church, M. 2001, A&A, 369, 915

Church, M. J., Gibiec, A., & Bałucińska-Church, M. 2014, MNRAS, 438, 2784

Cocchi, M., Bazzano, A., Natalucci, L., et al. 1998, ApJ, 508, L163

Cook, G. B., Shapiro, S. L., & Teukolsky, S. A. 1994, ApJ, 424, 823

Cornelisse, R., Casares, J., Charles, P. A., & Steeghs, D. 2013, MNRAS, 432, 1361

Coughenour, B. M., Cackett, E. M., Miller, J. M., & Ludlam, R. M. 2018, ApJ, 867, 64

D'Aì, A., Di Salvo, T., Ballantyne, D., et al. 2010, A&A, 516 A36

D'Aì, A., Iaria, R., Di Salvo, T., et al. 2014, A&A, 564, A62

Dauser, T., Wilms, J., Reynolds, C. S., & Brenneman, L. W. 2010, MNRAS, 409, 1534

Degenaar, N., Wijnands, R., & Miller, J. M. 2013, ApJ, 767, L31

Degenaar, N., Miller, J. M., Harrison, F. A., et al. 2014, ApJ, 796, L9

Degenaar, N., Altamirano, D., Deller, A., et al. 2015a, The Astronomer's Telegram, 7352, 1

Degenaar, N., Miller, J. M., Chakrabarty, D., et al. 2015, MNRAS, 451, L85

Degenaar, N., Altamirano, D., Parker, M., et al. 2016, MNRAS, 461, 4049

Degenaar, N., Pinto, C., Miller, J. M., et al. 2017, MNRAS, 464, 398

Degenaar, N., Ballantyne, D. R., Belloni, T., et al. 2018, SSRv, 214, 15

Deller, A., Degenaar, N., Hessels, J., et al. 2015, The Astronomer's Telegram, 7255, 1

Demorest, P. B., Pennucci, T., Ransom, S. M., Roberts, M. S. E., & Hessels, J. W. T. 2010, Nature, 467, 1081

Deutsch, E. W., Anderson, S. F., Margon, B., & Downes, R. 1998, ApJ, 493, 775

Deutsch, E. W., Margon, B., Anderson, S. F., Wachter, S., & Goss, W. M. 1999, ApJ, 524, 406

Di Salvo, T., Stella, L., Robba, N. R., et al. 2000, ApJ, 544, L119

Di Salvo, T., D'Aí, A., Iaria, R., et al. 2009, MNRAS, 398, 2022

Di Salvo, T., Iaria, R., Matranga, M., et al. 2015, MNRAS, 449, 2794

Di Salvo, T., Sanna, A., Burderi, L., et al. 2019, MNRAS, 483, 767

Díaz Trigo, M., Parmar, A. N., Boirin, L., Mendez, M., & Kaastra, J. 2006, A&A, 445, 179

Díaz Trigo, M., Sidoli, L., Boirin, L., M., & Parmar, A. N. 2012, A&A, 543, A50

Dickey, J. M., & Lockman, F. J. 1990, ARA&A, 28, 215

Done, C., Gierliński, M., & Kubota, A. 2007, A&A Rev., 15, 1

Eddington, A. S. 1916, MNRAS, 77, 16

Egron, E., Di Salvo, T., Motta, S., et al. 2013, A&A, 550, A5

Fabian, A. C., Rees, M. J., Stella, L., & White, N. E. 1989, MNRAS, 238, 729

Fabian, A. C., Iwasawa, K., Reynolds, C. S., & Young, A. J. 2000, PASP, 112, 1145

Fabian, A. C., Zoghbi, A., Ross, R. R., et al. 2009, Nat, 459, 540

Ford, E. C., van der Klis, M., Méndez, M., et al. 2000, ApJ, 537, 368

Fowler, W. A., & Hoyle, F. 1964, ApJS, 9, 201

Frank, J., King, A. R., & Lasota, J.-P. 1987, A&A, 178, 137

Freire, P. C. C., Bassa, C. G., Wex, N., et al. 2011, MNRAS, 412, 2763

Füerst, F., Grinberg, V., Tomsick, J. A., et al. 2016, ApJ, 828, 34

Galloway, D. K., Muno, M. P., Hartman, J. M., Psaltis, D., & Chakrabarty, D. 2008, ApJS, 179, 360

Galloway, D. K., Ajamyan, A. N., Upjohn, J., & Stuart, M. 2016, MNRAS, 461, 3847

Garcia, M. R., Callanan, P. J., McCarthy, J., Eriksen, K., & Hjellming, R. M. 1999, ApJ, 518, 422

García, J., & Kallman, T. R. 2010, ApJ, 718, 695

García, J., Dauser, T., Reynolds, C. S., et al. 2013, ApJ, 768, 146

García, J. A., Dauser, T., Lohfink, A., et al. 2014, ApJ, 782, 76

García, J. A., Steiner, J. F., McClintock, J. E., et al. 2015, ApJ, 813, 84

García, J. A., Fabian, A. C., Kallman, T. R., et al. 2016, MNRAS, 462, 751

García, J. A., Kallman, T. R., Bautista, M., et al. 2018, arxiv:1805.00581

Gatuzz, E., Kallman, T., García, J., Gorczyca, T., & Mendoza, C. 2014, in The X-ray Universe 2014, 253

Gendreau, K. C., Arzoumanian, Z., & Okajima, T. 2012, in Society of Photo-Optical Instrumentation Engineers (SPIE) Conference Series, Vol. 8443, 13

Gierliński, M., & Done, C. 2002, MNRAS, 337, 1373

Gilfanov, M., Revnivtsev, M., & Molkov, S. 2003, A&A, 410, 217

Gladstone, J., Done, C., & Gierliński, M. 2007, MNRAS, 378, 13

Glendenning, N. K. 1992, Phys. Rev. D, 46, 1274

González Martínez-País, I., Shahbaz, T., & Casares Velázquez, J. 2014, Accretion Processes in Astrophysics

Gupta, S., Brown, E. F., Schatz, H., Möller, P., & Kratz, K.-L. 2007, ApJ, 662, 1188

Haensel, P., & Zdunik, J. L. 1990, A&A, 227, 431

Haensel, P., Zdunik, J. L., Douchin, F. 2002, A&A, 385, 301

Haensel, P., & Zdunik, J. L. 2003, A&A, 404, L33

Haensel, P., & Zdunik, J. L. 2008, A&A, 480, 459

Harrison, F., Stern, D., Alexander, D., et al. 2011, https://pcos.gsfc.nasa.gov/studies/rfi/Harrison-Fiona-RFI.pdf

Harrison, F. A., Craig, W. W., Christensen, F. E., et al. 2013, ApJ, 770, 103

Hasinger, G., & van der Klis, M. 1989, A&A, 225, 79

Hermsen, W., & Wrinkler, C. 1998, IAUS, 188, 87

Hewish, A., Bell, S. J., Pilkington, J. D. H., Scott, P. F., Collins, R. A. 1968, Nature, 217, 709

Homan, J., van der Klis, M., Fridriksson, J. K., et al. 2010, ApJ, 719, 201

Homan, J. Steiner, J. F., Lin, D., et al. 2018, ApJ, 853, 157

Horowitz, C. J., Berry, D. K., Briggs, C. M., et al. 2015, Phys. Rev. Letters, 114, 031102

Horowitz, C. J., & Piekarewicz, J. 2001, Physical Review Letters, 86, 5647

Iaria, R., D'aì, A., Di Salvo, T., et al. 2009, A&A, 505, 1143

Iaria, R., Di Salvo, T., Burderi, L., et al. 2014, A&A, 561, 99

Iaria, R., Di Salvo, T., Del Santo, M., et al. 2016, A&A, 596, 21

Ibragimov, A., & Poutanen, J. 2009, MNRAS, 400, 492

Jacoby, B. A., Hotan, A., Bailes, M., Ord, S., & Kulkarni, S. R. 2005, ApJ, 629, L113

Jahoda, K., Markwardt, C. B., Radeva, Y., et al. 2006, ApJS, 163, 401

Jonker, P. G., Mendez, M., Nelemans, G., Wijnands, R., & van der Klis, M. 2003, MNRAS, 341, 823

Jonker, P. G., Buxton, M., & McClintock, J. E. 2004a, The Astronomer's Telegram, 262

Jonker, P. G., Galloway, D. K., McClintock, J. E., et al. 2004b, MNRAS, 354, 666

Kaur, R., & Heinke, C. 2012, The Astronomer's Telegram, 4085, 1

Kinch, B. E., Schnittman, J. D., Kallman, T. R., & Krolik, J. H. 2016, ApJ, 826, 52

King, A. L., Tomsick, J. A., Miller, J. M., et al. 2016, ApJ, 819, L29

Kitchin, C. R. 2009, Astrophysical Techniques, 5th edn., CRC Press, Boca Raton

Kiziltan, B., Kottas, A., De Yoreo, M., & Thorsett, S. E. 2013, ApJ, 778, 66

Krimm, H. A., Barthelmy, S. D., Baumgartner, W., et al. 2015a, The Astronomer's Telegram, 6997, 1

Krimm, H. A., Kennea, J. A., Siegel, M. H., & Sbarufatti, B. 2015b, The Astronomer's Telegram, 7039, 1

Kubota, A., Tanaka, Y., Makishima, K., et al. 1998, PASJ, 50, 667

Kuulkers, E., Parmar, A. N., Owens, A., Oosterbroek, T., & Lammers, U. 1997, A&A, 323, L29

Kuulkers, E., & van der Klis, M. 2000, A&A, 356, L45

Kuulkers, E. 2002, A&A, 383, L5

Kuulkers, E., den Hartog, P. R., in't Zand, J. J. M., et al. 2003, A&A, 399, 663

Kuulkers, E., in't zand, J. J. M., Atteia, J.-L., et al. 2010, A&A, 514, A65

Lagaris, I. E., & Pandharipande, V. R. 1981, Nuclear Physics A, 359, 349

Lamb, F. K., Shibazaki, N., Alpar, M. A., & Shaham, J. 1985, Nature, 317, 681

Lamb, F. K., Boutloukos, S., Van Wassenhove, S., et al. 2009, ApJ, 706, 417

Landau, L. D., 1932, Phys. Z. Sowjetunion, 1, 285

Langmeier, A., Sztajno, M., Hasinger, G., Truemper, J., & Gottwald, M. 1987, ApJ, 323, 288

Lattimer, J. M. 2011, Ap&SS, 336, 67

Lattimer, J. M., & Prakash, M. 2001, ApJ, 550, 426

Lattimer, J. M., & Prakash, M. 2004, ApJ,

Lattimer, J. M., & Prakash, M. 2016, Phys. Rep., 621, 127

Lee, J.-W., & Carney, B. W. 2006, AJ, 132, 2171

Lin, D., Remillard, R. A., & Homan, J. 2007, ApJ, 667, 1073

Lin, D., Remillard, R. A., & Homan, J. 2010, ApJ, 719, 1350

Ling, S.J., Sanny, J., Moebs, W., et al. 2016, University Physics Volume 3, OpenStax, Rice University, Texas. https://openstax.org/details/books/universityphysics-volume-3

London, R. A., Taam, R. E., Howard, W. M. 1986, ApJ, 306, 170L

Long, M., Romanova, M. M., & Lovelace, R. V. E. 2005, ApJ, 634, 1214

Ludlam, R. M., Miller, J. M., Cackett, E. M., et al. 2016, ApJ, 824, 37

Ludlam, R. M., Miller, J. M., Bachetti, M., et al. 2017a, ApJ, 836, 140

Ludlam, R. M., Miller, J. M., Cackett, E. M., Degenaar, N., & Bostrom, A. C. 2017b, ApJ, 838, 79

Ludlam, R. M., Miller, J. M., Cackett, E. M., et al. 2017c, ApJ, 847, 135

Ludlam, R. M., Miller, J. M., Arzoumanian, Z., et al. 2018, ApJL, 858, L5

Ludlam, R. M., Miller, J. M., Barret, D., et al. 2019, ApJ, 873, 99

Lyu, M., Méndez, M., Sanna, A., et al. 2014, MNRAS, 440, 1165

Madej, O. K., Jonker, P. G., Fabian, A. C., et al. 2010, MNRAS, 407, L11

Madej, O. K., García, J., Jonker, P. G., et al. 2014, MNRAS, 442, 1157

Makishima K., Mitsuda K., Inoue, H., et al. 1983, ApJ, 267, 310

Matranga, M., Di Salvo, T., Iaria, R., et al. 2017, A&A, 600, 24

Markwardt, C. B., Strohmayer, T. E., & Swank, J. H. 1999, ApJ, 512, L125

Markwardt, C. B., & Swank, J. H. 2004, The Astronomer's Telegram, 255

Marshall, F. E., Swank, J. H., Thomas, B., et al. 1997, IAU Circ., 6543

Mata Sánchez, D., Muñoz-Darias, T., Casares, J., & Jiménez-Ibarra, F. 2017, MNRAS, 464, 41

Mazzola, S. M., Iaria, R., Di Salvo, T., et al. 2018, Arxiv: 1811.10922

Meidinger, N., Nandra, K., Plattner, M., et al. 2015, JATIS, 1, 014006

Meidinger, N., Eder, J., Eraerds, T., et al. 2016, Proc. of SPIE, 9905, 78

Merloni, A., Fabian, A. C., Ross, R. R. 2000, MNRAS, 313, 193

Miller, J. M., Fabian, A. C., Reynolds, C. S., et al. 2002, AAS, 201, 5701

Miller, J. M. 2007, ARA&A, 45, 441

Miller, J. M., Cackett, E. M., & Reis, R. C. 2009, ApJ, 707, L77

Miller, J. M., D'Ai, A., Bautz, M. W., et al. 2010, ApJ, 724, 1441

Miller, J. M., Maitra, D., Cackett, E. M., Bhattacharyya, S., & Strohmayer, T. E. 2011, ApJ, 731, L7

Miller, J. M., Parker, M. L., Füerst, F., et al. 2013, ApJ, 779, L2

Miller, M. C., Lamb, F. K., & Psaltis, D. 1998, ApJ, 508, 791

Misner, C. W., Thorne, K. S., & Wheeler, J. A. 1973, Gravitation, Freeman, San Francisco

Mitsuda, K., Inoue, H., Koyama, K., et al. 1984, PASJ, 36, 741

Mondal, A. S., Dewangan, G. C., Pahari, M, & Raychaudhuri, B. 2018, MNRAS, 474, 2064

Mukherjee, D., Bult, P., van der Klis, M., & Bhattacharya, D. 2015, MNRAS, 452, 3994

Nakahira, S., Mihara, T., Matsouka, M., et al. 2016, The Astronomer's Telegram, 9108, 1

Nandra, K., Barret, D., Barcons, X., et al. 2013, arXiv:1306.2307

Narayan, R., & Yi, I. 1994, ApJ, 428, L13

Narayan R., & Yi I., 1995, ApJ, 452, 710

Negoro, H. Sugizaki, M., Tomida, H., et al. 2010, The Astronomer's Telegram, 2729, 1

Negoro, H., Kawai, N., Nakagawa, Y., et al. 2013, The Astronomer's Telegram, 5319, 1

Negoro, H., Sugimoto, J., Mihara, T., et al. 2015, The Astronomer's Telegram, 7008, 1

Nelemans, G., Jonker, P. G., Marsh, T. R., & van der Klis, M. 2004, MNRAS, 348, L7

Ng, C., Díaz Trigo, M., Cadolle Bel, M., & Migliari, S. 2010, A&A, 522, A96

Oosterbroek, T., Barret, D., Guainazzi, M., & Ford, E. C. 2001, A&A, 366, 138

Oppenheimer, J. R., & Volkoff, G. M. 1939, Physical Review, 55, 374

Özel, F., Baym, G., & Güver, T. 2010, Physical Review D, 82, 101301

Özel, F., Psaltis, D., Güver, T., et al. 2016a, ApJ, 820, 28

Özel, F., Psaltis, D., Arzoumanian, Z., Morsink, S., & Baubck, M. 2016b, ApJ, 832, 92

Pandel, D., Kaaret, P., & Corbel, S. 2008, ApJ, 688, 1288

Papitto, A., D'Ai, A., Di Salvo, T., et al. 2008, The Astronomer's Telegram, 1846, 1

Papitto, A., Di Salvo, T., D'Aí, A., et al. 2009, A&A, 493, L39

Papitto, A., D'Ai, A., Di Salvo, T., et al. 2013, MNRAS, 429, 3411

Park, S. Q., Miller, J. M., McClintock, J. E., et al. 2004, ApJ, 610, 378

Parker, M. L., Tomsick, J. A., Miller, J. M., et al. 2015, ApJ, 808, 9

Parker, M. L., Tomsick, J. A., Kennea, J. A., et al. 2016, ApJ, 821, 6

Parmar, A. N., Stella, L., & Giommi, P. 1989, A&A, 222, 96

Pedersen, H. et al. 1982, ApJ, 263, 325

Petrucci, P. O., Merloni, A., Fabian, A., Haardt, F., & Gallo, E. 2001, MNRAS, 328, 501

Pintore, F., Di Salvo, T., Bozzo, E., et al. 2015, MNRAS, 450, 2016

Pintore, F. et al. 2016, MNRAS, 457, 2988

Piraino, S., Santangelo, A., Di Salvo, T., et al. 2007, A&A, 471, L17

Piraino, S., Santangelo, A., Kaaret, P., et al. 2012, A&A, 542, L27

Ponti, G., Gallo, L. C., Fabian, A. C., et al. 2010, MNRAS, 406, 2591

Popham, R., & Sunyaev, R. 2001, ApJ, 547, 355

Prialnik, D. 2009, An Introduction to the Theory of Stellar Structure and Evolution, 2nd edn., Cambridge Univ. Press, Cambridge

Prigozhin, G., Gendreau, K., Foster, R., et al. 2012, Proc. SPIE, 8453, 845318

Pritzl, B. J., Smith, H. A., Catelan, M., & Sweigart, A. V. 2001, ApJ, 122, 2600

Ray, P. S., Arzoumanian, Z., Brandt, S., et al. 2018, Proc. of SPIE, 10699, 19

Reis, R. C., Fabian, A. C., Ross, R. R., et al. 2008, MNRAS, 387, 1489

Reis, R. C., Fabian, A. C., Ross, R. R., & Miller, J. M. 2009a, MNRAS, 395, 1257

Reis, R. C., Fabian, A. C., & Young, A. J. 2009b, MNRAS, 399, L1

Remillard, R. 2007, The Astronomer's Telegram, 1302, 1

Reynolds, C. S., & Fabian, A. C. 2008, ApJ, 675, 1048

Rhoades, C. E., & Ruffini, R. 1972, Phys. Rev. Letters, 32, 324

Ross, R. R., & Fabian, A. C. 1993, MNRAS, 261, 74

Ross, R. R., & Fabian, A. C. 2005, MNRAS, 358, 211

Rothschild, R. E., Blanco, P. R., Gruber, D. E., et al. 1998, ApJ, 496, 538

Sanchez-Fernandez, C., Chenevez, J., Pavan, L., et al. 2012, The Astronomer's Telegram, 4304, 1

Sanna, A., Hiemstra, B., Méndez, M., Altamirano, D., Belloni, T., & Linares, M. 2013, MNRAS, 432, 1144

Sanna, A., Méndez, M., Altamirano, D., Belloni, T., Hiemstra, B., & Linares, M. 2014, MNRAS, 440, 3275

Sanna, A., Riggio, A., Pintore, F. et al. 2016a, The Astronomer's Telegram, 9287, 1

Sanna, A., Riggio, A., Pintore, F. et al. 2016b, The Astronomer's Telegram, 9292, 1

Sansom, A. E., Dotani, T., Asai, K., & Lehto, H. J. 1993, MNRAS, 262, 429

Schulz, N. S. 1999, ApJ, 511, 304

Shahbaz, T., Watson, C. A., Zurita, C., Villaver, E., & Hernandez-Peralta, H. 2008, PASP, 120, 848

Shapiro, I. I. 1964, Phys. Rev. Letters, 13, 789

Shapiro, S., & Teukolsky, S. 1983, Black Holes, White Dwarfs and Neutron Stars, John Wiley & Sons, USA

Shih, I. C., Bird, A. J., Charles, P. A., Cornelisse, R., & Tiramani, D. 2005, MNRAS, 361, 602

Shimura, T., Takahara, F. 1995, ApJ, 445, 780

Sibgatullin, N. R., & Sunyaev, R. A. 1998, Astronomy Letters, 24, 774

Sibgatullin, N. R. & Sunyaev, R. A. 2000, Astronomy Letters, 26, 699

Sidoli, L., Oosterbroek, T., Parmar, A. N., Lumb, D., & Erd, C. 2001, A&A, 379, 540

Sleator, C. C., Tomsick, J. A., King, A. L., et al. 2016, ApJ, 827, 143

Sobczak, G. J., McClintock, J. E., Remillard, R. A., et al. 2000, ApJ, 544, 993

Strohmayer, T. E., & Markwardt, C. B. 2002, ApJ, 577, 337

Strohmayer, T. E., Markwardt, C. B., & Kuulkers, E. 2008, ApJ, 672, L37

Sunyaev, R. A., Arefev, V. A., Borozdin, K. N., et al. 1991, Soviet Astronomy Letters, 17, 409

Swank, J. H., Becker, R. H., Pravdo, S. H., Saba, J. R., & Serlemitsos, P. J. 1976, IAU Circ., 3010, 1

Swank, J. H., Boldt, E. A., Holt. S. S., Serlemitsos, P. J., & Becker, R. H. 1978, MNRAS, 182, 349

Sztajno, M., Fujimoto, M. Y., van Paradijs, J., et al. 1987 MNRAS, 226, 39

Takahashi, T, Abe, K., Endo, M., et al. 2007, PASJ, 59, 35

Tarenghi, M., & Reina, C. 1972, Nature Physical Science, 240, 53

Thorstensen, J., Charles, P., & Bowyer, S. 1978, ApJL, 220, L131

Tolman, R. C. 1934, Relativity, Thermodynamics, and Cosmology, Oxford: Clarendon Press

Tolman, R. C. 1939, Physical Reviews, 55, 364

Tomsick J., Yamaoka K., Corbel S., et al. 2009, ApJL, 707, L87

Tomsick, J. A., Parker, M. L., García, J. A., et al. 2018, ApJ, 855, 3

van den Eijnden, J., Bagnoli, T., Degenaar, N., et al. 2017, MNRAS, 466, 98

van den Eijnden, J., Degenaar, N., Pinto, C., et al. 2018, MNRAS, 475, 2027

van der Klis, M. 2006, Compact Stellar X-Ray Sources, Cambridge Univ. Press, Cambridge

van Paradijs, J. 1979, ApJ, 234, 609

van Paradijs, J., van der Klis, M., van Amerongen, S., et al. 1990, A&A, 234, 181

Veledina A., Poutanen J., & Vurm I. 2013, MNRAS, 430, 3196

Verner, D. A., Ferland, G. J., Korista, K. T., & Yakovlev, D. G. 1996, ApJ, 465, 487

Vrtilek, S. D., Swank, J. H., & Kallman, T. R. 1988, ApJ, 326, 186

Walton, D. J., Reis, R. C., Cackett, E. M., Fabian, A. C., & Miller, J. M. 2012, MNRAS, 422, 2510

Walton, D. J., Risaliti, G., Harrison, F. A., et al. 2014, ApJ, 788, 76

Walton, D. J., Tomsick, J. A., Madsen, K. K., et al. 2016, ApJ, 826, 87

Waterhouse, A. C., Degenaar, N., Wijnands, R., et al. 2016, MNRAS, 456, 4001

Watts, A. L., Andersson, N., Chakrabarty, D., et al. 2016, Rev. Mod. Phys., 88, 021001

Weisskopf, M.C., Guainazzi, M., Jahoda, K., et al. 2010, ApJ, 713, 912

White, N. E., & Zhang, W. 1997, ApJ, 490, L87

Wijnands, R. et al. 1997, ApJ, 490, L157

Wijnands, R., Parikh, A. S., Altamirano, D., Homan, D., & Degenaar, N. 2017, MNRAS, 472, 559

Wilkins, D. R., Fabian, A. C., 2012, MNRAS, 424, 1284

Wilkins, D. R. 2018, MNRAS, 475, 748

Wilms, J., Allen, A., & McCray, R. 2000, ApJ, 542, 914

Witten, E. 1984, Phys Rev D, 30, 272

Zdziarski, A. A., Johnson, W. N., & Magdziarz, P. 1996, MNRAS, 283, 193

Zhang, W., Lapidus, I., Swank, J. H., White, N. E., & Titarchuk, L. 1997, IAU Circ., 6541

Zhang, W., Jahoda, K., Kelley, R. L., et al. 1998, ApJL, 495, L9

Zycki, P. T., Done, C., & Smith, D. A. 1999, MNRAS 309, 561